Autonomous Stabilization and Quantum Squeezing of a Spin Ensemble Coupled to a Driven Optical Cavity

by

Olive Eilbott

A dissertation submitted in partial satisfaction of the

requirements for the degree of

Doctor of Philosophy

in

Physics

in the

Graduate Division

of the

University of California, Berkeley

Committee in charge:

Professor Dan M. Stamper-Kurn, Chair
Professor Ehud Altman
Assistant Professor Alp Sipahigil

Summer 2025

Autonomous Stabilization and Quantum Squeezing
of a Spin Ensemble Coupled to a Driven Optical Cavity

Copyright 2025
by
Olive Eilbott

Abstract

Autonomous Stabilization and Quantum Squeezing
of a Spin Ensemble Coupled to a Driven Optical Cavity

by

Olive Eilbott

Doctor of Philosophy in Physics

University of California, Berkeley

Professor Dan M. Stamper-Kurn, Chair

The development of quantum mechanics introduced ideas of measurement and information connected to the quantum nature of systems under study. Measurement is intrinsically linked to back-action that disturbs the measured system. Information extracted from a classical or quantum system can be used to steer the state of the system by conditioning the action of an appropriate actuator on the extracted information. Classical feedback to a quantum system involves conditioning the system Hamiltonian on measurement results, and in recent years has been used to produce entangled states that have been shown to exhibit squeezing. In the absence of conditional input to a system, dissipation can cause interacting subsystems and single systems with time-delayed self-interactions to exhibit coherent quantum feedback, wherein the interactions stabilize the system state.

In this work I explore the optodynamical light-matter interaction between a cloud of atoms and a dispersively coupled optical cavity and study the exchange of angular momentum between the light field and the collective atomic spin formed by symmetrically coupled ^{87}Rb atoms in their $F = 2$ hyperfine ground-state manifold. Weaving together the two concepts of conditional squeezing by weak measurement and of autonomous optodynamical stabilization, I build a theory of a novel type of autonomous squeezing in which dissipative coherent quantum feedback powered by light pumping the cavity produces an unconditionally squeezed spin state. Additionally, I show that the state is simultaneously conditionally squeezed. Equipped with a portion of the information carried by photons leaving the cavity, a conditional rotation on the state produces a deterministically squeezed state of the collective spin out to infinite time, in the absence of scattering and other decoherence. In the presence of scattering I show that the system exhibits squeezing at intermediate times.

In a detour from spin optodynamics, I report a series of experiments exploring molecular photoassociation in an optical cavity that demonstrate real-time monitoring of the photoassociation dynamics, and I discuss the prospects and motivation for observing cavity-mediated photoassociation.

To my sister Kayla, my mom Rikelle, my dad Seth

Contents

Contents **ii**

List of Figures **v**

List of Tables **vii**

1 Introduction **1**
1.1 Ultracold atomic clouds and dispersive coupling 2
1.2 Dispersive cavity quantum electrodynamics 4
1.3 Cavity optomechanics and spin optodynamics 5
1.3.1 Introduction to atom–cavity interactions 6
1.4 My journey through the PhD 7
1.4.1 My time with E3 10
1.5 Definitions, notation, and conventions 11

2 Experimental hardware **13**
2.1 Preparation of the atomic sample 14
2.1.1 Initial cooling and trapping 16
2.1.2 Magnetic trapping and transport 16
2.1.3 Optical dipole trapping 16
2.2 The science cavity 17
2.2.1 Longitudinal mode spectrum and co-resonance 19
2.2.2 Atom–cavity elliptical birefringence 21
2.2.3 Science cavity piezo–chip temperature feedback 25
2.3 Laser stabilization 26
2.3.1 Locking to spectroscopy 26
2.3.2 Reference cavity 26
2.3.3 Lasers used in this experiment 27
2.3.4 Wavemeter lock 27
2.4 Optical readout 28
2.4.1 Heterodyne detection 28
2.4.2 Single-photon detection 29

2.4.3 Optical imaging . . . 29
2.5 Homodyne and heterodyne measurement rates . . . 30
2.5.1 Motivation: atom counting and path length noise . . . 30
2.5.2 Dispersive measurement rates . . . 31
2.5.3 Adaptive optics: two-color path-phase-stabilization lock . . . 34
2.6 The slow, then fast, end of E3 . . . 41
2.6.1 The slow end of E3 . . . 41
2.6.2 The fast end of E3 . . . 42

3 Cavity–spin autonomous stabilization 45
3.1 Introduction . . . 45
3.2 Cavity–spin optodynamical Hamiltonian . . . 46
3.2.1 Dispersive interactions between a spin ensemble and a single-mode optical cavity . . . 47
3.2.2 Full cavity–spin optodynamical Hamiltonian . . . 50
3.2.3 Conceptual picture of the system . . . 50
3.2.4 Semiclassical equations of motion . . . 53
3.2.5 Atomic scattering and excited-state adiabatic elimination . . . 55
3.2.6 Optical detection of collective atomic spin states . . . 56
3.3 Observation of autonomous cavity–spin feedback . . . 59
3.3.1 Experimental results . . . 59
3.4 Conclusion . . . 61

4 Cavity–optodynamical autonomous spin squeezing 62
4.1 Introduction . . . 62
4.1.1 Analysis roadmap . . . 63
4.2 Steady-state spin distribution . . . 64
4.2.1 Rate equations and detailed balance . . . 64
4.2.2 Numerical steady-state solution of the Lindblad equation . . . 67
4.3 Cavity–spin Heisenberg–Langevin equations . . . 68
4.3.1 Solution for the cavity field . . . 69
4.3.2 Deriving the reduced spin equations of motion . . . 73
4.3.3 Damping and the atomic scattering rate . . . 74
4.4 Dynamics of the reduced spin equations . . . 75
4.4.1 Variance of the spin transverse to the field axis . . . 76
4.4.2 Variance of the spin component along the field axis . . . 77
4.5 Measurement of non-commuting observables . . . 80
4.6 Autonomous spin squeezing . . . 81
4.6.1 Unconditional squeezing . . . 82
4.6.2 Conditional squeezing . . . 85
4.6.3 Scattering limit . . . 86

5 Cavity photoassociation spectroscopy of $^{87}Rb_2$ **92**
5.1 Introduction 92
5.2 Model and calculations of photoassociation rates 93
5.2.1 One-color photoassociation in free space 93
5.2.2 Two-color photoassociation in free space 96
5.2.3 Atom number during photoassociation 97
5.2.4 Photoassociation in a cavity nearly resonant with an atomic transition 98
5.2.5 Photoassociation in a cavity nearly resonant with a molecular transition 99
5.2.6 Cavity-assisted photoassociation 99
5.3 Selection of molecular manifolds and states 100
5.4 Molecular spectroscopy experiments 103
5.4.1 One-photon molecular spectroscopy experiments 103
5.4.2 Two-photon molecular spectroscopy experiments 104
5.5 Toward cavity and collective enhancement 106

Bibliography **110**

List of Figures

2.1 Photograph of the E3 vacuum chamber with optical and electrical equipment . . 14
2.2 Photograph of the optical cavities and absorption image of atoms in the cavity . 15
2.3 Photograph of the view inside the E3 vacuum chamber through the west viewport 18
2.4 Calculation of cavity transmission and mirror phase shifts 20
2.5 Co-resonance determination of cavity spacing 22
2.6 Systematic shifts in the spectrum of a birefringent cavity 24
2.7 Two-color heterodyne interferometer conceptual sketch 30
2.8 Cavity transmission function and homodyne and heterodyne measurement rates 32
2.9 Realized two-color heterodyne interferometer and signal chain 36
2.10 Spectrum of two-color heterodyne signal and signal isolation 38
2.11 Phase-stabilized heterodyne measurements across cavity resonance 39
2.12 Demonstration of two-color cavity interferometer heterodyne phase stabilization 40
2.13 Ion pump current over time indicating vacuum pressure rise 42
2.14 Excerpt of a text conversation 42
2.15 Photographic evidence of damage to atom chip wires 43
2.16 Varistor-based protection circuit with and without a fuse 44

3.1 Energy level diagram of ^{87}Rb D_2 transition 48
3.2 Relative ^{87}Rb $f = 2$ scalar, vector, and tensor dispersive coupling strengths . . . 49
3.3 Schematic of cavity–spin optodynamics system in tilted field 51
3.4 Larmor precession sideband asymmetry in a dispersively shifted cavity 51
3.5 Optodynamics in a transverse field 53
3.6 Optodynamical evolutions of longitudinal spin in transverse and tilted fields . . 54
3.7 Semiclassical optodynamical spin damping in a tilted field 56
3.8 Tilted-field optodynamical spin damping rate versus various parameters 57
3.9 Measurement of the cavity–spin autonomous stabilization process 60

4.1 Steady-state variance of spin under optodynamical rate-equation evolution . . . 66
4.2 Steady-state variance of spin under Lindbladian evolution 68
4.3 Comparison between analytic transverse diffusion expression and numerical result 77
4.4 Predicted phase diagram of unconditional squeezing in the absence of scattering 84
4.5 Squeezing dynamics with and without scattering 87

5.1 One-color photoassociation schematic 93
5.2 Two-color photoassociation schematic 98
5.3 Partial molecular level structure of the $a^3\Sigma$ and 0_g^- potentials in $^{87}Rb_2$ 101
5.4 Calculated photoassociation rates, Franck–Condon factors, and figure-of-merit . 102
5.5 Single-color photoassociation spectroscopy of the 0_g^- $\nu' = 1$ vibrational level . . . 104
5.6 Two-laser beat-note lock and spectrum 105
5.7 Two-color photoassociation spectroscopy of 0_g^- $\nu' = 1$, $a^3\Sigma$ $\nu = 36$ 106
5.8 Two-color atom loss spectrogram of 0_g^- $\nu' = 1$, $a^3\Sigma$ $\nu = 36$ 107
5.9 Two-color ^{87}Rb photoassociation spectroscopy of 0_g^- $\nu' = 1$, $a^3\Sigma$ $\nu \in \{36, 37, 38, 39\}$ 108

List of Tables

4.1 Basic system parameters and fiducial values 89
4.2 Composite system parameters, definitions, and fiducial values 90
4.3 Assumptions, approximations, and small parameters 91

Acknowledgments

I made it to this point with the support of many people. My first formal research project was at the University of Texas at Dallas, working with Professors Lindsay King and Michael Kesden. Their advice, encouragement, mentorship, and endless mugs of tea helped me navigate the path towards graduate school. In this project I also worked alongside my friends Jonathan Cohn and Alex Riley who have completed graduate school as well.

My first formal experience with experimental science was at the University of California, Davis, where I worked with Professor Rena Zieve on vortex (un)pinning in superfluid ^{4}He as part of a summer REU program. I benefited from living in the Pierce co-op house with all the other REU students and find our ways through our research and our new lives in California together. I miss the house cat, Datura, and the fig tree in the back.

After that, in my last semester of college, I participated in the Green Fellows program in which I worked in a biophysics laboratory at UT Southwestern Medical Center learning about microtubule growth and collapse dynamics. Working in a wet lab was a very different experience and helped me develop my attention to detail, and my sense of time that my friends sometimes describe as uncanny.

I am happy to have remained in touch with a number of dear friends from college, many of whom have also gone to graduate school in science, including Jon, Rebecca, and Kiyn.

When I applied to Berkeley, I thought I would dive into condensed matter experiment or theory. But there were so many active fields here that I had never even heard about and many more that I was clueless about! Several professors welcomed me into their research groups here, which allowed me to find a good fit. I am grateful to Professors Naomi Ginsberg, Michael Crommie, and Alessandra Lanzara for welcoming me into their groups and their laboratories, and many kind folks in their groups for mentoring me. These included Dr. Milan Delor in the Ginsberg group, Dan Rizzo in the Crommie group, and graduate students Sam Ciocys, Conrad Stansbury, and Nick Dale in the Lanzara group. In my ARPES days, I learned a great deal from beamline scientist Jonathan Denlinger, who seemingly knew the answer to question after question that I asked him, and he made it a very straightforward experience to use beamline 4.0.3 (MERLIN) for my measurements. When I decided to change research groups, I appreciated advice from Professors Holger Müller and Heather Gray.

In my first semester of graduate school, I took a class called Advanced Atomic, Molecular and Optical Physics taught by Professor Norman Yao and studied with the other first-year students in the class, Julian Wolf and Eric Parsonnet, but I did not think that much about actually working in the research field for for some time after that. Eventually I made contact with Professor Dan M. Stamper-Kurn and asked if there might be a spot in his group for me. He saw connections between the skills I had been learning in my earlier graduate work and the projects in his group, and he welcomed me onto a new experiment he was starting. On that project I had the opportunity to work with and learn from a network of scientists including Professors Norman Yao, Hartmut Häffner, and Manuel Endres, postdocs Dr. Josh Isaacs, Dr. Emily Davis, and Dr. Xudong Lv, and graduate students Ivaylo Madjarov and Weijie Wu. After that project shut down, I transitioned to working on Dan's then-oldest

running experiment, code-named E3, with my close friend Julian and our fantastic postdoc Josh. It is our work on this experiment that I report in this dissertation.

I am deeply grateful to have had the opportunity to work with Dan for the past four and a half years. His intuition for the core physics of a problem and his recollection of the history of nearly every last bolt on our machines are incredible. On many occasions I have brought a new idea to him and described some confusing part, to which he would often respond by staring silently into the distance for up to several minutes — then suddenly he would refocus his attention on me and, with sometimes only a few words, share the key piece that I was missing. His lofty expectations and his insistence that we be bold have helped me push myself in my thinking and in my abilities and in my confidence. It is with his expert teachings, advice, mentorship, guidance, and wisdom that I have been able to grow into an independent scientist.

My time on E3 with Dan, Josh, Julian, and our visiting master's student Kevin Mours, was very challenging, but very enjoyable. It was full of light-hearted banter mixed into long stretches of troubleshooting, measurements, head-scratching, and breakthroughs. Josh taught me so much, including just about everything I know about molecules and how to couple light into a fiber. Julian introduced me to cavity–spin stabilization and taught me a ton about feedback generally. It is thanks in no small part to the mentorship of Dan, Josh, and Julian that I have made through graduate school. My interactions, mentorship by, and mentorship of all other members of the Ultracold group have also taught me a lot along the way. I am especially grateful to Rowan Duim, Scott Eustice, Jack Schrott, Jacqie Ho, Shao-Wen Chang, Malte Schwarz, and Dr. Zhenjie Yan.

On my committee for my qualifying exam before my advancement to candidacy were Dan and Professors Naomi Ginsberg, Ehud Altman, and Alp Sipahigil, who kindly offered their time to participate and advise me. I appreciate the efforts of Dan, Ehud, and Alp in reviewing this dissertation before its submission.

I have had helpful conversations with many colleagues and scientists including useful theory discussions with Dr. Francisco Machado and Dr. Mohan Sarovar.

I have been extremely fortunate to make so many friends here in Berkeley in my program, in our labor union UAW 4811, and about town. Early in graduate school I became close with friends in my cohort including Vikram, Shannon, Winston, Nathaniel, Tessa, Greg, Kayla, Anne, Hadar, Eric, and Roger, and my friends made along the way within the program include Tamar, Gabe, Mèabh, Violet, Livia, Bethany, Nikola, and many others.

Outside of physics I am incredibly grateful to my dear housemates (former, current, and future), loved ones, and family, including Kaj, Anna, Cassie, Irian, Cass, Vikram, Winston, Tessa, Julian, Will, Zoe, Robyn, Julia, Jamie, and Noe. With them I have found joy, fun, growth, and comfort that have carried me through the past years. I am also grateful to my kind, humble, and extremely knowledgeable darkroom photography instructor Xochitlquetzal, and the sweet folks Khendu and Gopal at Momo Masalas who have kept me fed during long days on campus. I am appreciative of the places I have lived, worked, and learned during this time, including our house in the hills, *Casa Lesbiana*; the table on the east end of the lowest floor of the East Asian Library; and the Berkeley Art Studio darkroom.

My parents and sister have always supported me in pursuing science and mathematics and in being silly all the time. My grandparents, as well, have always supported my seeking an education, and my uncles David and Eli have long listened to me talking about my research and interests. I credit my dad with initially sparking my interest in mathematics and for teaching me a great deal of math when I was very young. My mom has always advocated for me and always encouraged me to pursue my passions. My sister has stuck by me through everything and I cherish every minute I have with her. Most importantly, my family has always shown me unconditional love.

I completed this dissertation and the work reported therein during a time of great challenges both local and global. The ongoing COVID-19 pandemic posed a significant disruption during my degree. My work in E3 had to be put on pause while, with our labor union UAW 4811, we went on strike for six weeks in late 2022. And I want to acknowledge that not all people have equal, equitable, or even any, access to scientific education, facilities, and training; the same is true as for the fruits of the endeavors of the scientific community. At the time of writing this, there are no universities, schools, or hospitals left in Gaza. I believe we in the scientific community are not removed from personal responsibilities to speak out against injustice and to build a better world for those living today and for those who come after us. For me, this also means we must consider the impacts of our scientific work on the world and on humanity.

Outside of research I spend most of my time making photographs and trying to find my place in fighting for the liberation of queer and trans people and all those facing oppression.

I am grateful to have been supported in my graduate studies by the National Science Foundation Graduate Research Fellowship Program, which made it possible for me to experiment with so many different experiments early in my degree.

Chapter 1

Introduction

Observation, with its quantification in measurement, is the basis of physical science. A successful physical theory is one that accurately predicts the results of measurements and is thus supported by experimental observation. The theory of quantum mechanics developed and established one century ago has been subject to incredible tests and remains the foundation for the study of nearly all physical phenomena due to its extraordinary agreement with physical measurements [1, 2]. It is a theory of matter, of light, of the interaction between the two, of information, and of measurement (and observation) itself.

Light, long thought to be wave-like, was understood beginning in the 20th century to exhibit particle-like properties [3–5], including its role in transitions with discrete energies; as well as its momentum, found to be frequency dependent. Matter, previously thought to be particle-like, was likewise found near the same period to exhibit wave-like properties, originating from a collection of experiments that observed the diffraction of electrons, and later the diffraction of larger entities including atoms and molecules.

Knowledge of the state of a quantum system can be used statistically to predict the outcome of measurements on that system. This predictive power obeys an inviolable constraint described by the uncertainty principle. Unitarity of time evolution in quantum mechanics guarantees that information about quantum states is conserved, that it cannot be created, copied, or destroyed, only transported. Quantum information dynamics play a critical role in the behavior of quantum systems, and analysis of the allowed forms of information transfer predict the possible outcomes of interactions between systems.

With this work I discuss experiments conducted using a cloud of ultracold atoms located within and interacting with a high-finesse optical cavity. The experiments include certain explorations of new classical feedback systems towards better control of certain classes of interferometers; previously reported work [6] on an optodynamical atom–cavity system that hosts a coherent quantum feedback phenomenon, wherein the dissipation of the cavity steers a non-equilibrium state of the atomic spins toward a certain steady-state property; as well as forays into ultracold photoassociation of the atoms within the optical cavity.

In this work I also present a new theoretical treatment of the optodynamical feedback system, deriving and solving the quantum Langevin equations that describe the system.

Through this analysis I develop a model for the autonomous stabilization of the mean spin projection onto the cavity axis, which has been described previously [6, 7]. Further, I show that the same equations lead to the autonomous entanglement of the spins with fluctuations along the field axis damped to a value smaller than that of an analogous coherent (unentangled) spin state. For a fiducial set of parameters, I predict that at intermediate times, the reduced state of the spin sector is unconditionally squeezed, and that it is conditionally squeezed for as long as the model holds. I present a preliminary phase diagram visualizing the regions of parameter space that the system exhibits squeezing.

In the remainder of this chapter, I introduce the relevant physics and experimental tools used for the work in this dissertation, including ultracold atomic clouds, high-finesse optical cavities, and additional background information. Also in this chapter is an account of my journey through graduate school.

1.1 Ultracold atomic clouds and dispersive coupling

Atoms, as the building blocks of matter, have long been central to both theoretical and experimental explorations of quantum mechanics. Over the decades, numerous new experimental platforms have been introduced and the collection of realizations of quantum systems is vast and still growing. It includes the "artificial atoms" of superconducting qubits [8–14] and quantum dots [15–17], crystalline impurities [18–24], nonlinear optical systems, and more. But unlike larger composite quantum systems, individual atoms of the same element and isotope are fundamentally identical. It is also often possible to prepare large samples of atoms quickly and control or even switch off their interactions.

In our work we start with atoms inside an ultra-high vacuum chamber to isolate them from collisions with air molecules. Interfacing with them then consists of shining coherent laser light of controlled frequency, intensity, and polarization on them; producing and controlling the static electromagnetic fields and field gradients that form their environment; and generating radio-frequency or microwave radiation that couples their internal states. An atomic cloud has a distribution of atomic velocities that depends on the cloud temperature. This distribution leads to varying Doppler shifts between the atomic transition frequencies and the frequencies of incident radiation. To control the internal degrees of freedom of the atom, we cool them [25] to a temperature sufficiently low that the relative Doppler shifts are much smaller than all other relevant frequency scales, freezing out their motional degrees of freedom. This is an important step for us to be able to engineer the interactions among the atoms [26–28] and between the atoms and the rest of the universe (including incident radiation).

In this dissertation I describe work performed using rubidium atoms, which each have 37 protons and electrons; specifically we work with atoms of the ^{87}Rb isotope, which each have 50 neutrons. As an alkali atom, most of the electrons in the structure of rubidium form complete shells except for one lone valence electron. The ground state of the rubidium atom has the valence electron in the $5s^1$ state, and its lowest-energy excitations are those in

which only the valence electron is excited to a higher-energy state. In this way we reduce the complexity of the full ^{87}Rb atom—with 37 mutually repulsive electrons all bound to a nucleus with 87 nucleons—to a remarkably simple system in which we need only consider a discrete set of bound states of one single electron in an effective nuclear potential, plus the transitions among those states. Even further, we will neglect most of these remaining states because only a very few transitions will be nearly resonant with the laser fields. We prepare the atoms in one of these states through decay of the excited states to various ground states and deterministic optical pumping of atom populations from all other ground states into one. The radiation fields we apply to the atoms are chosen to be nearly resonant with a given electronic transition, as is the case for the cooling, repumping, imaging, and photoassociation laser fields, as well as the radio-frequency fields; or far enough from resonance that the details of many individual states can be simplified into effective off-resonant coupling strengths, as is the case for the cavity pump light that has significant contributions from several excited hyperfine structure states, and the cavity optical dipole trapping light that has significant contributions from transitions to several excited fine structure states: the $5S_{1/2} \rightarrow 5P_{1/2}$ (D_1) and $5S_{1/2} \rightarrow 5P_{3/2}$ (D_2) transitions with wavelengths near 795 nm and 780 nm, respectively.

In the photoassociation work reported in Ch. 5, the driving lasers are nearly resonant with the molecular transitions, where determining the frequencies and coupling strengths of these transitions presents much of the complexity. But in the portion of the work dealing with the atoms as spins, we consider driving light detuned far from the transitions to the excited states such that the overall effect is to produce simple "light shifts" to the energies of the Zeeman sublevels of the ground state [29], which greatly simplifies the analysis.

Alkali atoms have ground states characterized by a hyperfine splitting on the scale of ∼1 GHz. This splitting represents the energy difference between alignment and anti-alignment of the electronic spin angular momentum and the nuclear spin angular momentum (as the ground state has electronic orbital angular momentum $\ell = 0$). The nuclear spin of ^{87}Rb is 3/2. The hyperfine interaction couples this with the spin 1/2 of the electron to form two ground-state manifolds with total atomic angular momenta $f = 1$ and $f = 2$ that are split in energy by the hyperfine interaction strength $E_{\mathrm{hfs}} = h\nu_{\mathrm{hfs}}$. For ^{87}Rb, this frequency is $\nu_{\mathrm{hfs}} = 6.834\,682\,610\,904\,29(9)$ GHz [30]. The $f = 1$ and $f = 2$ states each have $2f + 1$ sublevels distinguished by their magnetic quantum number. These sublevels are non-degenerate in a magnetic field due to the Zeeman effect.

We initialize $N_{\mathrm{a}} \sim 2 \times 10^3$ atoms in the $f = 2$ hyperfine manifold of the electronic ground state, to which we couple one or more lasers. In the spin work, we use one laser of frequency ω_{p} that pumps the optical cavity mode (frequency ω_{c}) nearly resonantly, but that is off-resonant from the $5S_{1/2} \rightarrow 5P_{3/2}$ (D_2) atomic transition of angular frequency ω_{a}. Specifically I define ω_{a} to be the frequency of the D_2 cycling transition between $F = 2$ and $F' = 3$. We work in terms of the cavity–atom detuning $\Delta_{\mathrm{ca}} = \omega_{\mathrm{c}} - \omega_{\mathrm{a}}$ and work in the "dispersive" limit where the magnitude $|\Delta_{\mathrm{ca}}|$ is much larger than the natural linewidth of the transition $\Gamma = 2\pi \times 6.065(9)$ MHz [31] and also much larger than the resonant cavity–atom coupling strength. In this limit, we consider atomic excitation to be rare; we consider the primary effects of the light on the atoms to be coherent energy shifts (light shifts) determined

by summing the contributions from the sublevels of the excited states. This contains scalar, vector, and tensor components, which depend on ${m_F}^0$, ${m_F}^1$, and ${m_F}^2$, respectively, where m_F is the magnetic quantum number of the total atomic angular momentum. This sum simplifies in the case that the magnitude of the detuning is much larger than the scale of the excited-state hyperfine structure, which in ^{87}Rb contains shifts of $\Delta_{f'} = \{-302, -230, -73, +194\}$ MHz [32]. For $|\Delta_{\mathrm{ca}}| \gg |\Delta_{f'}|$, the tensor light shift becomes negligible, and we only consider the scalar and vector shifts.

If the detuning has even larger magnitude then the shifts simplify further. For detuning magnitude much larger than the fine structure interaction, the contributions from the D_1 and D_2 lines cancel and the light shift simplifies to just the scalar shift. The optical dipole trapping light we use approaches this limit, but the residual vector shift from the ODT light still reduces the spin coherence time of our spin ensembles [7].

In the dispersive limit, the atoms remain within the $f = 2$ ground state manifold, which forms a spin-2 system. One further simplification is that due to the tight spatial confinement of the atoms in our experiment, all atoms couple nearly identically to the optical cavity mode, so that we can consider the state of the spin system at all times to be symmetric with respect to interchange of any two individual spins; this allows us to consider just the collective spin $\hat{\boldsymbol{F}} = \sum_i \hat{\boldsymbol{f}}_i$, reducing the complexity from N_{a} spin-2 systems to one single spin of magnitude $F = 2N_{\mathrm{a}}$.

As quantum systems become larger they ordinarily tend to become more classical in nature as the collective zero-point fluctuation becomes a fractionally smaller effect. But there is great interest in studying non-classical effects in large systems. States with quantum entanglement can be used for measurements with sensitivity beyond the standard quantum limit (SQL), the limit of measurement when using unentangled states [33–36]. Non-classical effects in large systems can also be used to study the transition across the boundary of where we typically consider classical physics to apply [37, 38]. The coupling of a localized atomic cloud to the mode of a high-finesse optical cavity provides can provide strong interaction between light and a collective matter degree of freedom and facilitate high-sensitivity measurements of the cloud by the light transmitted through the cavity.

1.2 Dispersive cavity quantum electrodynamics

Light scattering by atoms in free space causes information to be carried away by photons traveling in all directions. This decay of atomic excitations is a consequence of the continuum of electromagnetic field modes (the vacuum) to which the atoms are coupled. Enclosing the atoms within a high-finesse[1] optical cavity enhances the coupling to a single optical mode. In our system we use two slightly concave, extremely highly reflective mirrors that share an optical axis and are separated by a distance much smaller than their radii of curvature, to form a Fabry–Pérot cavity. We call the resonant coupling strength between the cavity

[1]The finesse $\mathcal{F}$ can be understood as the number of round trips that light makes on average within the cavity before leaking out of the cavity.

mode and an atom g_0 and I take it to be the strength on the cycling D_2 transition between $F = 2$ and $F' = 3$. The coupling strength depends on the cavity mode volume, the cavity finesse, and the atomic transition strength, and the position of the atom because of the spatial variation of the cavity field amplitude. We write $g_0(\boldsymbol{r})$ for an atom at position $\boldsymbol{r}$.

This enhancement of the coupling between an atom and an optical mode can be strong enough that the mode exchanges energy coherently with an atom faster than the atom can decay to free space. We quantify the competition between the coherent exchange and the incoherent decay to free space modes with a parameter known as the cooperativity:

$$C = \frac{g_0^2}{\kappa \Gamma} \tag{1.1}$$

The cooperativity depends on the resonant coupling strength and the decay rates of both the atom and the cavity: κ is the field decay rate of the cavity (the half-linewidth) and Γ is the natural linewidth of the atom. Cooperativity much greater than unity indicates that an excitation will coherently oscillate between the atom and cavity before it decays. The cavity used for the work described in this thesis has the value $C_{\mathrm{QED}} \approx 16$ for the D_2 cycling transition between $F = 2$ and $F' = 3$.

Rather than working with the cavity resonant with the atoms, we detune our cavity far from the atomic transitions such that the atoms are very rarely actually driven to their excited states. Instead, we consider the atomic excited states to be adiabatically eliminated [39] from the dynamics of the system such that the dominant effects of the cavity on the atoms are Raman transitions among the atomic states within the ground-state hyperfine manifold, which are described by second-order perturbation theory. The strength of this process scales with the dispersive coupling $g_{\mathrm{c}} = g_0^2/\Delta_{\mathrm{ca}}$ and causes a level repulsion that introduces frequency shifts to both the cavity mode and the atomic states.

The dispersive shift of the cavity is one of our main experimental observables, providing a window into the atomic dynamics through its weak continuous measurement. The light shift on the atomic states, meanwhile, produces not only an average frequency shift of the entire ground state manifold, which has little effect in our experiment, but *differential* shifts of the magnetic sublevels: for large Δ_{ca} and a circularly polarized cavity field, this shift is linearly proportional to the magnetic quantum number and thus resembles the Zeeman effect of a weak magnetic field [40]. For this reason, the phenomenon is known as a fictitious magnetic field of light, sometimes called the optical magnetic field $\boldsymbol{B}_{\mathrm{opt}}$. The interplay between the dispersive shift of the cavity and the fictitious field acting on the atoms is rich and leads to a variety of optodynamical phenomena.

For $|\Delta_{\mathrm{ca}}| \gg g_0$, we find that $|g_{\mathrm{c}}| \ll g_0$. The collective dispersive strong coupling limit is defined by $N_{\mathrm{a}}|g_{\mathrm{c}}| \gg \kappa, \Gamma$ [41].

1.3 Cavity optomechanics and spin optodynamics

The spin experiments and theoretical analysis I report in this dissertation are part of the growing field of cavity spin optodynamics, which examines the effects of coupling between a

spin and a cavity mode. This field builds on the closely related field of cavity opto*mechanics*, in which the optical cavity mode is coupled to one or more mechanical degrees of freedom. Cavity optomechanical systems consist of, for example, a cavity mirror mounted on a cantilever [42], or an atomic ensemble dispersively coupled to the cavity mode [43]. Developments in cavity optomechanics have enabled demonstrations of quantum effects including entangled [44, 45] and squeezed states of mechanical oscillators [46, 47], squeezed states of light generated through the optomechanical interaction [48], and ground-state cooling of mechanical oscillators and observation of the associated sideband asymmetry [49]. Cavity spin optodynamics, in the case that the axes of the external magnetic field and the cavity are orthogonal, has analogies to cavity optomechanics [50]. But in the general case of a non-orthogonal cavity–field configuration, spin optodynamics offers certain features absent in cavity optomechanics such as the possibility of quantum-nondemolition (QND) measurements in the case of cavity–field alignment, or the case of a field tilted at an intermediate angle relative to the cavity, which is the subject of the analysis reported in this dissertation. My work builds directly on prior work performed with the same optical cavity and apparatus I have had the opportunity to use. These prior works include studies of optomechanics [51–53], spin optodynamics [54], and a hybrid combination of the two [55]. Recently, the E3 team performed continuous measurements of the atom number of a cloud and used the dispersive shift of the cavity to monitor the evaporative cooling process [56].

1.3.1 Introduction to atom–cavity interactions

Atoms can absorb light by undergoing a change in their electronic state from some state to another of higher energy, if the transition between those states obeys the selection rules describing the state of the atom and the incident photon. Excited atoms can relax to a lower-energy state by releasing a photon, a process that generally occurs spontaneously and can also be stimulated by an incident photon with the same quantum numbers. In free space, atoms couple to the continuum of electromagnetic field modes. In an optical cavity, the couplings are modified, with certain modes being strongly preferred by the cavity boundary conditions. An excitation of a cavity mode can be transferred into an atomic excitation and an atomic excitation can be transferred to the cavity. For simplicity, in cases where the energy spacing between different cavity modes is large, we can consider just a single mode of the cavity while all others are assumed to be far from resonance with both the light pumping the cavity and with any relevant atomic transitions. Similarly, we can often treat the atom as approximately a two-level system, where we assume the atom has one ground state and only one excited state coupled to that ground state by the cavity mode. The Jaynes–Cummings model [57] describes a single two-level atom coupled to a single mode of an optical cavity. The two-level picture is a useful but limited conceptual starting point. To appropriately model our system we will need to consider multiple ground state levels, which form our spin, and multiple excited state levels, which give rise to an effective form of the dispersive interaction that behaves like a fictitious magnetic field. I consider this in detail in Ch. 3.

For a cloud of many identical two-level atoms all coupled to a single mode of an optical cavity, but without strong interactions between the atoms, we turn to the Tavis–Cummings model [58]. This model is commonly encountered in our field and depends, like the earlier Jaynes–Cummings model, on the electric-dipole and rotating-wave approximations. The former assumes that the electromagnetic field profile of the cavity mode varies so slowly over the spatial extent of the electron wavefunction that it can be treated as uniform, and the latter ignores the counter-rotating term of the interaction as it is (for optical frequencies) so far off-resonance that its effect is insignificant. The Hamiltonian is

$$\hat{H}_{\mathrm{TC}} = \hbar\omega_{\mathrm{c}}\hat{c}^{\dagger}\hat{c} + \sum_{i=1}^{N_{\mathrm{a}}} \hbar\omega_{\mathrm{a}}\hat{\sigma}^{i}_{e;e} + \hbar g(\boldsymbol{r}^{i}) \left[\hat{\sigma}^{i}_{g;e}\hat{c}^{\dagger} + \hat{\sigma}^{i}_{e;g}\hat{c}\right], \tag{1.2}$$

in terms of the cavity annihilation operator $\hat{c}$ and the two-level density operators acting on atom i given by $\hat{\sigma}^{i}_{\alpha;\beta} = |\alpha\rangle_i\langle\beta|_i$ where $\alpha, \beta \in \{g, e\}$ index the atomic ground and excited states, respectively. The atom–cavity coupling g quantifies the rate at which the exchange of an excitation between the cavity and an atom takes place. Without loss of generality, we will take g to be real, and write it as $g(\boldsymbol{r}) = g_0 U(\boldsymbol{r})$ where U is the spatially dependent dimensionless relative cavity mode intensity. For a near-planar[2] cavity such as ours, the TEM_{00} mode the spatial mode function has the form[3]

$$U(r, z) = e^{-2r^2/w_0^2} \sin^2(k_{\mathrm{c}} z), \tag{1.3}$$

in terms of the radial and axial coordinates r and z, respectively, as well as the cavity mode wavenumber $k_{\mathrm{c}} = 2\pi/780\,\mathrm{nm}$, and $w_0 = 25\,\mu\mathrm{m}$, the cavity mode waist [59]. In general this creates a position-dependent coupling that couples to motional degrees of freedom of the atoms and forms the connection to cavity optomechanics. In the present work we take the atoms to be positioned at an antinode of the cavity mode so that the spatial dependence is small.

The value of g_0 is critical in the design and characterization of a cavity and is given by

$$g_0 = d\sqrt{\frac{\omega_{\mathrm{a}}}{2\hbar\epsilon_0 V}}, \tag{1.4}$$

in terms of $d = 2.989\, e a_0$, the dipole strength of the atomic transition [31], and the mode volume of the cavity $V = \int d^3\boldsymbol{r}\, |U(\boldsymbol{r})|^2$ where $V \approx \pi w_0^2 L_{\mathrm{c}}/4$ for our near-planar cavity. Our system realizes $g_0 = 2\pi \times 13.1\,\mathrm{MHz}$.

1.4 My journey through the PhD

When I began my PhD, I had no experience with atomic, molecular, nor optical physics, and had little formal experimental training other than tinkering at home and my advanced

[2]The cavity length is much smaller than the radii of curvature of the mirrors, $L_{\mathrm{c}} = 250\,\mu\mathrm{m} \ll R_{\mathrm{c}} = 5\,\mathrm{cm}$.

[3]Both the divergence and the Gouy phase of the cavity mode are neglected because the cavity length is much smaller than the Rayleigh range $z_{\mathrm{R}} = 2.5\,\mu\mathrm{m}$.

laboratory class[4] in college. There were so many exciting fields suddenly accessible as a new graduate student at Berkeley and I wanted to make an informed choice, so I decided to do a few "rotations" to get my feet wet.

I first reached out to Professor Naomi Ginsberg, who kindly welcomed me into her research group. There I worked with Dr. Milan Delor on ultrafast pump–probe optical homodyne detection of molecular rotational dynamics in the liquid phase.

In my second semester of the program, I joined the group of Professor Mike Crommie, where Dan Rizzo taught me to operate a scanning tunneling microscope (STM), how to design topologically nontrivial graphene nanoribbons, and image topologically protected edge states in real space with the STM.

During my first summer in the program I followed a couple of my friends to work with Professor Alessandra Lanzara up the hill at the Lawrence Berkeley National Laboratory, Materials Sciences Division. In our laboratories in Building 2 and in our frequent use of beamlines 4.0.3 and 7.0.2 of the Advanced Light Source (ALS), I learned to perform angle-resolved photoemission spectroscopy (ARPES) on single-crystalline samples of superconductors, topological insulators, and other unusual materials. My mentors there were Sam Ciocys, Conrad Stansbury, and Nick Dale, and I often worked closely alongside Kayla Currier. Near the end of my time in the group I worked closely with a new student, Burhan Ahmed. We had various specializations of ARPES available in our laboratory including time-resolved ARPES using the tools of ultrafast pump–probe spectroscopy, and spin-resolved ARPES using a time-of-flight-based analyzer that reflected the collected electrons off a magnetic target. I sought training on operating beamline 4.0.3 from my peers in the group and from Jonathan Denlinger, the incredible beamline scientist there. Once I could reliably operate it, I formed a productive collaboration with my friends and colleagues in the Analytis group: they grew samples, and I brought them up the hill on the shuttle, loaded them into the chamber, cooled them down, cleaved them, and collected ARPES data in marathon overnight and sometimes multi-day sessions. I measured a great variety of materials (including from other crystal growers), including electron-doped cuprate superconductors alongside Kayla Currier; beautiful purple bronze samples that conduct along only one axis, grown by Vikram Nagarajan; some vanadium(III) iodide crystals [60] that posed a fun puzzle because the material is an insulating ferromagnet, which is a formidable situation for ARPES due to charging effects and sensitivity to magnetic fields; and also because it is both hygroscopic and water-soluble, which together result in a property called deliquescence—exposure to air turns these crystals into a liquid. There was no way to load samples into beamline 4.0.3 without exposing them to air, so I did the best I could: I used a glovebox in a different part of the ALS to prepare the samples, enclose them within a small metal container with an o-ring seal before removing them from the glovebox. Then I would power-walk around the ALS ring as fast as I could without being asked to leave the facility, then rapidly open the container, load the sample in, and pump down the chamber. In this way I was able to minimize the exposure of the

[4] I designed and built my first experimental setup in this class: a Michelson interferometer with a green laser pointer that measured the variation of the index of refraction of water with temperature.

crystal sufficiently to perform ARPES on it. But one of my most successful endeavors was in measuring the photoemission signals on undoped and tin-doped $CeCoIn_5$ crystals grown by Nikola Maksimovic. This collaboration started when I was hanging out in the Analytis group office and asked if there were any new samples for which their investigations might benefit from ARPES data. Nikola explained the situation with his measurements on the material at the time and how there was some uncertainty that might be resolved by ARPES; we figured out together exactly where to look within the Brillouin zone of the material for a signature. I was able to collect data that proved critical in supporting a controversial claim about an unusual phase transition in the material [61].

After that, I decided to pursue more work with lasers, and my attention turned to reviving a tantalizingly exciting, but troubled, new optical spectroscopy setup that had been built and abandoned by a postdoc in the group. It used a high-power ultrafast Ti:sapphire amplifier operating at 800 nm wavelength that output 13 mJ, 70 fs pulses at a 1 kHz repetition rate that fed multiple nonlinear-optics stages downstream: optical parametric amplifier (OPA) and difference-frequency generation (DFG) stages with which we could generate intense pulses with a center wavelength tunable from about 1.2 µm out to about 20 µm that we used as an ultrafast pump, as well as a ZnTe crystal that we used to produce terahertz pulses used as a probe. In this way we were nominally capable of doing pump-probe spectroscopy, probing in the terahertz band and with tunable pump throughout the mid-infrared (MIR) spectrum. This was exciting because there was a buzzy idea in the field of resonantly driving some coherent mode in a material and observing its effect on out-of-equilibrium electronic properties, such as potentially driving certain modes in superconductors or near-superconductors and looking for changes in the superconductivity to try to understand the different ingredients necessary for superconductivity. I was also working on coupling the MIR light into the existing main in-group ARPES chamber for MIR-pumped time-resolved ARPES experiments. But the experiments dragged on, and on, not because of difficulties with the samples or with challenges with the data, but because of technical difficulties with the lasers. The laser power was incredibly unstable which led to insurmountable fluctuations in the nonlinear conversion stages. I had to so regularly do touch-ups to the high-power amplifier that it consumed essentially all of my time, despite frequent efforts of the company's laser technician who was in our lab so often he seemed like a member of the group.

The PhD offers an opportunity for a student to take risks. From time to time, one might find a small window into a completely unknown space, and can choose to venture into it and seek new answers and even questions, doing bold experiments that may prove transformational, or may cause one to get completely lost and lose track of time. This project was to use ideas developed in the field of quantum materials where resonant MIR excitation was thought to possibly enhance or modify superconductivity, or in a proximate superconductor possibly drive the system into a metastable superconducting state, but apply them to a completely different system that also features metastable states and a complicated free-energy landscape: specifically, biological samples. More specifically: proteins, and even more specifically misfolded proteins such as prions. Could we take samples of misfolding or misfolded proteins and, through resonant excitation of some vibrational modes, modify their

energy landscape to either destabilize their misfolded conformations, or otherwise influence their folding dynamics? Could we enhance or diminish the activity of certain enzymes by resonantly exciting conformational changes?

It turned out the answer was no, at least in our case. There were multiple challenges: one was that the vibrational modes of interest, those associated with the large-scale tertiary structure of the proteins, would generally be found at far lower frequency than our available MIR tuning range. We held out hope that there might be some coupling between the higher-frequency vibrational modes associated with the primary and secondary structure might still selectively excite modes associated with the larger-scale structure. However, there was also a foundational problem: water is strongly absorptive of these frequencies of light, and it would generally be difficult to ensure that the light was actually reaching the proteins in the liquid and that any signal we observed was not due to heating of the water (we could imagine scanning the pump frequency and looking for resonant features not associated with absorption features in water, but my estimates of the thermal background effects made it hard to imagine practically achieving our goal without being much more creative in our experiment design). We gave it a good run, and through this experience I learned that I wanted to work with systems where one can more easily disentangle cause and effect. Throughout our studies of the interaction between an aqueous sample and a high-power laser, thermal effects caused by laser-heating of the water were overwhelming; it proved extremely challenging to detect spectroscopic signatures of profound effects such as resonantly driven conformational changes in proteins.

Ultimately, I recalled once more that a graduate student can afford to take risks, and decided to risk jumping into another field of research.

1.4.1 My time with E3

I reached out to Professor Dan Stamper-Kurn who warmly invited me into his group to work initially on a new experiment building a neutral-atom tweezer array in collaboration with several other professors and their groups. Eventually, funding and logistical constraints led me to change my path again: in early 2021, I found my way into a spot on Dan's third experiment in Berkeley, code-named E3. At the time, postdoc Dr. Josh Isaacs and graduate student Julian Wolf were running the experiment. They took me in and taught me the ropes. I had never previously worked with actively stabilized narrow-linewidth lasers, locking them, or tuning them away from mode-hops. In fact, I had relatively little experience working with feedback systems of any kind. Past experience had made me plenty comfortable with basic laser alignment and safety, but the routine tasks in an AMO lab of tuning up laser locks and coupling light into single-mode optical fibers were new to me. Josh and Julian trained me on these tasks and many more with plenty of patience.

I joined the experiment during a partial reconstruction of the vacuum chamber and bake. That meant that in my first few months, we were rebuilding a significant portion of the experiment: we needed to restore the atom source and the vacuum, but also many optics had been removed from around the chamber to make way for the construction and the

bake. In the aftermath, we recoupled light into the cavity and rebuilt the paths around the chamber. It also took significant effort to get the various stages of the experimental sequence working again, from cooling to magnetic trapping and transport and eventually dispersive measurement of the atoms in the cavity.

After the rebuild, we jumped straight into experiments on molecular photoassociation that were designed and led by Josh. It took some time to switch between the experimental configuration we needed for molecules and that for spins, so we would work on one for some time and then periodically pivot to the other while analyzing the data we had collected. It was a real crash course in AMO, and in the meantime I came up with various ideas to improve certain limitations of the apparatus, which I describe in Ch. 2. In coming to understand the spin-stabilization experiments, described in Ch. 3, I developed a suspicion that the feedback process could be reducing not just fluctuations of the mean spin but also fluctuations away from the mean. As time progressed I became convinced that if the cavity–spin system can stabilize the spin with coherent feedback, then it must also (for certain parameters) reduce the quantum noise of the spin. It took a while to work through these ideas, but I was able to develop an analysis that indeed demonstrates squeezing of the spin within the model we were studying for stabilization. This analysis forms the basis of Ch. 4 of this dissertation.

Over time, the vacuum pressure in the E3 system began to worsen, and we began to run into issues with the background-pressure-limited lifetime of atoms in our magnetic traps. This eventually prevented us from loading atoms into our cavity, and we focused all our attention on trying to repair the problem. We decided that it was not going to be worth very much more effort to try to restore it given finite resources, particularly graduate student time; ultimately the experiment decided to shut itself down. I describe the conclusion of the experiment at the end of Ch. 2.

1.5 Definitions, notation, and conventions

I strive to follow certain typographic conventions throughout the work. Boldface quantities (such as $\boldsymbol{B}$) represent variables with vector values, and use a caret (such as $\hat{n}$) to distinguish quantum mechanical operators. I will generally introduce new variables with the $\equiv$ sign, and use one of $\simeq$, $\approx$, and $\sim$ in a line to indicate that an approximation has been made in the prior step to arrive at that expression (with which symbol depending somewhat loosely on how I feel about that approximation).

The vector operator $\hat{\boldsymbol{F}}$ and its components $\hat{F}_x$, $\hat{F}_y$, and $\hat{F}_z$, as well as the ladder operators $\hat{F}_\pm$, refer to unitless operators acting on a collective spin F while lowercase operators $\hat{\boldsymbol{f}}$ act on an individual atomic spin f. The operators $\hat{c}^\dagger$ and $\hat{c}$ are the unitless creation and annihilation operators of the bosonic optical cavity field and satisfy the commutation relation $[\hat{c}, \hat{c}^\dagger] = 1$. I define the amplitude and phase quadratures of the optical cavity fields with normalization

$$\hat{c}^{\mathrm{AM}} = \frac{1}{\sqrt{2}}\left(\hat{c}^\dagger + \hat{c}\right) \qquad \hat{c}^{\mathrm{PM}} = \frac{\imath}{\sqrt{2}}\left(\hat{c}^\dagger - \hat{c}\right) \tag{1.5}$$

and commutator $[\hat{c}^{\mathrm{AM}}, \hat{c}^{\mathrm{PM}}] = \imath$. The definitions for quadratures of $\hat{b}$, the fluctuation of the optical cavity field away from its mean, and for the optical vacuum input $\hat{\xi}$, are analogous, and $\hat{\xi}$ is taken to satisfy $[\hat{\xi}(t), \hat{\xi}(t')] = \delta(t - t')$.

Chapter 2

Experimental hardware

The work described in this dissertation was performed with our experimental apparatus known internally as E3. In tradition, it was named for its timing as the third apparatus constructed in the Stamper-Kurn group at Berkeley. In early 2021 I first visited the E3 lab room that would become my academic home for the remainder of my PhD. E3 had seen several generations of graduate students by that point, and I was not the first to think that I would be the last. In my time with E3, my coworkers were (in addition to my advisor Dan), my mentors Dr. Joshua Isaacs and senior graduate student Julian Wolf, as well as visiting master's degree student Kevin Mours. It would be some months' time before I was set to work full-time on E3, having dabbled in that time with spinning up an ill-fated new optical tweezer atom array experiment to be dubbed "EX" but which was ultimately spun back down in November 2021.

The heart of E3 was a silicon chip plated with wires used to create strong magnetic field gradients at the location of a cloud of cooled atoms [59]. High-reflectivity mounted with the chip in vacuum, arranged to be near planar, formed a high-finesse optical cavity that shined through a fabricated hole in the chip. As shown in Fig. 2.2, the apparatus actually hosted a pair of side-by-side optical cavities, and thus four mirrors total. This provided a choice of cavity parameters accessible without breaking vacuum. In my time in the group, and to my knowledge in the entire history of the experiment, only one cavity (the "one-sided" cavity) was ever used for science. In the experimental sequence, atoms were cooled and trapped and shuttled magnetically into the cavity, tightly compressed in the magnetic trap and then transferred to an optical trap formed from an off-resonant cavity mode. The strong field gradient generated by the atom chip wires was necessary to achieve sufficient compression of the atomic cloud to achieve symmetric (spatially uniform over the size of the cloud) coupling to the cavity mode. Outside the vacuum chamber, the rest of E3 was a lab room full of equipment: optical tables, lasers, optics, a small secondary vacuum chamber housing a "reference" cavity, electronics, cables, fibers, computers, labels, HVAC systems stabilizing the lab environment, and a lead brick.

As I describe in Sec. 2.6, we decommissioned and disassembled E3 in late 2023.

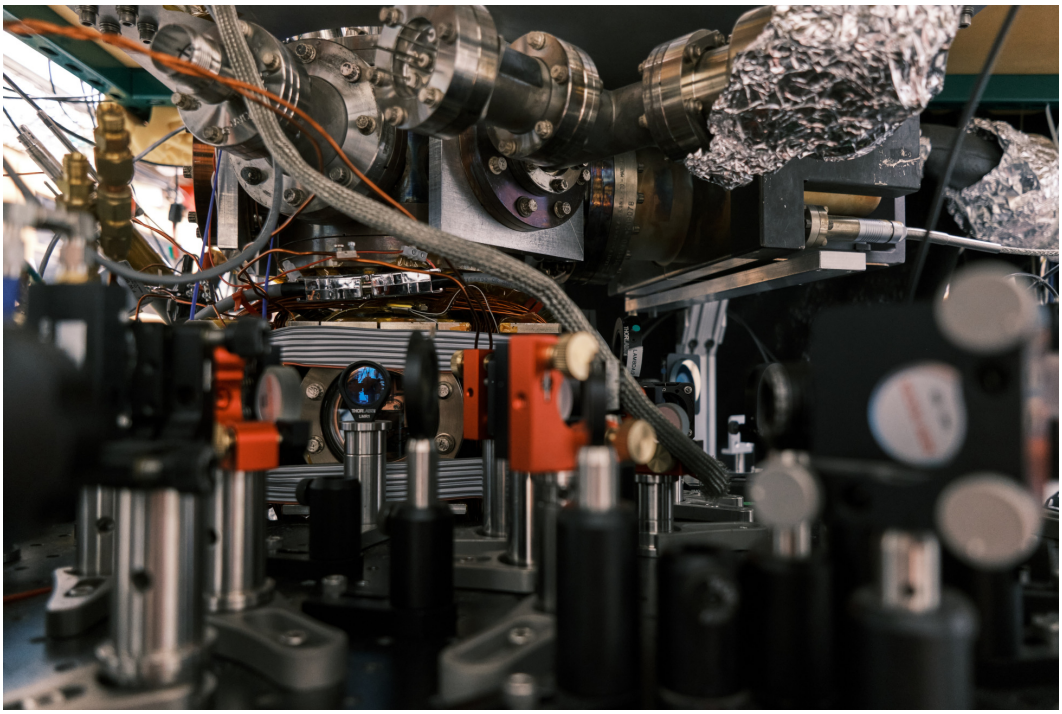


Figure 2.1: Photograph of the E3 vacuum chamber surrounded by optical, vacuum, and electrical equipment. The optics in the foreground combine the cavity pump and optical dipole trapping light and couple them into the optical cavity through the west viewport, visible in the center. External electromagnetic coils, plumbing, and vacuum feedthroughs are visible, as well as the ion pump in the upper right. This view is about level with the optical paths and is above the breadboard that surrounded the chamber.

2.1 Preparation of the atomic sample

The experiments in E3 described here rely on the production of ultracold samples of 1000-2000 atoms coupled *symmetrically* to a high-finesse optical cavity. Symmetric coupling requires that the atoms be positioned within the optical cavity in a cloud (or multiple clouds) with very thin extent along the cavity axis; in particular, the extent of the cloud along the cavity axis must be significantly smaller than the periodicity of the cavity pump light to minimize spatial averaging of the atom-cavity coupling strength. Today, one might design an apparatus to achieve this by loading atoms into one or more optical tweezers; this technology was less developed at the time of E3's commissioning, and a different approach was selected. Atoms are instead trapped in an far-off-resonance standing-wave optical dipole trap (ODT) formed by a second driven cavity mode. The spatial extent of each well of this potential is small enough along the cavity axis to provide nearly symmetric coupling, if the atoms can be loaded into a single well. This is far too small a region to serve as the initial atom trap, and the atoms must first be cooled before loading into such a trap, so the

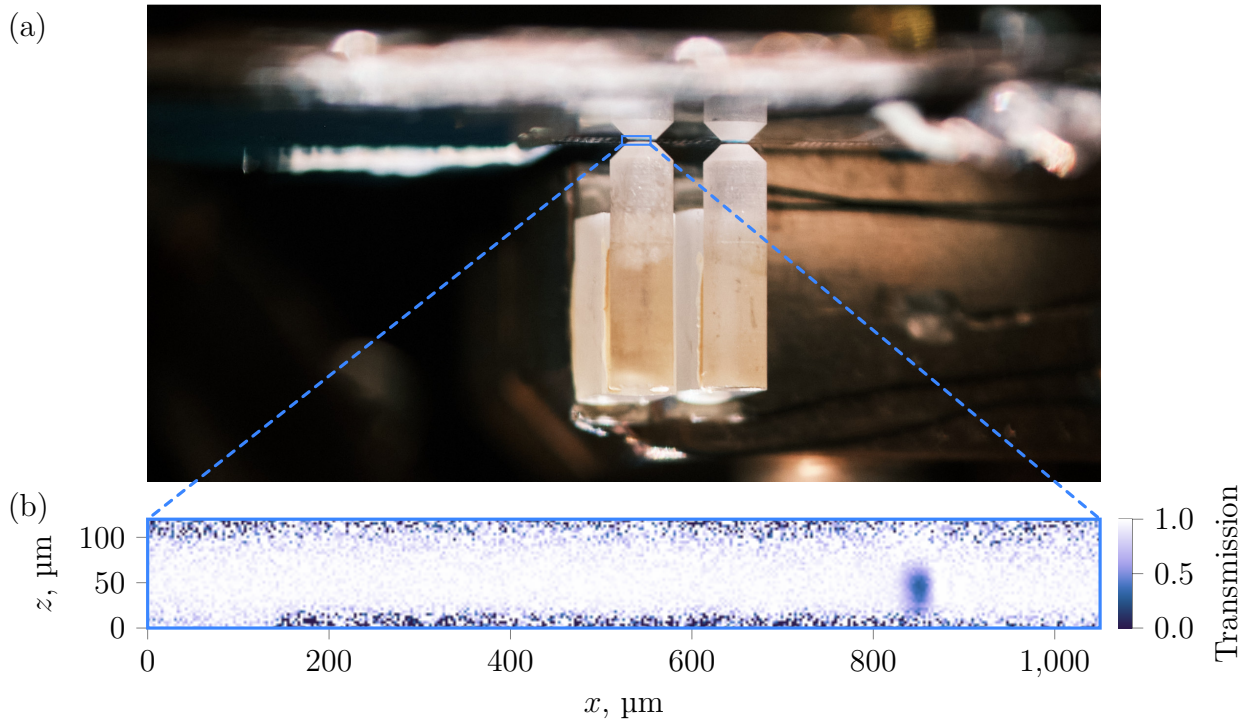


Figure 2.2: (a) The E3 chamber holds two side-by-side high-finesse optical cavities, here seen through the north viewport used for optical imaging and pumping. The lower mirror of each cavity is visible. The reflections of the lower mirrors are visible on the surface of the atom chip. The upper mirrors sit behind the atom chip in essentially the same positions as the reflections. (b) Representative time-of-flight absorption image of a cloud of ~ 2000 ^{87}Rb atoms within the optical cavity after 400 µs time-of-flight. Absorption measures local atom column-density along the propagation of the imaging light; lower transmission indicates higher atomic density. The shadows of the atom chip and the lower cavity mirror are visible at the top and bottom of the image, respectively.

experimental sequence consists of a number of steps before this point.

Atoms are first cooled and trapped in a magneto-optical trap (MOT), then undergo a series of slightly different cooling, compression, and spin-polarizing processes before they are able to be loaded into an initial magnetic trap. Due to the spatial constraints imposed by the optical cavity mirror substrates, these steps must take place away from the cavity volume for the cooling laser beams to fit. The system makes use of intricately designed in-vacuum coils and wires on an in-vacuum chip substrate to translate the magnetic trap from the initial preparation region into the optical cavity. The chip wires generate strong enough magnetic confinement that the spatial extent of the atoms in the trap is comparable to the size of a single well of the cavity-mode ODT. Once the magnetic trap is co-located with the ODT, the ODT light is ramped up and the magnetic trap is released, leaving the atoms optically

trapped and ready for experimentation.

2.1.1 Initial cooling and trapping

Rubidium atoms begin their journey through the E3 vacuum chamber by sublimating off the surface of a 5 g sample of solid Rb exposed to the vacuum; some of them find their way to the magneto-optical trap (MOT) region of the chamber. The initial MOT is formed by one horizontal pair of counter-propagating laser beams, and two pairs of counter-propagating laser beams that pass through the MOT region at 45° angles from vertical, and that each reflect in-vacuum off three mirrors: two with normal vectors in the horizontal plane, and one with a normal vector along the vertical axis. An in-vacuum coil (through the center of which the non-horizontal MOT beams travel for optical access convenience), in addition to external bias coils, generates the magnetic field for the MOT. The MOT collects approximately 10^8 atoms at a temperature $\sim 1\,\mathrm{mK}$.

The size of the atom cloud in the initial MOT is too large to to be loaded efficiently into the magnetic trap we use, so once the initial MOT is loaded, the laser detuning is increased to compress the cloud. The atoms are then transferred into the "chip MOT" with magnetic fields partially generated by the chip wires. Next, the field is briefly zeroed and while the atoms are released they undergo polarization-gradient (PG) cooling [62, 63] and optical pumping [64, 65]. The currents then switch back on to catch the polarized atoms in a magnetic trap; at this point the trap holds approximately 10^7 atoms at $\sim 15\,\mu\mathrm{K}$.

2.1.2 Magnetic trapping and transport

The first magnetic trap generated in the E3 experimental sequence is located at the beginning of a magnetic conveyor system. In preparation for transport, an applied radio frequency (rf) "knife" cools the atoms by forced evaporation, leaving $\sim 5 \times 10^5$ atoms at $\sim 2\,\mu\mathrm{K}$. The conveyor system uses periodically varied currents in a pair of spatially out-of-phase squiggly wires on the chip to first accelerate and then horizontally transport the position of the magnetic trap at close to a constant velocity, until the trap approaches the end of the conveyor at which point the trap decelerates and comes to rest at a precisely determined position within the optical cavity. Acceleration and deceleration serve to make the ride as smooth as possible for the atoms, but nevertheless the process still heats the gas and atoms are lost from the trap in transit; the surviving ones arrive at elevated temperature, too hot to load mostly into a single well of the ODT. A second stage of evaporative cooling at the final magnetic trap location lowers the cloud temperature to facilitate site-selective loading of the ODT.

2.1.3 Optical dipole trapping

Once the magnetic trap has arrived in the cavity and the second stage of evaporation is complete, the magnetic trap switches off and the ODT intensity ramps up to hold the

atoms. The ODT wavelength is $\lambda_{\mathrm{ODT}} = 842\,\mathrm{nm}$ which is red-detuned from the D_1 and D_2 transitions and produces a conservative attractive potential at the antinodes of the standing wave. These potential wells repeat spatially every $\lambda_{\mathrm{ODT}}/2 = 421\,\mathrm{nm}$ as the optical potential is proportional to the intensity of the light field. The cavity pump light at 780 nm wavelength and the cavity ODT light at 842 nm wavelength are incommensurate with a moiré wavelength of $[(780\,\mathrm{nm})^{-1} - (842\,\mathrm{nm})^{-1}]^{-1} = 10.6\,\mu\mathrm{m}$, while the moiré wavelength of the intensities is $[(780\,\mathrm{nm}/2)^{-1} - (842\,\mathrm{nm}/2)^{-1}]^{-1} = 5.3\,\mu\mathrm{m}$. As the pump and ODT half-wavelengths are significantly less than this, precise alignment of the tightly confined magnetic trap with an individual well of the ODT allows tuning of the coupling strength, ranging from maximum coupling if the atoms are localized in an ODT well aligned with a pump antinode, minimum coupling for a pump node, or an intermediate coupling maximally sensitive to displacements of the atomic cloud for an ODT well halfway between the pump node and antinode. For the work in this dissertation, the atoms are placed close to the pump antinode to maximize coupling and minimize the sensitivity of the coupling to displacement. The system is able to load up to 4000 atoms at temperatures around 3 µK, as measured by time-of-flight absorption images such as Fig. 2.2.

The ODT confines the atoms tightly in the axial (cavity) dimension and more weakly in the radial direction because the axial confinement is on the scale of the wavelength $\lambda_{\mathrm{ODT}} = 842\,\mathrm{nm} = 2\pi/k_t$ where k_t is the wavenumber of the trapping light, while the radial confinement is on the scale of the cavity mode waist $w_0 = 25\,\mu\mathrm{m}$. The cloud extent is about 100 nm in the axial direction and 5 µm in the radial direction [59]. At the low temperatures of the gas, the confinement is nearly harmonic; for a typical trap potential depth U_t we realize harmonic trap frequencies $\omega_m = \sqrt{2k_t^2 U_t/m} = 2\pi \times 150\,\mathrm{kHz}$ in the axial direction, and $\omega_r = \sqrt{4U_t/{w_0}^2 m} = 2\pi \times 1.2\,\mathrm{kHz}$ in the radial direction, with m the atom mass.

Once the atoms are held optically in the cavity, they are ready to be used in an experiment probing the interaction of the atoms and the near-resonant cavity mode.

2.2 The science cavity

Atoms trapped in the standing-wave ODT of the cavity are probed with a second driven TEM_{00} cavity mode detuned from the atomic D_2 transition by $\Delta_{\mathrm{ca}} \approx 2\pi \times -40\,\mathrm{GHz}$, defined relative to the cycling D_2 transition between $F = 2$ and $F' = 3$. On resonance with this transition, the cavity mode has a coupling strength $g_0 = 2\pi \times 13\,\mathrm{MHz}$, and detuned by Δ_{ca} this yields a dispersive coupling strength $g_c = g_0^2/\Delta_{\mathrm{ca}} = 2\pi \times -4.2\,\mathrm{kHz}$. I show the relevant transitions and frequencies in Fig. 3.1.

At wavelengths near 780 nm the cavity has a finesse of $\mathcal{F} = 1.6 \times 10^5$ and half-linewidth $\kappa = 2\pi \times 1.82\,\mathrm{MHz}$. On resonance the system reaches the single-atom strong-coupling regime of cavity QED as indicated by the cooperativity $C = g_0^2/\kappa\Gamma = 16 \gg 1$.

The science cavity mirrors are mounted to either side of the atom chip at the location of a hole made through the chip such that the cavity mode shines through a hole. Piezoelectric transducers on the mounts allow for precision spatial control of the cavity mirrors and it

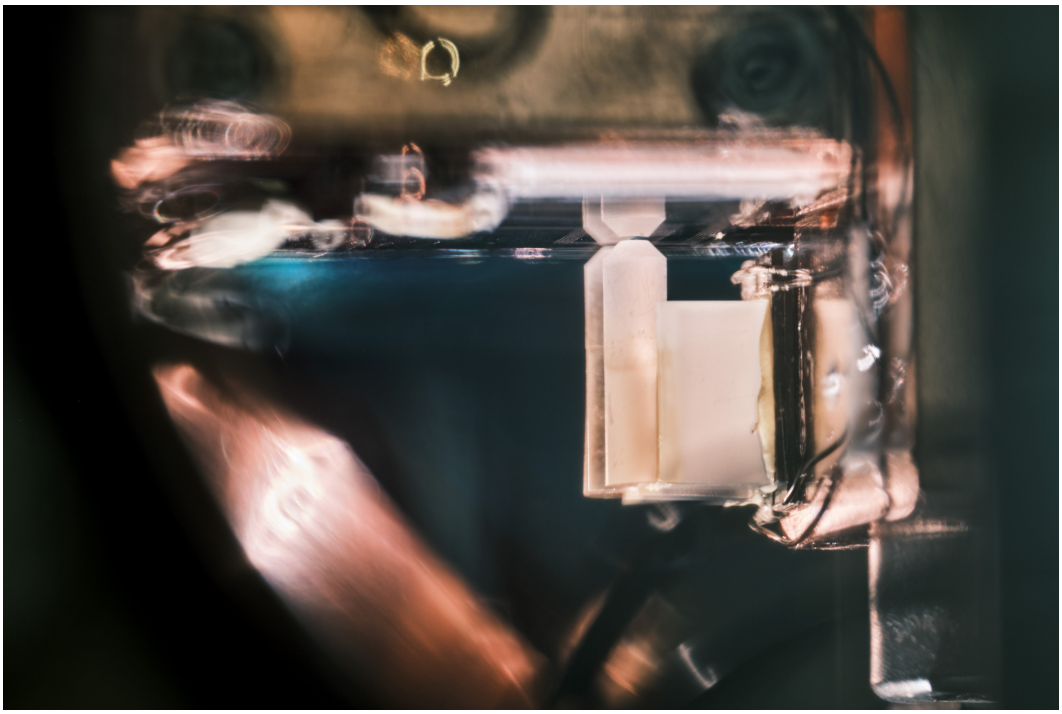


Figure 2.3: Another view inside the E3 vacuum chamber through the west viewport used for coupling light into the cavity. The lower mirrors of the two optical cavities are visible below the atom chip, while some of the atom chip magnetic wires and reflections of the lower cavity mirrors are visible on the atom chip surface. The cavity mirror mounting blocks and piezo control wires are visible to the right. In the lower left sits the in-vacuum MOT coil. Whereas the view of Fig. 2.1 was from above the breadboard mounted around the chamber, this view is from below the breadboard, looking slightly upwards.

is feedback of the ODT transmission error signal to the piezos that stabilizes the cavity frequency. The spacing of the cavity mirrors has historically been understood to be $L_c \approx 250\,\mu\text{m}$ which was determined from measurements of the free spectral range $\nu_{\text{FSR}} = c/2L_c$. It turns out that L_c can be determined with greater precision from co-resonance measurements as described in Sec. 2.2.1.

The mirrors are made from BK7 glass substrates that are each flat on the outer side and curved with a radius of curvature $R_c = 5\,\text{cm}$ on the inner side. The curved sides feature a dielectric coating with alternating layers of Ta_2O_5 and SiO_2. For the "one-sided" cavity used in the E3 experiments, the "input" mirror has 39 layers; the "output" mirror has 33 layers making it eight times more transmissive than the input mirror.

2.2.1 Longitudinal mode spectrum and co-resonance

The simple model of a near-planar Fabry-Pérot optical cavity consists of two highly reflective and infinitesimally thick surfaces separated by a distance L_c and predicts a transmission spectrum with peaks at wavelengths λ_m that divide $2L_c$ by an integer q: $\lambda_q = 2L_c/q$. This corresponds to frequencies $\nu_q = c/\lambda_q$ that satisfy $\nu_{q'} = \nu_q + (q' - q)\nu_{\mathrm{FSR}}$ where $\nu_{\mathrm{FSR}} = c/2L_c \simeq 599\,\mathrm{GHz}$, according to the historical specifications of the E3 science cavity.

The cavity is simultaneously driven by at least two lasers each resonant with a different longitudinal mode, the pump at wavelength approximately 780 nm and the trap around 843 nm wavelength. I will use a specific example: in May of 2019, these lasers were measured at $\nu_1 = 384.1850(1)\,\mathrm{THz} \leftrightarrow 780.333\,58\,\mathrm{nm} = \lambda_1$ and $\nu_2 = 355.728\,40(30)\,\mathrm{THz} \leftrightarrow \lambda_2 = 842.756\,61\,\mathrm{nm}$ during co-resonance[1]. Note that the difference frequency is not a multiple of the historically known ν_{FSR}: $\nu_1 - \nu_2 = 28.456\,61(40)\,\mathrm{THz}$ and $(\nu_1 - \nu_2)/\nu_{\mathrm{FSR}} = 47.51$. This apparent violation of the principle that longitudinal modes are uniformly spaced in frequency is heuristically explained by allowing the reflecting surfaces to have finite thickness, noting that for realistic reflecting surfaces must be a finite skin depth over which the reflected wave penetrates the reflecting medium but decays, and that the skin depth depends on the wavelength and the optical properties of the reflecting medium. It turns out that we can analyze the situation in greater detail and obtain a more satisfyingly concrete resolution.

To achieve the very high reflectivity necessary for a high-finesse optical cavity, the mirrors are typically made from multilayer dielectric coatings deposited on super-polished glass substrates. The design principle of a high-reflectivity dielectric mirror is analogous to that of an anti-reflection coating. The idea is to engineer the interference of light reflected from the interfaces between layers to be constructive (mirror) or destructive (anti-reflection) at wavelengths of interest by interleaving layers of high-index material with those of low-index material and choosing the layer thicknesses to achieve the desired interference condition. For high reflectivity, layer thicknesses L_i are optimally chosen when each layer is one-quarter-wavelength thick: $L_i = \lambda_0/4n_i$, where λ_0 is the vacuum wavelength of the light and n_i is the refractive index of the i^{th} layer. These layers can be deposited onto a substrate sequentially with very accurate control of the thickness of each layer. The calculations I describe here assume that the layers have optimal thicknesses for the D_2 line of ^{87}Rb.

The optical reflectance and transmission of an interface between two materials with different refractive indices are described by the Fresnel coefficients. With a stack consisting of multiple layers (and interfaces), incident light can traverse a large number of possible paths, reflecting off various interfaces or not, inside the layered stack before finally exiting having been reflected by the film or transmitted. The amplitudes of these partial contributions that ultimately reflect from the layered structure add, as do those that are ultimately transmitted. Fortunately, the optical transfer matrix method (TMM) accounts for the entire layered dielectric structure at once to simplify calculations [66, 67]. I used the conveniently avail-

[1] These values are known from Wavemeter measurement plus correction for AO offsets between the Wavemeter light and the light incident on the science cavity. Uncertainty of which diffraction order was used for an AO at the time leads to an uncertainty of about 300 MHz that does not affect the results here.

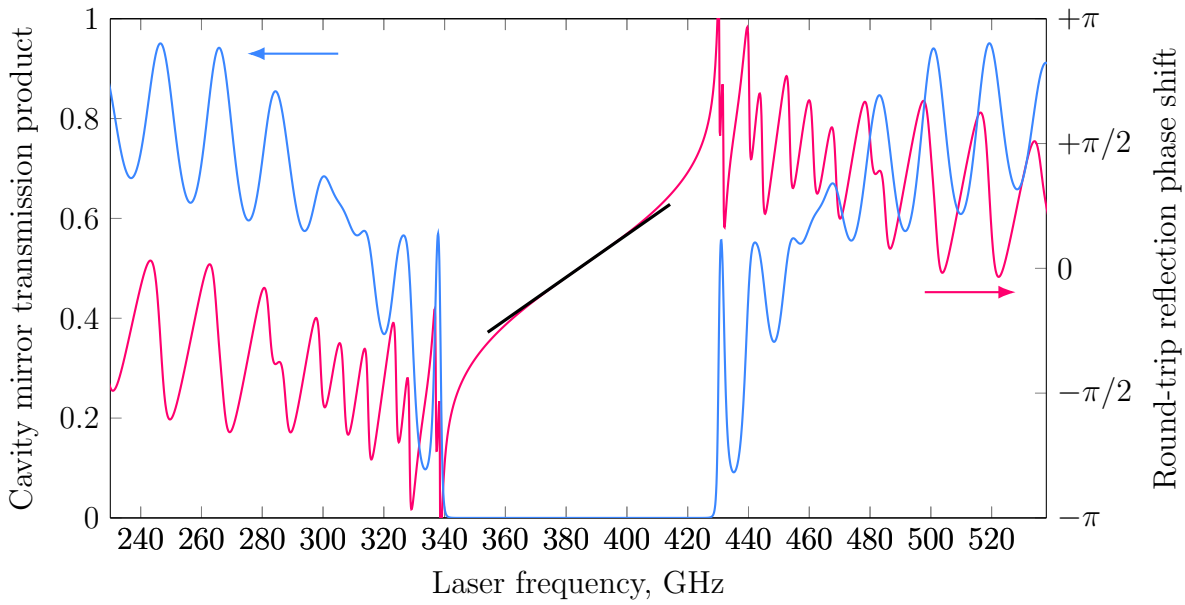


Figure 2.4: Calculations of the product of the power transmissions through the input and output mirrors, and of the sum of the phase shifts accumulated from reflecting off both mirrors. The dispersion discussed in the text is indicated by the black line.

able Python packages `tmm` [67] and `tmm-fast` [68] that implement the TMM and published data [69–72] on refractive indices $n_{Ta_2O_5}$ and n_{SiO_2} of Ta_2O_5 and SiO_2 at our wavelengths of interest (780 nm − 850 nm) to perform the numerical calculations in this section. The datasets I reference for $n_{Ta_2O_5}$ and n_{SiO_2} have a very similar wavelength dependence, but differ by about 2 %, likely related to differences in the preparation of the measured films. I check the analysis with each dataset and also use them in combination to infer statistics about the refractive indices, which I infer at 780.2 nm wavelength to be $n_{Ta_2O_5} = 2.094(20)$ and $n_{SiO_2} = 1.4694(50)$.

I consider the reflection and transmission of the entire cavity system at once rather than the simpler model that, for example, treats each mirror coating in isolation and abstracts them to surfaces of some determined (possibly wavelength-dependent) high reflectivity at either end of a certain distance of vacuum. This expression represents how I model the entire cavity structure:

$$\text{laser drive} \;\rightleftarrows\; \text{B(TS)}^{19}\text{TVT(ST)}^{16}\text{B} \longrightarrow \text{detector}$$

In this notation, B represents the cm-scale BK7 mirror substrate; T, one thin layer of Ta_2O_5; S, one thin layer of SiO_2; and V, the "layer" of vacuum. The periodic patterns are written in shorthand: for example, $(XY)^3 \equiv XYXYXY$. B is thick enough and its contribution small enough that we assume it to be infinitely thick in the calculation. The first thin layer, T has a thickness of $780.2\,\text{nm}/4n_{Ta_2O_5} = 93.1\,\text{nm}$. Similarly, S has a thickness of $780.2\,\text{nm}/4n_{SiO_2} =$

132.7 nm. The thickness of the vacuum layer is a variable in the simulations, initialized at the traditionally known value of 250 µm. Equipped with this multilayer model of the system, the TMM yields the full wavelength-dependent reflection and transmission spectra.

The transmission spectrum of the pair of mirrors (calculated in isolation, not as a cavity) and the total phase shift after round-trip reflections ϕ are shown in Fig. 2.4. The dispersion near the D_2 line is calculated as $d\phi/d\omega = 4.27\,\mathrm{PHz}^{-1}$. The estimated cavity length $L_c = 252\,\mu\mathrm{m}$ corresponds to round-trip phase $4\pi L_c/c = 10.565\,\mathrm{THz}^{-1}$. The sum of these two quantities is the total round-trip phase increment $\approx 10.592\,\mathrm{THz}^{-1} = 2\pi/\nu_{\mathrm{FSR}}$. The calculated free spectral range at this cavity length and frequency is

$$\nu_{\mathrm{FSR}} = \left(\frac{2L_c}{c} + \frac{d\phi}{d\omega}\right)^{-1} = 593.2\,\mathrm{GHz}. \tag{2.1}$$

The longitudinal mode spectrum is not perfectly linear and instead is a function of the mode index due to the frequency dependence of the mirror dispersion. Idealized mirrors without any dispersion would have simply led to $c/(2L_c) = 594.7\,\mathrm{GHz}$ which differs from the corrected expression Eq. 2.1 by about 1.5 GHz.

In principle, the non-linear longitudinal mode spectrum allows a comparison of two measured co-resonant laser frequencies and a TMM-type calculation of the resonant frequencies to identify the longitudinal mode index uniquely. I show this in Fig. 2.5. The idea is that I set the cavity length to be resonant with the measured pump frequency; this constrains the length to a discrete set of allowed lengths. For each such length I mark calculated cavity resonances near the simultaneously measured ODT frequency. This comparison suggests a pump longitudinal mode index[2] of 646.

Measurements of the frequencies of three simultaneously co-resonant lasers, two in adjacent longitudinal modes and several modes away (such as the pump and "reference" used in Sec. 2.5, plus the trap) would unambiguously identify the longitudinal mode index and cavity length as the measurement of two neighboring "pump" modes would constrain the cavity length while the comparison to the trap frequency would constrain the longitudinal mode index. We do not have a good measurement of the "reference" laser frequency in addition to the simultaneous pump and reference frequencies available to perform this analysis. When searching for co-resonance of the pump and reference lasers, we naïvely expected to find it when they were 600(1) GHz apart, but experimentally I found that I had to tune the reference laser closer to the pump frequency by 6(2) GHz to achieve co-resonance (implying $\nu_{\mathrm{FSR}} = 594(1)\,\mathrm{GHz}$); unfortunately, the precise frequency was not recorded correctly so we do not have a direct measurement with higher precision.

2.2.2 Atom–cavity elliptical birefringence

An empty, idealized optical cavity has degenerate circular polarization modes, or alternatively, degenerate linear polarization modes; the input light will populate a mode of identical

[2]By this I mean 646 half-wavelengths fit in the vacuum distance, not that this is the 646th mode. Due to the dispersive properties these do not generally correspond.

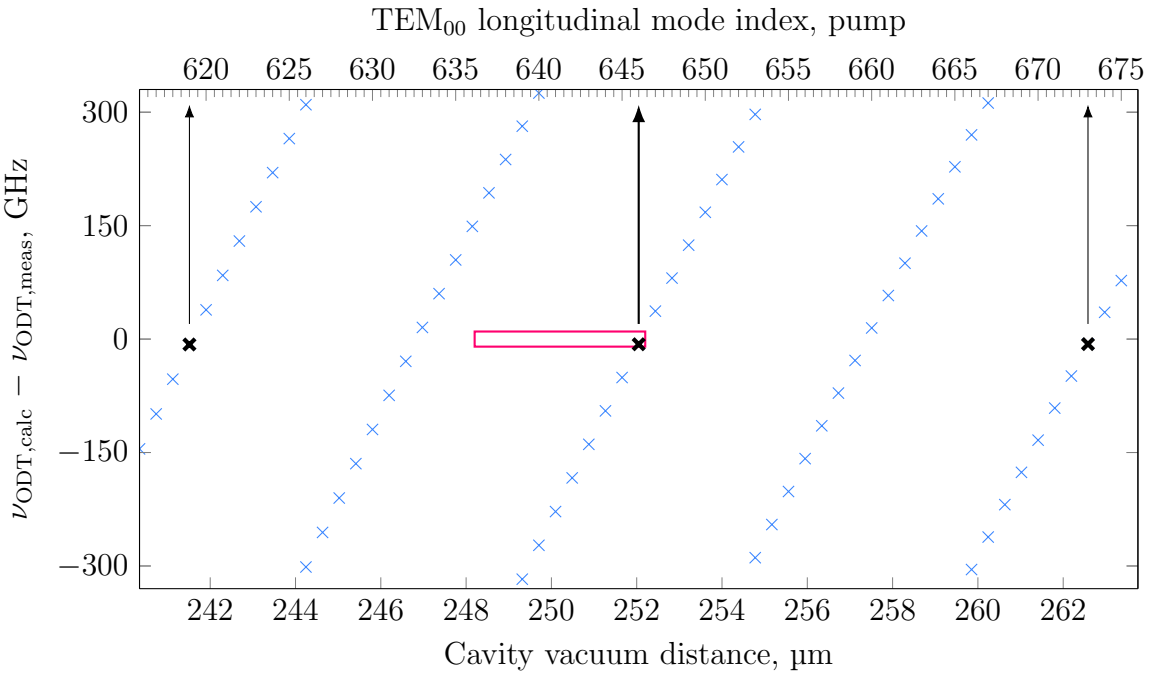


Figure 2.5: The frequency of co-resonant pump light and trap light were measured to be 384 185 GHz and 355 728 GHz, respectively. The inter-mirror distance L_c is constrained to integer multiples of half the pump vacuum wavelength 780.3336 nm. Co-resonant trap frequency TMM calculations $\nu_{\mathrm{ODT,calc}}$, assuming normal incidence, at these $\{L_c\}$ agree with the measured trap frequency $\nu_{\mathrm{ODT,meas}}$ for pump longitudinal mode indices $\{619, 646, 673\}$. The rectangle represents a prior estimate of the cavity length and the relative frequency uncertainty of the measurement and prediction, suggesting pump mode 646 and $L_c = 252.047\,\mu\mathrm{m}$.

polarization, and the output light will again have the same polarization. Linear birefringence in the cavity mirrors causes an energy splitting between two linearly polarized cavity modes, which also results in mixing between the circularly polarized cavity modes now that they are no longer eigenmodes. The circular birefringence of spin-polarized atoms in the cavity causes an energy splitting between the two circularly polarized cavity modes, mixing the linear modes. The combination of linear and circular birefringences has effects on the response of the cavity to a drive depending on the relative strengths of the birefringences.

We drive the cavity with nearly circularly polarized light and we use a polarization-sensitive detector that detects circularly polarized output light of the corresponding handedness. With atoms in the cavity but no linear birefringence, the cavity transmission spectrum exhibits a dispersive shift proportional to the collective spin state of the atoms. Linear birefringence blurs the relation between the dispersive shift and the spins, and the dispersive shift itself becomes less well-defined as the cavity response is no longer Lorentzian in shape.

Following the derivation in Ref. [73], we describe this system by the Hamiltonian

$$H = \hbar\omega_c \left(\hat{c}_+^\dagger \hat{c}_+ + \hat{c}_-^\dagger \hat{c}_-\right) + \hbar\Delta_m \left(\hat{c}_+^\dagger \hat{c}_+ - \hat{c}_-^\dagger \hat{c}_-\right) + \hbar\Delta_\mathrm{b} \left(\hat{c}_+^\dagger \hat{c}_- + \hat{c}_-^\dagger \hat{c}_+\right), \tag{2.2}$$

where ω_c is the "bare" cavity resonance frequency, Δ_b is the linear birefringence of the cavity mirrors, and Δ_m the circular birefringence of the atoms. I use the subscripts b and m to indicate birefringence and the total m_F of the atoms along the cavity direction respectively.

To investigate the effect of the birefringence on the dispersive shift measurement, we use the above Hamiltonian in combination with terms describing coherent driving $\eta_\pm$ to solve for the steady-state cavity occupation, assuming the modes all have identical amplitude decay rates κ. In a rotating frame detuned from ω_c by Δ,

$$\dot{\hat{c}}_+ = (-i(\Delta - \Delta_m) - \kappa)\hat{c}_+ + \sqrt{2\kappa}\eta_+ - i\Delta_\mathrm{b}\hat{c}_- \tag{2.3}$$

$$\dot{\hat{c}}_- = (-i(\Delta + \Delta_m) - \kappa)\hat{c}_- + \sqrt{2\kappa}\eta_- - i\Delta_\mathrm{b}\hat{c}_+ \tag{2.4}$$

The $\eta_\pm$ are external cavity drives of corresponding polarization such that on resonance with a bare cavity the steady-state photon number would be $n_\mathrm{max}^\pm = 2\langle|\eta_\pm|^2\rangle$. We assume a well-polarized drive so that $\eta_- = 0$.

$$\bar{n}_+ = \langle\hat{c}_+^\dagger \hat{c}_+\rangle = n_\mathrm{max}^+ \frac{\kappa^2[(\Delta + \Delta_m)^2 + \kappa^2]}{(\Delta^2 + \Delta_\mathrm{b}^2 + \Delta_m^2 + \kappa^2)^2 - 4\Delta^2(\Delta_\mathrm{b}^2 + \Delta_m^2)} \tag{2.5}$$

$$\bar{n}_- = \langle\hat{c}_-^\dagger \hat{c}_-\rangle = n_\mathrm{max}^+ \frac{\kappa^2\Delta_\mathrm{b}^2}{(\Delta^2 + \Delta_\mathrm{b}^2 + \Delta_m^2 + \kappa^2)^2 - 4\Delta^2(\Delta_\mathrm{b}^2 + \Delta_m^2)} \tag{2.6}$$

Note that the denominators of these expressions are the same. In principle, if one has access to both $\bar{n}_+$ and $\bar{n}_-$, taking the ratio of these two quantities would cancel the dependence of each on the complicated denominator:

$$\frac{\bar{n}_-}{\bar{n}_+} = \frac{\Delta_\mathrm{b}^2}{(\Delta + \Delta_m)^2 + \kappa^2}. \tag{2.7}$$

The power ratio is thus described by a Lorentzian function that peaks at $\Delta = -\Delta_m$ for any value of Δ_b.

In the experimental analysis historically performed in E3, we only measure a single circular polarization of the output light, as described in Eq. 2.5, as we sweep the pump light frequency across across cavity resonance. Although the data are fit well by a Lorentzian function, the analysis here indicates that these fits result in biased measured dispersive shifts that are not proportional to the true spin state of the atoms. I fit a Lorentzian function to the expression derived in Eq. 2.5 for various values of circular birefringence Δ_m and compare to it the extracted frequency $\tilde{\Delta}_m$ in Fig. 2.6. There is a systematic error between Δ_m and $\tilde{\Delta}_m$ that results in values of $\tilde{\Delta}_m$ biased away from zero compared to Δ_m, so that $|\tilde{\Delta}_m| > |\Delta_m|$. For small $\Delta_m/\kappa \ll 1$, the error has the heuristic dependence

$$\tilde{\Delta}_m - \Delta_m \simeq \left(\frac{3}{2}\frac{\Delta_\mathrm{b}}{\kappa}\right)^2 \Delta_m. \tag{2.8}$$

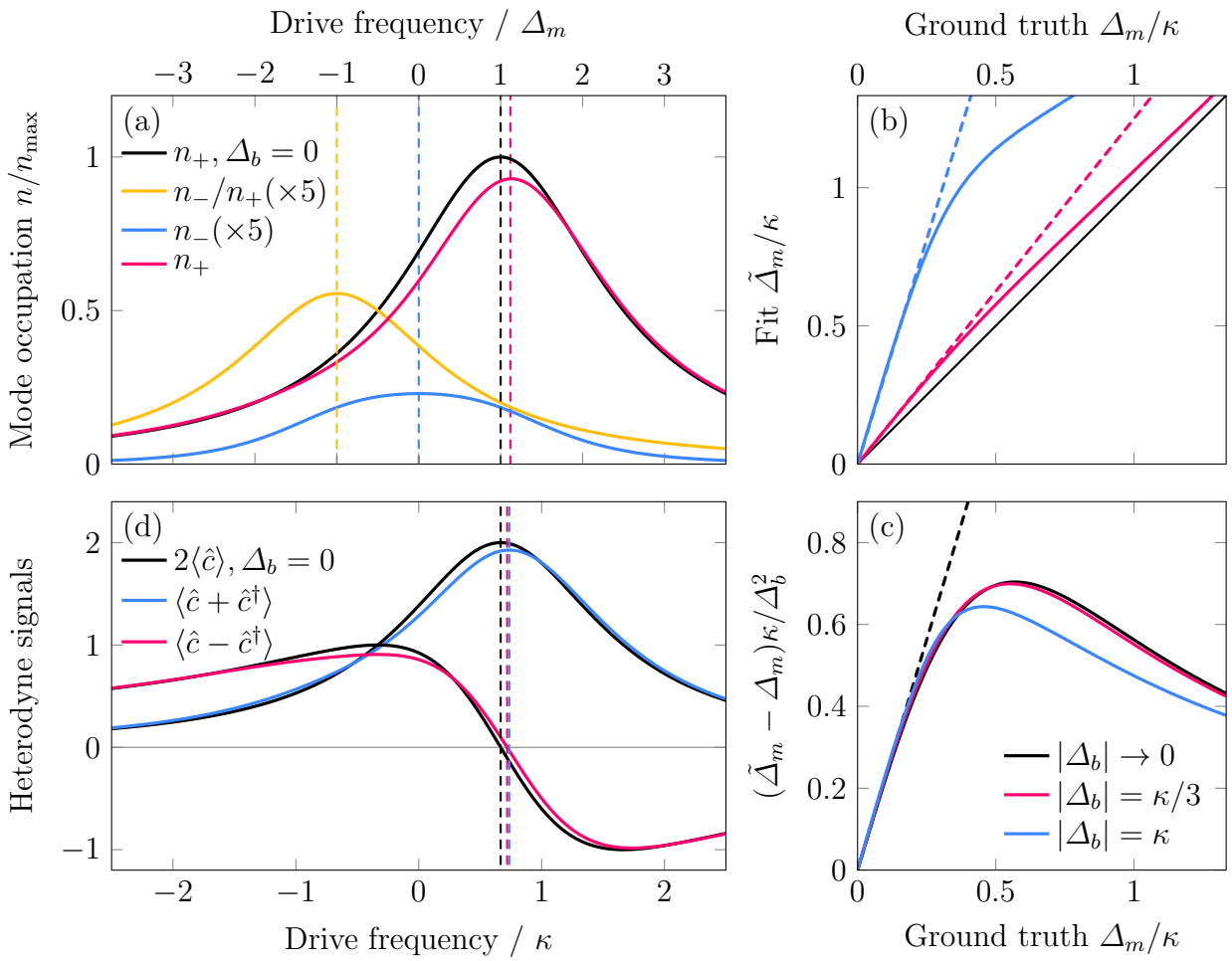


Figure 2.6: (a) Calculations of the steady-state cavity mode occupation for a circularly polarized input drive slowly swept across the resonance frequency of a cavity containing atoms spin-polarized along the cavity axis. The circular birefringence Δ_m of the atoms causes a splitting between circularly polarized cavity modes, chosen here to be $\Delta_m = 2\pi \times 1.2\,\mathrm{MHz}$. The linear birefringence of the cavity, previously measured to be $\Delta_\mathrm{b} = 2\pi \times 0.6\,\mathrm{MHz}$, causes the circularly polarized drive to populate both circularly polarized cavity modes. The ratio n_-/n_+ has a Lorentzian shape centered at the frequency $-\Delta_m$. (b) Comparison between the estimated dispersive shift $\tilde{\Delta}_m$ determined by a Lorentzian fit to n_+, and the true circular birefringence Δ_m. The dashed lines are plotted according to Eq. 2.8. The curves all have odd parity; only the positive half is shown. (c) The dispersive shift measurement bias $\tilde{\Delta}_m - \Delta_m$ scales as $(\Delta_\mathrm{b}/\kappa)^2$ for $\Delta_\mathrm{b}/\kappa \ll 1$. The dashed lines are plotted according to Eq. 2.8. The peak values of the curves are described in Eq. 2.9. The colors of curves in (b) and (c) correspond to the legend in (c). (d) The two quadratures of the heterodyne signal for the output polarization corresponding to the input polarization. The frequency axis of (d) is the same as that of (a).

For small linear birefringence $\Delta_\mathrm{b}/\kappa \ll 1$ the error has an approximate maximum value

$$|\tilde{\Delta}_m - \Delta_m| \lesssim \sqrt{2}\frac{\Delta_\mathrm{b}^2}{\kappa}. \tag{2.9}$$

I note two ways to mitigate this measurement bias phenomenon, of which one can in principle be performed retroactively on data already measured and implemented into analysis workflow without any change to the apparatus; the other depends on incorporating data from a second detector in the output path which could have been, but was not, present during measurements in E3.

The first is to generate a calibration function $\tilde{\Delta}_m(\Delta_m)$ as in Fig. 2.6(b). For a given cavity, Δ_b is fixed and can be measured; equipped with a reliable measurement of Δ_b one can calculate the curve mapping Δ_m to $\tilde{\Delta}_m$, invert it, and end up with a calibration curve that given a measured $\tilde{\Delta}_m$ maps to an inferred Δ_m. Given that we have a measurement [74] of Δ_b, it should be possible to perform this mapping retroactively on data collected in the past by splicing this calibration into the analysis pipeline. The disadvantages of this approach include distortions introduced by inaccuracy in measuring Δ_b, which lead to systematic error in the calibration curve. These corrected measurements will also have varying uncertainties inherent to the fact that the original $\tilde{\Delta}_m$ measurement has varying sensitivity across different ranges of Δ_m.

The second is to use two parallel polarization-selective detectors measuring the light emitted from the cavity, one measuring the circular polarization corresponding to that of the input light (like the single-polarization measurement performed in E3), and a second one measuring the opposite circular polarization. This could be done using a waveplate to change the circularly polarized output light into two linear polarizations, splitting them using a polarizing beam splitter, and directing the light exiting each port of the splitter onto one of the detectors. Another approach would be to use dynamic waveplates such as liquid-crystal variable waveplates (LCVWPs) to dynamically choose which output polarization reaches the detector, performing a sweep measuring one polarization and then immediately repeating the measurement after switching the state of the LCVWP. We integrated LCVWPs at both the input and output of the cavity, described in Ref. [7], but did not use them for this particular application. With measurements of both polarizations, one can take the ratio of the two powers and fit a Lorentzian to it; the frequency of the peak in that fit offers an unbiased measurement of $-\Delta_m$, as described in Eq. 2.7. Note that if the cavity drive is not a pure circular polarization, then the ratio will generally not be a Lorentzian function.

2.2.3 Science cavity piezo–chip temperature feedback

The science cavity lock eventually drifts to the end of the range of its integrator, at which point it loses lock and interrupts data collection. A possible improvement would still largely use feedback from the ODT to the cavity piezoelectric transducer, but now also feed the cavity piezo control signal through an extremely slow low-pass filter to the setpoint of the

chip temperature controller, which has effectively infinite cavity frequency actuation range. This idea was discussed, but we did not find an opportune time to implement it in E3.

2.3 Laser stabilization

2.3.1 Locking to spectroscopy

Near-resonant laser light is an essential tool for optically cooling and trapping clouds of atoms. The frequency of the light must be carefully controlled to interact with the atomic vapor; we typically need to control it down to the level of, or more finely than, the linewidth of the ^{87}Rb D_2 transition, $\Gamma \approx 6\,\mathrm{MHz}$. Thermal, electrical, and mechanical fluctuations of the laser can cause the frequency of its light to vary significantly, so we use feedback control to correct the fluctuations and stabilize the frequency. Stabilization of any experimental parameter requires a reference value to generate an error signal that the control system minimizes. The best and most straightforward frequency reference for light driving atomic transitions is the atoms themselves; since all atoms of a given element and isotope are fundamentally identical, we can use a Rb vapor cell as a frequency reference. We pick off some of the laser light and direct it through the vapor cell to probe the transition frequency of the atoms by measuring how much of the light the atoms absorb and generate the necessary error signal. So long as the vapor cell is not subject to strong electromagnetic fields, the primary challenge is the Doppler effect due to the thermal motion of the room-temperature atomic vapor, which causes broadening of the absorption of the vapor and would limit the precision of the stabilization. Pump-probe spectroscopy circumvents this by only probing atoms that are simultaneously co-resonant with two laser beams incident from opposite directions: atoms with zero velocity projection onto the beam propagation axis and thus no Doppler shift [75–78].

Standard pump-probe vapor cell spectroscopy techniques include saturated absorption spectroscopy (SAS), which has become standard in experimental AMO laboratories [79, 80], in which the probe light is modulated, but features problematic residual amplitude modulation (RAM); modulation transfer spectroscopy (MTS) [81], instead puts the modulation on the pump light and avoids the RAM issue (but often features a smaller error signal size). When I joined E3, both the repumper laser and the main cooling laser were stabilized using SAS, and in my time on the experiment we rebuilt first the repumper lock, and then the cooling laser lock, using MTS and found it advantageous. Detailed schematics of our spectroscopy configurations have been previously described [7].

2.3.2 Reference cavity

Not all of the lasers are locked to atomic spectroscopy as described above, because lasers that are far from atomic resonance cannot easily be locked using atomic spectroscopy. We still need control of the frequencies of these far-detuned lasers including the cavity pump,

typically red-detuned from the D_2 line by 30–40 GHz, and the ODT, red-detuned by about 30 THz. The exact frequencies at such large detunings are of little consequence to the atomic response, but because the experiment takes place in an optical cavity the various frequencies must be controlled on a scale better than $\kappa = 1.8$ MHz to maintain frequencies relative to the cavity resonance. This is accomplished using the "reference cavity" (as opposed to the "science cavity" which hosts the atoms used in the experiment), a Fabry–Pérot optical cavity located in a separate vacuum chamber.

We pick off a small amount of light from each of several lasers to be locked and direct it to the reference cavity, multiplexed using polarization, dichroic mirrors, and different modulation frequencies so that several lasers can be separately stabilized relative to the cavity simultaneously. Fiberized electro-optic modulators modulate the light to perform PDH-type locks to the reference cavity with known frequency offsets. We typically lock at least three external-cavity diode lasers (ECDLs) to the reference cavity this way: the science cavity pump, the ODT, and the repumper. Historically, the reference cavity length was stabilized to the frequency of the ODT light, which was in term stabilized by a signal from the Wavemeter monitoring its frequency, see Sec. 2.3.4. Early in my time in the group we changed this, so that now the reference cavity length is stabilized with respect to the repumper atomic spectroscopy error signal, by having the repumper follow the cavity while the cavity is locked such that the repumper is resonant with the spectroscopic signal. In our system, this new scheme offered more flexibility in tuning the various laser frequencies.

2.3.3 Lasers used in this experiment

Almost all of our lasers used in this work and in this experiment are grating-stabilized external-cavity diode lasers (ECDLs). We used a Newport Vortex as our repumper laser and several Toptica DL 100 and DL Pro model ECDLs.

Two additional lasers were introduced to the experiment for the photoassociation (PA) experiments: a Coherent 899 Ti:sapphire-converted ring laser (pumped by a Coherent Verdi V18 at 532 nm) and another ECDL. Of these two, the Ti:sapph laser was typically locked to the reference cavity while the new ECDL was beatnote-locked to the Ti:sapph to ensure its relative coherence. Experiments on the two-color heterodyne phase-lock described in 2.5 used the same additional ECDL as the PA experiments but did not use the Ti:sapph. In this case the additional ECDL was locked directly to the reference cavity in place of the Ti:sapph.

2.3.4 Wavemeter lock

Locking the various lasers to either spectroscopy or, by using the reference cavity, to each other, serves to stabilize their relative frequencies. It is often useful or necessary to monitor the absolute frequencies as well. We do this by picking off a small portion of light from each laser to direct towards a fiber switch that cycles through its inputs to feed one at a time into a HighFinesse Wavelength Meter WS7.

2.4 Optical readout

Information leaves the system, carried by photons leaving the cavity, and produces an electrical signal on an optical detector. A reconfigurable series of radio-frequency electronics gizmos then filter and further amplify the signal and feed it to a GageScope CSE1442 computer oscilloscope that ultimately records it into a digital record. We observe the signal and record data at a sample rate of 80 MHz.

2.4.1 Heterodyne detection

Information about the system under study is coupled to the rest of the world through light that enters and leaves the cavity through the mirrors. The atomic system and its dynamics couple to the intra-cavity field, change the complex transmission function of the cavity, and modulate the amplitude of phase of the transmitted light, which now holds a record of the atom-cavity dynamics. To measure this record, we interfere the transmitted light with a local oscillator beam and direct the combined beam onto a Newport 1807-FS balanced photodetector. The local oscillator is a 1 mW beam split from the cavity pump before the cavity, and offset in frequency by $\nu_{\text{het}} = 10\,\text{MHz}$. There is a particular experimental mode described in Sec. 2.5 where we instead used $\nu_{\text{het}} = 19\,\text{MHz}$. In all cases, this is well below the Nyquist frequency ν_{N} of the 80 MHz sampling rate, $\nu_{\text{het}} < \nu_{\text{N}} = 80\,\text{MHz}/2$.

In principle, the frequency offset ν_{het} could be effected on the local oscillator, which would provide certain advantages; for historical reasons in E3 the frequency offset is applied to the light driving the cavity with a pair of AOMs, with the same result but extra inconvenience[3].

The frequency offset ν_{het} makes this an optical heterodyne measurement, capable of measuring both quadratures of the transmitted light. Without the frequency offset, the system would realize an optical homodyne measurement, which would record one quadrature of the emitted light as selected by the phase difference between the combined beams. We do heterodyne measurement because of the flexibility of simultaneously measuring both quadratures, but also because of a slow phase instability in the interferometer that would render homodyne measurement impractical. The disadvantage is that when a particular quadrature is of interest, heterodyne measurement is 50% less efficient than a comparable stable homodyne measurement would be. This can be understood as the detector spending half of its time measuring each quadrature rather than all of the time measuring just one quadrature. Another way to think of this is to consider sending the cavity light through a 50:50 beamsplitter, interfering the beam in each arm with a homodyne local oscillator, and directing the two beams to separate photodetectors. Then one can choose the phases of the two local oscillators so that one arm measures the in-phase component and the other measures the quadrature component. In this picture, the unused input port of the beamsplitter couples

[3] In our configuration, changing ν_{het} necessitates changing the laser frequency or the cavity frequency to maintain resonance; more tediously, changing ν_{het} also necessitates realigning the cavity pump light to the cavity mode to maintain coupling, because the AOMs are in a single-pass configuration.

vacuum noise into the two arms. It turns out that this results in the same 50 % reduction in measurement strength that one finds in heterodyne.

The detection efficiency is $\epsilon_{\mathrm{det}} = \epsilon_{\mathrm{cav}} \times \epsilon_{\mathrm{path}} \times \epsilon_{\mathrm{mm}} \times \epsilon_Q$; here ϵ_{cav} is the cavity output efficiency, ϵ_{path} is the efficiency of the path from the cavity to the detector, ϵ_{mm} is the efficiency of the optical mode matching between the cavity transmission and the local oscillator beams, and ϵ_Q is the quantum efficiency of the photodetectors. Depending on the context, one may also introduce an additional factor of 1/2 to account for heterodyne detection. Over time, the detection efficiency would degrade. When this degradation had accumulated to a significant point, we would generally find that we could mostly recover it by optimizing the beam path to recover ϵ_{path} and ϵ_{mm}, of which the latter was usually the one that degraded first and could be most corrected, unless some optic had been smudged reducing ϵ_{path}. In my time with E3, we observed typical detection efficiencies around $1 - 5\,\%$.

The heterodyne signal we measure generically contains a carrier peak at the offset frequency ν_{het} (either 10 MHz or 19 MHz), first-order sidebands at $\nu_{\mathrm{het}} \pm \nu_{\mathrm{m}}$ containing information about the amplitude and phase of cavity modulation at frequency ν_{m}, and sometimes higher-order sidebands. In this work the modulation is Larmor precession at $\nu_{\mathrm{m}} = \omega_{\mathrm{s}}/2\pi$ which varies in the range of several hundred kHz.

2.4.2 Single-photon detection

While heterodyne detection offers a complete picture of the cavity output mode, its efficiency can be limited by imperfect mode-matching and its bandwidth limited by the available heterodyne frequency ν_{het}, in turn limited by the detector bandwidth and the measurement sampling rate. For some experiments we used a single-photon avalanche detector (SPAD) module, also known as a single-photon counting module (SPCM), to detect the cavity output. In particular these were experiments searching for super-radiance on the molecular transition, described in Sec. 5.5, and also measurements of the cavity lifetime. We used a Laser Components Count® series fiber-coupled SPCM with quantum efficiency $\gtrsim 50\,\%$. The cavity output at 780 nm wavelength reflects from the dichroic mirror that separates it from the ODT, was coupled into a fiber. We installed a sufficiently stable flip mirror such that when it is flipped out of the path the light travels to the heterodyne detector and when it is flipped into the path the light is redirected to the fiber. To minimize background counts, we thoroughly wrapped the fiber with opaque black tape.

2.4.3 Optical imaging

Much of the data collected in E3 is in the form of the real-time measurement record of light emitted from the cavity, usually observed with a heterodyne detector and sometimes with a single-photon detector, but the system additionally captures optical absorption images of the atomic cloud in the cavity at the conclusion of each experimental cycle. In diagnostic conditions, the absorption image can be captured earlier in the experimental cycle, such as when the atoms have not yet reached the cavity. Absorption images are often used

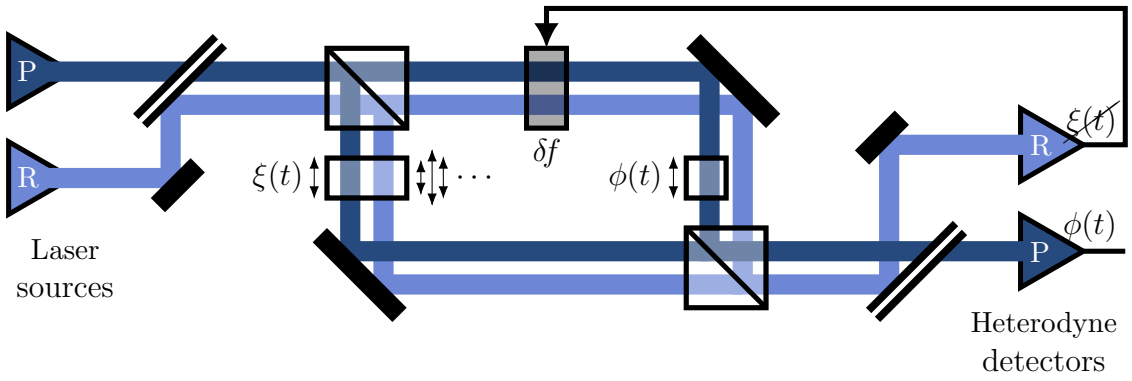


Figure 2.7: Model of the two-color Mach-Zehnder heterodyne interferometer system. A single laser P is used to measure $\phi(t)$, but measurements are obscured by unknown and variable $\xi(t)$. A second laser source R and heterodyne detector are incorporated that do not measure, and are thus insensitive to, $\phi(t)$. The phase from detector R is fed back to the heterodyne frequency offset ν_{het} to zero $\xi(t)$, allowing laser P to measure $\phi(t)$. In our system, $\phi(t)$ represents the differential phase of the cavity transmission as shifted by the atom-dependent dispersive shift, to which P is sensitive but R is not. In this model, the two beams are shown spatially offset to visualize that only one beam probes $\phi(t)$; in reality the beams co-propagate and the selective sensitivity to $\phi(t)$ is due to vastly different detuning from atomic resonance ($\sim -30\,\text{GHz}$ versus $-625\,\text{GHz}$). The phase noise $\xi(t)$ is common to both P and R.

for diagnostic purposes and thermometry and serve as a less-sensitive check on the cavity-dispersive-shift atom-number measurement. An example absorption image is shown in Fig. 2.2.

2.5 Homodyne and heterodyne measurement rates

2.5.1 Motivation: atom counting and path length noise

Information from the atom-cavity system is encoded in both the magnitude and phase of the light that leaks out from the cavity. As described in Sec. 2.4.1, heterodyne detection is in principle capable of measuring that information in both the magnitude and phase of the light. However, experiments conducted in E3 have been limited by phase instability between the cavity light and the local oscillator light on time scales greater than $\sim$1 ms. We attribute this to differential fluctuations $\xi(t)$ in the optical path lengths between the two interferometer paths, possibly due to vibrations of the apparatus or in the optics mounts. Homodyne measurement requires, in the absence of an unknown phase shift from the cavity–atom system, a predictable relative phase between the two arms of the interferometer, the signal and the local oscillator. In our case, the consequence of the phase instability is

that it has been impossible to perform stable homodyne measurements with our system on timescales longer than a few hundred µs.

To mitigate this phenomenon, one could rapidly modulate the frequency of the cavity drive light and detect phase modulation on the transmitted light from scanning across the cavity lineshape to measure the derivative of the phase and identify the detuning of the light from cavity resonance. This would however carry the deleterious effect of changing the spectrum of the light driving the cavity and thus the spectrum of the light populating the cavity and would change the atom-cavity interaction under study. Therefore, I sought to mitigate the phase instability without significantly modifying the cavity drive.

I was motivated by the recent work performed with E3 in which the dispersive shift was measured to monitor the atom number in the cavity in Ref. [56], and in Ref. [7] where it was used in a classical feedback system to prepare the system with less variation in the atom number from one experimental shot to the next. I wondered what it would take to improve our measurement sensitivity to the point that we could distinguish N_a from $N_\mathrm{a} \pm 1$ atoms [82] during a real-time atom number counting measurement, and whether we could use this with classical feedback to prepare clouds of deterministic atom number. It turns out that the maximum measurement rate we could hope to achieve over long periods of time without phase stability (called $\Gamma_m^M/2$ in the next section) is too small to achieve this level of precision, but that the measurement rate for phase-stable quadrature-component homodyne measurements (Γ_m^Q) may have a chance at doing so. This realization got me hooked on trying to solve the phase instability, and the remainder of this section describes the solution I devised and its implementation. In understanding these concepts and in figuring out some details of the signal processing chain, I benefited greatly from the kind help of Dr. Will Livingston.

2.5.2 Dispersive measurement rates

The dispersive interaction means that photons leaving the cavity carry information about the state of the atoms within. The scattering matrix element describing the transmission through an imbalanced cavity is

$$S_{21}(\Delta) = \frac{\sqrt{\kappa_1 \kappa_2}}{\kappa_1 + \kappa_2 + \imath\Delta}, \tag{2.10}$$

for a laser drive at detuning Δ from the dispersively shifted cavity resonance, incident on a mirror with leakage rate κ_1 and transmitting through the other mirror with leakage κ_2. Our cavity is quite imbalanced: we drive through the less-transmissive mirror and detect photons from the more-transmissive mirror. To an approximation we can assume that $\kappa_2 \gg \kappa_1$ and all photons leave through the second mirror:

$$t(\Delta) \approx \frac{\kappa}{\kappa + \imath\Delta} \tag{2.11}$$

Imagine two possible states of the atomic cloud labeled $|\beta_1\rangle$ and $|\beta_2\rangle$ that correspond to cavity shifts Δ_1 and Δ_2, respectively. These states could represent for example different atom

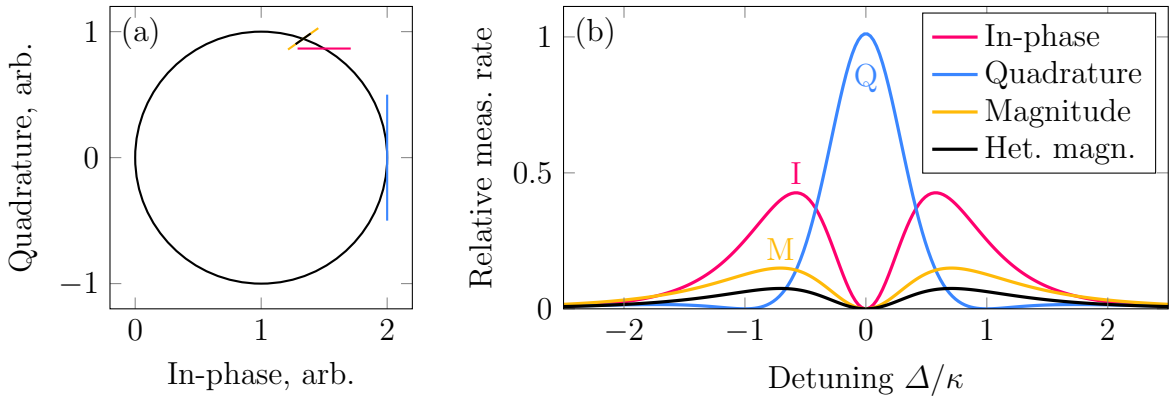


Figure 2.8: Complex cavity transmission signal and measurement rates. (a) The complex cavity transmission function $t(\Delta)$. The point $\Delta = 0$ corresponds to the largest $|t|$ and lies along the horizontal axis. The lines correspond to the measurement cases in (b), indicating where on the transmission function the measurement rate is maximized (shown for $\Delta > 0$). The lengths of the lines are proportional to the peak relative measurement rates. (b) Relative measurement rates for detection of the light output from a cavity. Several cases are shown: homodyne measurement of the in-phase component, the quadrature component, or on a linear combination that corresponds near a particular detuning to the magnitude, of the signal. The case of measurement of the magnitude of the heterodyne signal, which corresponds to the form of measurement used in Ref. [56], is shown in black.

numbers or different spin configurations. Consider a system in either a pure superposition of these two states or a mixed state (classical uncertainty) of the two. Assume the cavity of bare frequency ω_c is driven by a laser with frequency near $\omega_c + \Delta_1$, $\omega_c + \Delta_2$, or $\omega_c + (\Delta_1 + \Delta_2)/2$. Photons transmitted through the cavity each carry an amount of information that serve to partially distinguish states $|\beta_1\rangle$ and $|\beta_2\rangle$. The degree to which a photon can serve to distinguish the states depends on the ratio of the state-dependent dispersive shift difference to the cavity linewidth $|\Delta_{12}|/\kappa$ where $\Delta_{12} \equiv \Delta_1 - \Delta_2$. If the differential dispersive shift is large compared to the cavity linewidth $|\Delta_{12}| \gtrsim \kappa$, then if a given laser frequency is resonant for the dispersive shift of one state then it will not be resonant with the other, and it will not take many detected photons to reliably distinguish the two states.

On the other hand, if the differential dispersive shift is small $|\Delta_{12}| \ll \kappa$, then each photon carries little information distinguishing the two states. If the driving laser is near the cavity resonance then a small dispersive shift would not affect the in-phase component of transmission much, while it would mostly affect the quadrature component.

Under a constant classical drive at detuning Δ, the state $|\beta_1\rangle$ ($|\beta_2\rangle$) corresponds to a coherent state α_1 (α_2) in the cavity determined by the drive strength and the transmission function Eq. (2.11). For small differential dispersive shift, these coherent states will have significant overlap, and to reliably distinguish them requires observation for some period of

time. The distinguishability of the states (how much information is carried per photon) and the photon detection rate together determine the measurement rate Γ_m, which altogether depends on the cavity decay rate, the laser detuning, the photon detection efficiency, and the distinguishability along the measurement axis of choice as [83]

$$\Gamma_m \approx 2\kappa\bar{n}\epsilon|\delta\alpha|^2 \equiv \Gamma_0|\delta\alpha|^2, \tag{2.12}$$

where $\Gamma_0 = 2\kappa\bar{n}\epsilon$. Here $\bar{n}$ is the average intracavity photon number, ϵ is the cavity photon detection efficiency, and $\delta\alpha = \alpha_1 - \alpha_2$ represents the difference between the coherent states corresponding to the two states β_1 and β_2. Consistent measurement then eventually distinguishes the two states on a timescale $\sim 1/\Gamma_m$. For small differential dispersive shift Δ_{12} we can rewrite the coherent-state difference as $\delta\alpha = (d\alpha/d\Delta) \times \Delta_{12}$.

For measurement of the in-phase component we find

$$\begin{aligned}\Gamma_m^I &\approx \Gamma_0 \frac{4\Delta_{12}^2\Delta^2\kappa^4}{(\Delta^2+\kappa^2)^4} \\ &= \Gamma_0 \frac{27\Delta_{12}^2}{64\kappa^2},\end{aligned} \tag{2.13}$$

at the optimal detuning $|\Delta_{\text{opt}}^I| = \kappa/\sqrt{3}$, while for the quadrature component

$$\begin{aligned}\Gamma_m^Q &\approx \Gamma_0 \frac{\Delta_{12}^2\kappa^2(\Delta^2-\kappa^2)^2}{(\Delta^2+\kappa^2)^4} \\ &= \Gamma_0 \frac{\Delta_{12}^2}{\kappa^2}\end{aligned} \tag{2.14}$$

at the optimal detuning $|\Delta_{\text{opt}}^Q| = 0$. For an intermediate-phase homodyne measurement corresponding to the local magnitude direction at a given detuning,

$$\begin{aligned}\Gamma_m^M &\approx \Gamma_0 \frac{\Delta_{12}^2\kappa^2\Delta^2}{(\Delta^2+\kappa^2)^3} \\ &= \Gamma_0 \frac{4\Delta_{12}^2}{27\kappa^2}\end{aligned} \tag{2.15}$$

at the optimal detuning $|\Delta_{\text{opt}}^M| = \kappa/\sqrt{2}$. If one instead performs a heterodyne measurement of the magnitude the efficiency is worse than that by a factor of two as is typical for heterodyne measurements of single components.

In summary, the optimal-detuning measurement rates are $\Gamma_m = \Gamma_0 \times \{27/64, 1, 4/27, 2/27\}$ for in-phase, quadrature, magnitude, and heterodyne magnitude measurements, respectively. Switching from measuring the magnitude of the heterodyne signal to a quadrature-component homodyne (heterodyne) measurement would thus offer a possible improvement in the maximum rate at which two states β_1 and β_2 can be distinguished of 13.5× (6.75×).

In Ref. [56], experiments conducted with $\bar{n} = 6$ and $g_c \approx 2\pi \times 4\,\text{kHz}$ realized a measurement with a precision of $\Delta N_a \sim 10$ at an integration time around 1 ms. Repeating

this measurement with the same $\bar{n}$, g_c, and photon detection efficiency but assuming homodyne measurement of the quadrature component, we would anticipate improved precision of roughly $\Delta N_a \sim 3$.

Now I will use our system parameters to calculate how fast one could hope to distinguish two states β_1 with N_a atoms and β_2 with N_a+1 atoms in our system. I will assume[4] that the difference in the dispersive shifts is $\Delta_{12} = g_c = g_0^2/\Delta_{ca} = 2\pi \times 4\,\mathrm{kHz}$ for the detuning used in Ref. [56]. For our system parameters ($\kappa = 2\pi \times 1.82\,\mathrm{MHz}$, $\bar{n} \sim 6$, $\epsilon \sim 0.1$), $\frac{1}{2}\Gamma_m^M \approx 5\,\mathrm{s}^{-1}$ while $\Gamma_m^Q \approx 66\,\mathrm{s}^{-1}$. If we set $|\Delta_{ca}| \to 2\pi \times 10\,\mathrm{GHz}$, still far into the dispersive limit, we have $\Delta_{12} = g_c = 2\pi \times 17\,\mathrm{kHz}$. This would realize measurement rates $\Gamma_m^Q \approx 1200\,\mathrm{s}^{-1}$ and $\frac{1}{2}\Gamma_m^M \approx 88\,\mathrm{s}^{-1}$. Thus by using $\bar{n} = 6$ and a moderately larger dispersive coupling strength we could hope to achieve single-atom precision with an integration time $\sim 1\,\mathrm{ms}$. If the atom loss dynamics are sufficiently slow that on average fewer than one atom is lost in this 1 ms window, we may observe a quantized signal.

Off-resonant atomic scattering heats the cloud and leads to atom loss. These scattering events occur at rate $\Gamma_{sc} \sim \bar{n}\Gamma_e g_0^2/\Delta_{ca}^2$ per atom, or $\sim N_a \bar{n}\Gamma_e g_0^2/\Delta_{ca}^2$ for the whole cloud. I will not describe in detail the process of atom loss due to heating, but the essential point is that the trap is conservative with a finite depth and atoms remain trapped because they lack the energy to overcome the potential barrier, but as they gain more kinetic energy from scattering they will start to overcome the barrier and leave the trap. Importantly, note the same scaling $\propto \bar{n}/\Delta_{ca}^2$ of both Γ_{sc} and Γ_m. This offers a hint that if one wants to measure with higher precision, increasing $\bar{n}$ or decreasing Δ_{ca}^2 increases the measurement rate but also increases the atom heating and loss rates and that eventually there may be a limit where measuring faster is balanced by losing atoms faster and that the relative atom uncertainty will not improve once heating is the dominant source of atom loss. It is for this reason that being efficient with the information leaving the system is critical if one wants to improve measurement precision.

2.5.3 Adaptive optics: two-color path-phase-stabilization lock

A solution to the phase instability is illustrated schematically in Fig. 2.7. The cavity transmission exhibits a dispersive shift that depends on the number and state of atoms within the cavity, as well as the strength of the cavity–atom coupling g_0 and the detuning $\Delta_{pa} = \omega_p - \omega_a$ of the cavity pump laser from the atoms. Critically, the cavity supports multiple non-degenerate optical modes: resonance is achieved for modes with various longitudinal and transverse structures and polarizations. The "adjacent" resonant longitudinal modes are separated, approximately, by integer multiples of the free-spectral range $\nu_{FSR} = 593.2(10)\,\mathrm{GHz}$ as determined in Sec. 2.2.1. If the cavity is driven with "pump" light detuned by $\Delta_{pa} \sim -30\,\mathrm{GHz}$ and simultaneously with "reference" light detuned to $\Delta'_{pa} = \Delta_{pa} - \nu_{FSR} \sim -623\,\mathrm{GHz}$, the dispersive shift measured by the pump is greater by a

[4]The scalar dispersive shift per atom is 2/3 of g_c, while the vector dispersive shift is $g_c \times f/6$. For spin-polarized atoms we can treat the total as g_c. See Sec. 3.2.1 for more detail.

factor $\chi \equiv \Delta'_{\rm pa}/\Delta_{\rm pa} \approx 20 \gg 1$ than that measured by the reference[5]. The reference light is nearly insensitive to the atoms and probes a nearly bare cavity, so the phase of its heterodyne signal samples essentially only the bare cavity transmission phase plus the phase due to the variable interferometer path length drift $\xi(t)$.

There has been prior work exploring two-color interferometry including much effort to correct for fluctuations of the apparent path length of an interferometer due to variation in the index of refraction of air [84–86]. The setup discussed here is different in that rather than using two colors to sample the dispersion of the air, I use the two colors to separate the geometric path length fluctuations and the fluctuations due to air effects, both nearly common-mode for the two colors, from the variation of the cavity transmission phase. As the cavity dispersive shift evolves due to atomic dynamics, the cavity transmission phase seen by the far-detuned laser remains almost unchanged compared to that seen by the nearer-detuned laser. Additionally unlike those cases, because we are not interested in the total geometric distance, we need not know anything about the temperature or density or composition of the air, the absolute optical path length sampled by either laser, or the dispersion of the air; we only need to identify the phase fluctuations that are correlated among both lasers and those that are not. If we wanted to simply subtract the phases measured by the two lasers then there would be some constants of proportionality due to dispersion of the air. But since we simply freeze the optical path length of the reference laser and cancel its future fluctuation away from this value, the constants of proportionality do not play any role so long as the dispersion properties of the air remain constant (changes in the density of the air do not play a role, but changes in the dispersion of the air would change the relation between the apparent geometric path lengths at the two wavelengths, but this should be a very small effect under laboratory conditions).

[5]This ratio can be increased by choosing increasingly distant longitudinal modes up to several $\nu_{\rm FSR}$ away before the cavity parameters change significantly with frequency, and by decreasing $\Delta_{\rm pa}$. More generally, $\chi = (m\,\nu_{\rm FSR} + \Delta_{\rm pa})/\Delta_{\rm pa} = 1 + m\,\nu_{\rm FSR}/\Delta_{\rm pa}$ for integers m not too large.

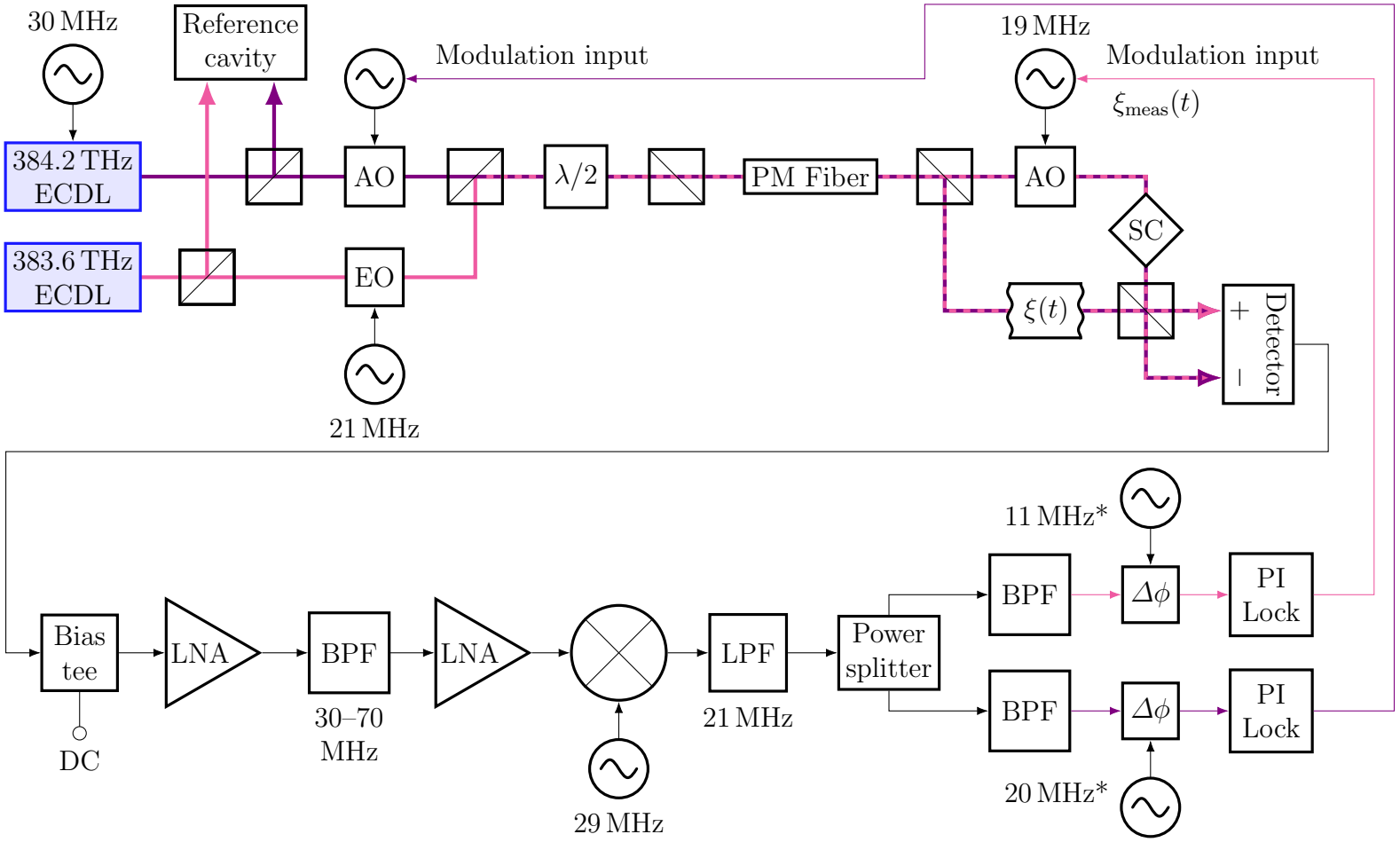


Figure 2.9: Two-color phase stabilization schematic. The 383.6 THz laser is used to cancel the common-mode noise $\xi(t)$, allowing the 384.2 THz laser to measure the cavity more sensitively. All function generators share a common clock. ECDL: external-cavity diode laser; AO: acousto-optic modulator; EO: electro-optic modulator; $\lambda/2$: half-wave plate; SC: "science" optical cavity; LNA: low-noise amplifier; BPF: band-pass filter; LPF: low-pass filter; $\Delta\phi$: phase detector; PI: proportional-integral. $\xi(t)$ is the differential phase noise between the interferometer arms, common-mode to both lasers. Inputs to the laser and EO effect modulation, while the AOs produce shifts. Frequencies of fillters characterize their passband or rolloff frequencies. *This indicates the generator frequency and also the center frequency of the BPF.

If there is a way to close a phase-locked loop with this measurement of $\xi(t)$, then the reference interferometer phase can be zeroed. We accomplish this by feeding the reference phase measurement back to the AOM providing the heterodyne offset frequency ν_{het} using an analog PI controller of the open-source JQI AMO design [87]. Because the twin interferometers share a balanced detector[6] in our setup, we separate the rf signals after detection and amplification. The reference signal is then filtered, fed into a Valon 4002 Phase Detector Module to be compared with an rf local oscillator, filtered again, and the resulting signal is finally fed into the modulation input port of the Agilent 33250A generator, closing the phase-locked loop. The pump signal can then be measured, or even used for feedback to the pump laser AOM to keep the pump laser resonant with the cavity as the cavity–atom dispersive shift evolves.

The results are shown in Figs. 2.11 and 2.12. Measurements of the pump heterodyne signal with the reference phase-locked loop engaged demonstrate what we get for all the trouble: having done no feedback on the pump signal itself, we have greatly reduced its phase instability and enabled stable phase-sensitive homodyne measurements over long measurement durations!

I began to integrate this improved system into the experimental sequence to sensitively monitor the atom number dynamics while atoms slowly leave the trap. My hope was to be able to resolve a quantized atom number signal and, by feeding this back to the forced evaporation, prepare clouds of deterministic atom number. Unfortunately, experimental setbacks interrupted this process and we did not have the chance to fully integrate the system.

[6]Note that this means that the shot noise floor is worse than the case of a single-color heterodyne detection because each signal has shot noise not just from its own LO power but from the total LO power, roughly double. If one were to use an etalon engineered and tuned to be highly reflective to one of the laser frequencies but highly transmissive to the other, then we could do dual heterodyne detection with two separate balanced detectors and avoid the additional noise from using a shared detector.

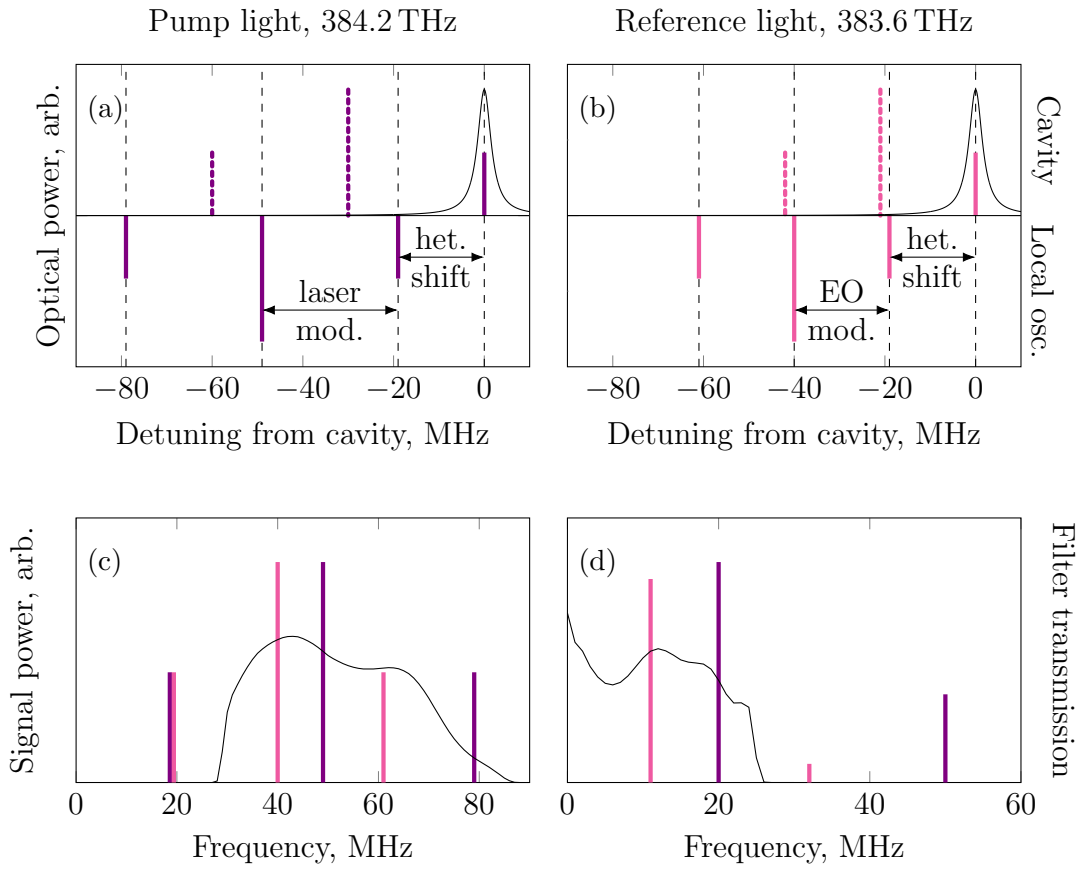


Figure 2.10: Schematic representations of the various signal frequencies generated in the two-color stabilization configuration and how they are reduced and separated. (a) Optical "pump" spectrum relative to the cavity resonance near 384.2 THz. (b) Optical "reference" spectrum relative to the cavity resonance near 383.6 THz. In (a) and (b), the spectrum of the light incident on the cavity is shown above the horizontal axis, with dotted lines representing components that are reflected from the cavity; the spectrum of the local oscillator light that does not encounter the cavity is shown mirrored below the horizontal axis. (c) Spectrum of electrical signals output from the balanced photodetector. The black line represents the transmission of the intermediate band-pass filter labeled 30–70 MHz in Fig. 2.9, which is used to suppress the component at $\nu_{\text{het}} = 19\,\text{MHz}$. (d) Spectrum of electrical signals following the mixer. The black line represents the transmission of the filter labeled LPF in Fig. 2.9. The signals at 11 and 20 MHz are the only ones not strongly suppressed. They contain the phase shifts sampled by the reference and pump lasers, respectively.

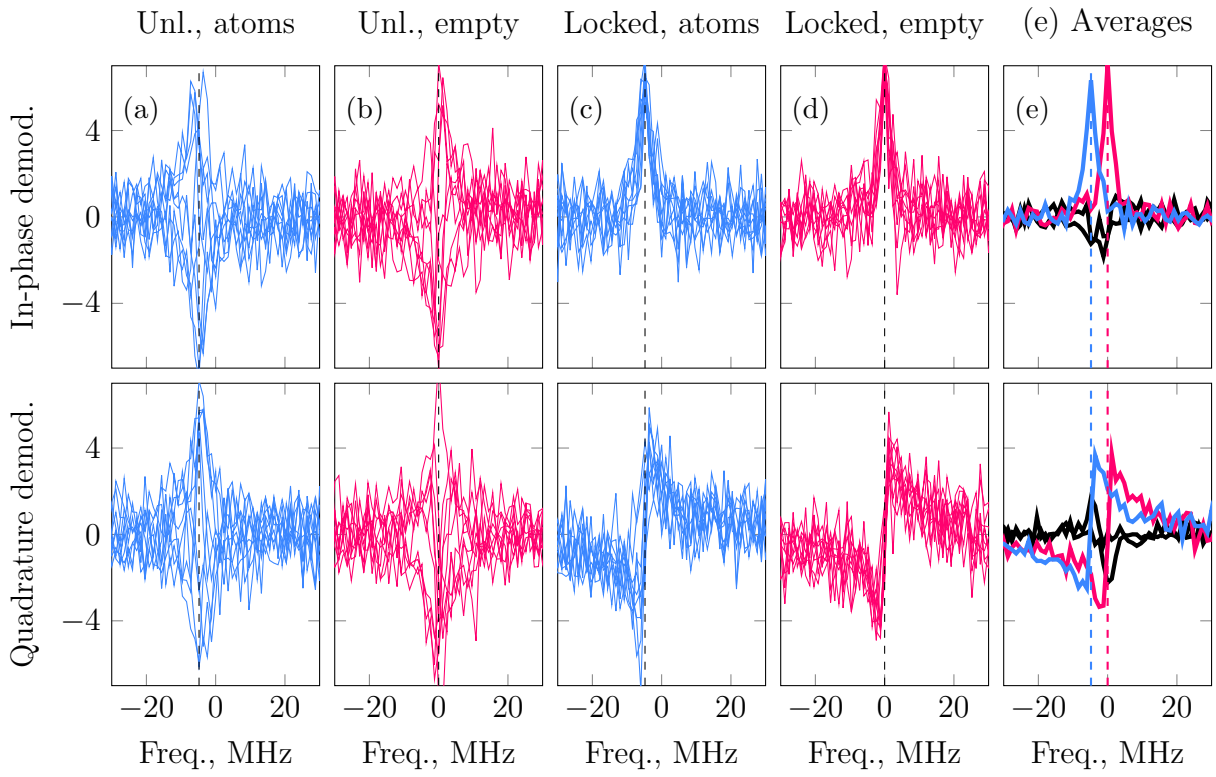


Figure 2.11: Demodulated heterodyne signals of pump frequency sweeps across cavity resonance with reference phase either (a,b) unlocked or (c,d) locked. (a), (c) Sweeps while ~ 1500 atoms are trapped within the cavity. (b), (d) Sweeps after the atoms have been ejected and the cavity is empty. Five individual traces are plotted in each subfigure, comprising ten sweeps across resonance. (e) The averages of several traces. Black lines are the averages of the free-running sweeps of (a,b) and the colorful lines are the averages of the phase-locked sweeps of (c,d). In the upper row are the in-phase demodulated signals and in the lower row are the quadrature demodulated signals. The cavity drive strengths produced an average photon number $\bar{n} \sim 4$ on resonance, split roughly evenly between photons at the pump and reference laser frequencies.

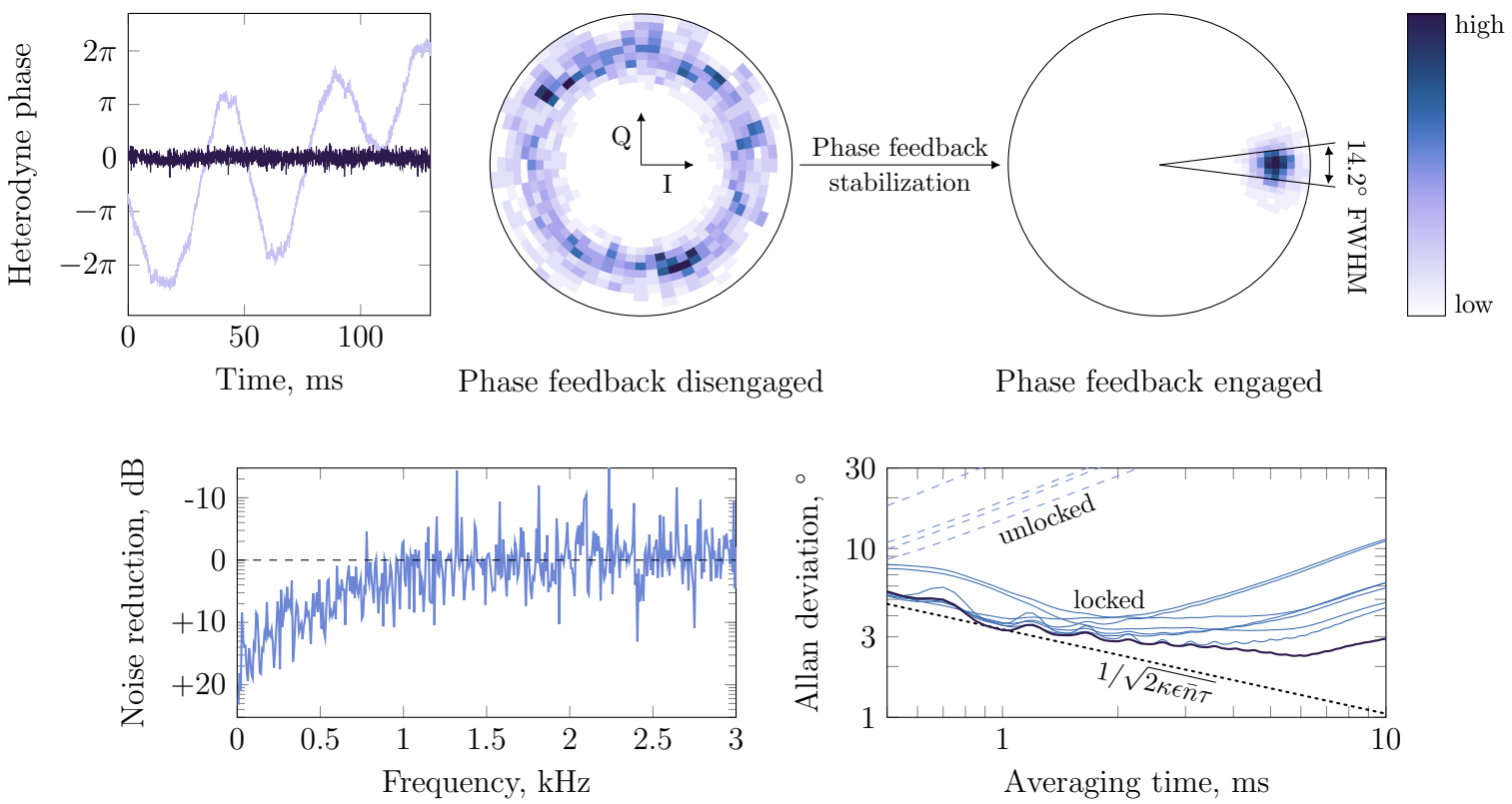


Figure 2.12: Individual traces of the heterodyne signal for a driven, empty cavity. Each heatmap visualizes the signal during one 140 ms experimental repetition, with the radius and angle corresponding to the heterodyne signal magnitude and phase respectively. The signals have been filtered to a bandwidth of 500 Hz. The intracavity photon numbers were approximately $3.6 - 4.2$, split roughly evenly between photons at the pump frequency and those at the next-lower-frequency longitudinal mode, with roughly equal local oscillator powers. The phase feedback was either disengaged or engaged, as indicated.

2.6 The slow, then fast, end of E3

Experiments end [88]. In the case of E3, the lore held that the experiment was to be likely decommissioned during Sydney Schreppler's PhD but the fruitful nature of the accessible science staved off the end long enough for Jonathan to join; again, he would likely see the end of the experiment but for a series of junior graduate students joining: Justin and Emma, and later Julian. Once again, Julian figured he would be the last student on E3, with the apparatus starting to demand increasing maintenance and repair, and then I joined the team. It was during my time as a graduate student that the experiment finally came to an end.

2.6.1 The slow end of E3

In 2020, the rubidium dispensers in the vacuum chamber ran dry. The chamber was opened and reassembled with first one new source, then another when it did not work, and rebuilt in early 2021; the bake and reassembly were the first things I worked on in E3 after joining in early 2021. Over the course of 2021 and 2022, we were able to record data on two primary scientific projects—studying spin optodynamics feedback and cavity photoassociation—and explore a number of side projects. By late 2022, we observed that the background pressure as measured by the ion pump current was rising gradually. Shortly thereafter was the academic labor union strike from Nov. 14, 2022 until Dec. 23, 2022; by the time we were back in the lab and getting everything up and running again the inferred pressure had worsened further. We noticed significant effects on the experiment: we were unable to load atoms into the cavity. It took a long time to rule out other causes and convince ourselves that it was actually due to the background pressure, but there-and-back magnetic transport measurements, careful measurements of the atom lifetime in a stationary magnetic trap, and MOT measurements, combined with steadily climbing ion pump current readings, made a strong case.

It seemed that we were unable to load atoms into the cavity because they were almost all lost due to collisions with background gas emptying the magnetic trap during the relatively long transport period. We explored performing the magnetic transport over a shorter period of time, but found that the heating and associated atom loss were disadvantageous. Eventually we decided to directly address the pressure issue, but because it was determined not worthwhile to properly bake the system again, our remaining options were to reduce the rubidium pressure and to fire the Ti sublimation pump. Partially closing the valve connecting the main chamber to the chamber holding the rubidium ampoule reduced its pressure but did not result in better performance. We fired the Ti sublimation pump with the chamber at room temperature, with the out-gassing was handled by the ion pump, the non-evaporable getter, and the fresh titanium surface; no turbomolecular pump was on the system, as we would have had to connect one and bake at least the connection chamber. The result was a decrease in the chamber base pressure after the out-gassing settled—unfortunately it did not last, and the chamber pressure began to climb again. We fiddled with this process numerous times while searching for any other workarounds and while gradually weighing the call to

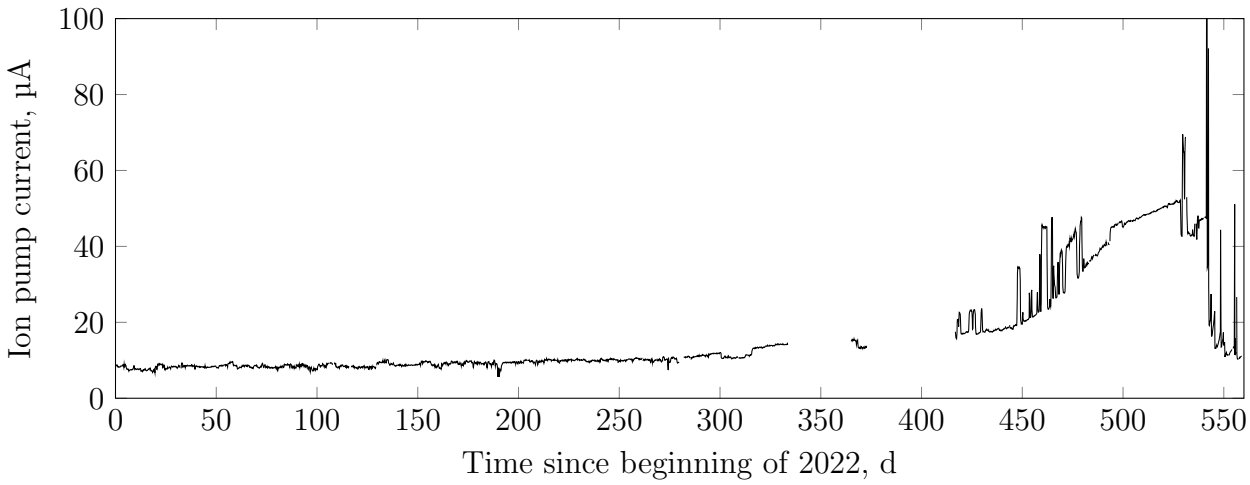


Figure 2.13: Ion pump current over time indicating a gradual rise in the background pressure. This was correlated with a decrease in the lifetime of atoms in our magnetic traps.

```
Julian  2:37 PM
    Minor fire above the chamber
    No obvious cause
Olive   2:37 PM
    Whoa
Julian  2:37 PM
    Old capacitor seems to be the only thing damaged
    Room smells really bad
Olive   2:39 PM
    Dang
    How did you notice it?
    Smell?
Julian  2:41 PM
    Yeah
    + smoke
```

Figure 2.14: Excerpt of my text conversation with Julian on September 18, 2023. The capacitor in question turned out to be a varistor.

vent the system for decommissioning, as baking was not an option. Ultimately, we were relieved of the responsibility of making this decision because the apparatus decided for us.

2.6.2 The fast end of E3

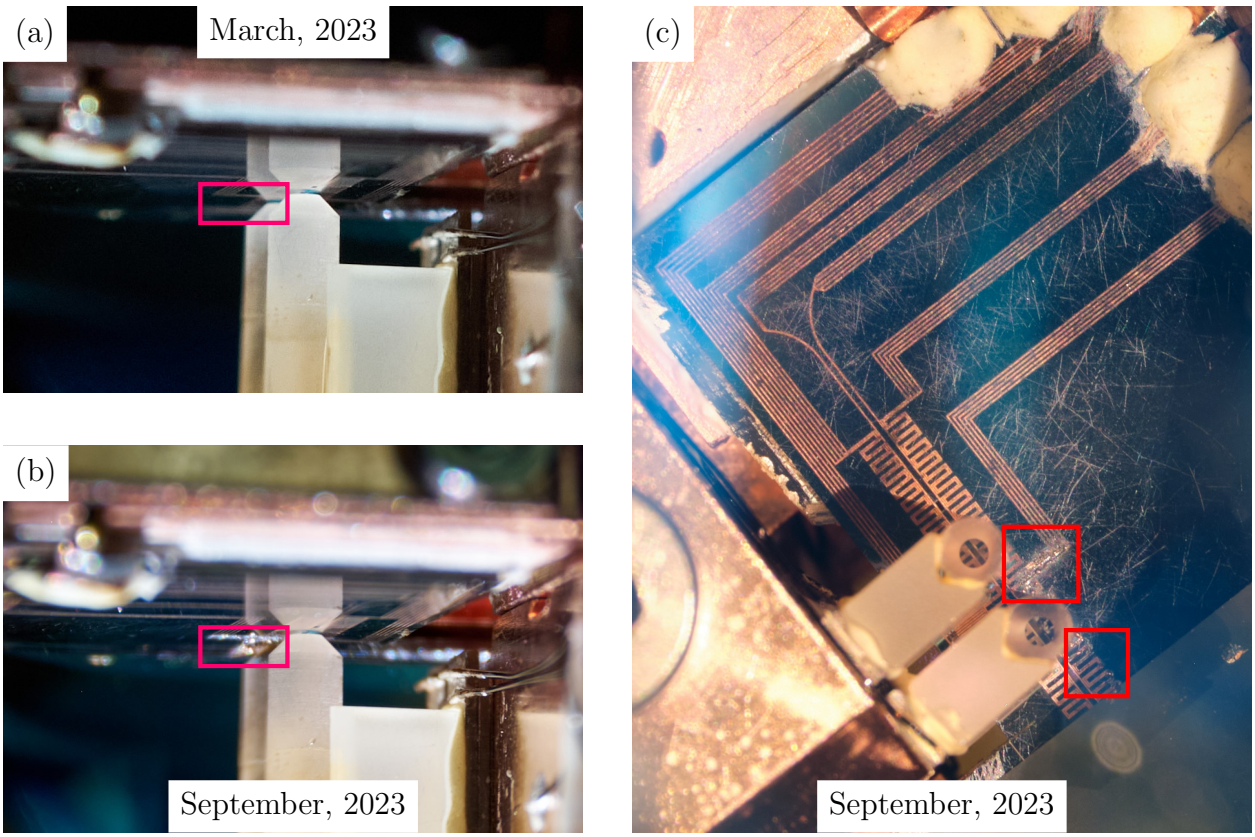


Figure 2.15: Photographs of the atom chip through the chamber viewports. (a) Photograph taken in March, 2023 looking directly through west-side chamber viewport, with the chip surface nearly edge-on. (b) Photograph taken in September, 2023 from nearly the same angle as (a). (c) Photograph taken in September, 2023 looking upwards through bottom chamber viewport, normal to chip surface.

On Monday, September 18, 2023 at approximately 2:23 pm, there was spontaneously a small fire in the laboratory, first noticed by those present in the room at the time by the distinctive smell of smoke from burning electronics. The smoke was traced to a varistor in the transfer box between the coil power supplies and the feed-through to the in-vacuum chip wires. The varistor is connected in parallel across the load, and best practice suggests that it be used in conjunction with a fuse connected in series from the power supply to the load [89] as depicted in Fig. 2.16, but in our case there was no such fuse. In retrospect, it is perhaps not surprising that the varistor could fail after millions of experimental cycles, as they degrade when subject to repeated surges. The basic purpose of a varistor is to turn short in response to too high of a voltage, so one could hope that if there had been a power surge from the supply that the vanishing resistance of the varistor would shield the sensitive in-vacuum wires. Unfortunately, this did not happen, and the varistor eventually catastrophically failed open, leaving the system unprotected. The corresponding chip conveyor wire experienced



Figure 2.16: (a) A parallel varistor provides overvoltage protection to a load coil. A short-circuit varistor failure can lead to catastrophic thermal runaway varistor failure in the absence of a fuse. Resulting open-circuit varistor failure may leave the load unprotected. (b) A parallel varistor provides overvoltage protection while a fuse provides overcurrent protection. The short-circuit varistor failure mode will likely open the fuse, disconnecting the supply from the load.

an overcurrent condition that overheated it to the point of catastrophic failure.

The first observed sign of intrachamber system damage was an enormous pressure spike measured by the ion pump current (up to $> 2.5\,\mathrm{mA}$, well above its usual range of 10–$50\,\mu\mathrm{A}$), followed by unprecedented modifications to the surrounding environment (typically the silhouette of the chip and the cavity mirrors) seen in the absorption images. Next, we observed anomalous, but not completely conclusive, measurements of the wire resistance across the feed-through. Finally, while the chamber was still under vacuum, I was able to use a digital camera with a telephoto lens to obtain conclusive photographic evidence of a catastrophic destructive event on the chip surface that we could conveniently compare to a photograph I had taken months before with the same alignment, shown in Fig. 2.15.

One of the conveyor wires heated to the point of phase change and became non-functional. Without both conveyor wires the apparatus was rendered unable to transport atoms magnetically, and it would no longer be possible to prepare atoms in the optical cavity. In late 2023 the experiment was decommissioned and disassembled, and many of its subsystems and parts have found new homes in the other active experiments in the group: E6, E8, and E9.

Chapter 3

Cavity–spin autonomous stabilization

The experimental results demonstrating cavity–spin optodynamical stabilization are published in Ref. [6]. In this chapter, I review some of the critical background information and discuss the core pillars of our experimental observations to motivate the analysis reported in the following chapter.

Angular momentum is quantized in units of the reduced Planck constant $\hbar$. Systems with angular momentum degrees of freedom (such as spins, dynamical systems with orbital angular momenta, and composite angular momenta formed through coupling) have played an enormous role in the development of quantum mechanics and are critical to understanding the structure of the atom. Coupling a spin system to an optical cavity mode facilitates high-sensitivity real-time measurement of the spin dynamics, and can simultaneously lead to coherent feedback effects as the spin modifies the evolution of the cavity mode which in turn drives evolution of the spin.

3.1 Introduction

In our apparatus we prepare clouds of a few thousand atoms trapped within and coupled to the mode of an optical cavity. The local intensity of the cavity mode as seen by the atoms depends on their position within the spatially varying cavity mode profile. The coupling strength depends on that local intensity and the atomic transitions available to be driven by the cavity mode and their selection rules. In this work we take the atoms to be localized at a local maximum of the cavity pump field such that the spatial variation can be approximately neglected.

We consider dispersive coupling, as described in Ch. 1 and in much greater detail in [73], where atomic excitations are rare and the cavity drives Raman transitions among the Zeeman sublevels of the ground-state hyperfine manifold. An atom constrained in this way to this manifold and initialized in the $f = 2$ manifold, as in our case, thus becomes a spin-2 system. This is illustrated in Fig. 3.1. For sufficiently large detuning Δ_{ca}, the contributions of the off-resonant couplings to the various f' manifolds result in an effective Hamiltonian

for the dispersive interaction that is derived in detail in Ref. [73]. I review the derivation in the following section.

As a reminder, in this work I use the cavity field creation and annihilation operators $\hat{c}^\dagger$ and $\hat{c}$ which obey the standard commutation relations $[\hat{c}, \hat{c}^\dagger] = 1$, with number operator $\hat{n} = \hat{c}^\dagger\hat{c}$, and collective spin operators $\hat{\boldsymbol{F}} = (\hat{F}_x, \hat{F}_y, \hat{F}_z)$ and spin ladder operators $\hat{F}_\pm = \hat{F}_x \pm \imath\hat{F}_y$. Lower-case spin operators $\hat{\boldsymbol{f}}$ act on individual atomic spins, with $\hat{\boldsymbol{F}} = \sum_{i=1}^{N_\mathrm{a}} \hat{\boldsymbol{f}}_i$.

Following [73], I will work within a sign convention where the atomic magnetic dipole moment is

$$\boldsymbol{\mu} = -g_f\mu_\mathrm{B}\hat{\boldsymbol{f}} = \hbar\gamma\hat{\boldsymbol{f}}, \tag{3.1}$$

in terms of the Landé g-factor g_f and gyromagnetic ratio $\gamma = -g_f\mu_\mathrm{B}/\hbar$. μ_B is the Bohr magneton and g_f is the Landè g-factor.

The coordinate systems are as shown in Fig. 3.3. The choice of axes follows that of Refs. [6, 7, 73], where the atomic quantization axis defined by the external magnetic field $\boldsymbol{B}$ is aligned with $\boldsymbol{z}$. The cavity is at an angle χ from $\boldsymbol{z}$ and we call its axis $\boldsymbol{k}$, and $\hat{F}_k = \hat{F}_x\sin\chi + \hat{F}_z\cos\chi$ is the spin projection onto the cavity axis. One can also also work with the spherical coordinates θ and ϕ which relate to the Cartesian coordinates by the definitions $\boldsymbol{x} = \cos\theta\cos\phi$, $\boldsymbol{y} = \cos\theta\sin\phi$, and $\boldsymbol{z} = \sin\theta$ but I will largely not, except for brief mention of the Larmor precession phase ϕ.

The quadratures of the cavity field are defined with the unitary normalization condition

$$\hat{c}^\mathrm{AM} = \frac{1}{\sqrt{2}}(\hat{c}^\dagger + \hat{c}) \qquad\qquad \hat{c}^\mathrm{PM} = \frac{\imath}{\sqrt{2}}(\hat{c}^\dagger - \hat{c}) \tag{3.2}$$

3.2 Cavity–spin optodynamical Hamiltonian

In Ch. 4 of this dissertation, I report a new theoretical analysis that builds from and extends those found in Refs. [6, 7, 73]. To motivate the experiment reported in the present chapter, I sketch the derivation of the Hamiltonian that describes our spin–cavity system and outline some of the basic phenomena found in its equations of motion.

The system Hamiltonian has three parts: one that describes the spin subsystem, one for the cavity subsystem, and one for the interaction between the two.

The Hamiltonian of the cavity mode in the laboratory frame is $\hat{H}_\mathrm{c}^\mathrm{lab} = \hbar\omega_\mathrm{c}\hat{c}^\dagger\hat{c}$, neglecting linear birefringence of the cavity[1]. It is easier to consider this from a frame rotating at the cavity pump laser frequency ω_p, in which

$$\hat{H}_\mathrm{c} = \hbar(\omega_\mathrm{c} - \omega_\mathrm{p})(\hat{n}_+ + \hat{n}_-) = -\hbar\Delta_\mathrm{pc}(\hat{n}_+ + \hat{n}_-), \tag{3.3}$$

with $\Delta_\mathrm{pc} \equiv \omega_\mathrm{p} - \omega_\mathrm{c}$, and here explicitly including photon number operators $\hat{n}_\pm = \hat{c}_\pm^\dagger\hat{c}_\pm$ for both circularly polarized cavity modes.

[1] In our experimental apparatus, the linear birefringence Δ_b was measured [73] to be $\Delta_\mathrm{b} = 2\pi\times 0.6\,\mathrm{MHz}$, which is sufficiently small compared our cavity linewidth $\kappa = 2\pi\times 1.82\,\mathrm{MHz}$ that when we drive the cavity with circularly polarized light we can neglect the birefringence and only consider a single circularly polarized cavity mode. See also Sec. 2.2.2 for a discussion of some of the systematic effects.

Neglecting interactions, a cloud of spinful atoms in a magnetic field has internal energy

$$\hat{H}_{\mathrm{s}} = \sum_i \boldsymbol{\mu}_{F,i} \cdot \boldsymbol{B}(\boldsymbol{r}_i) = \sum_i \hbar g_f \mu_{\mathrm{B}} \boldsymbol{B}(\boldsymbol{r}_i) \cdot \hat{\boldsymbol{f}}_i = \hbar \sum_i \omega_{\mathrm{s}}(\boldsymbol{r}_i) \hat{f}_{z,i} \tag{3.4}$$

where i indexes the atoms, and $\omega_{\mathrm{s}}(\boldsymbol{r}_i)$ is the Larmor frequency—the local spin precession frequency due to the externally applied magnetic field $\boldsymbol{B}$—at position $\boldsymbol{r}_i$. The dependence on position was included here for generality, but because the atoms are more tightly confined than the scale of spatial variations in the magnetic field, going forward we assume all atoms see the same intensity. This results in a Hamiltonian where all spins $\hat{\boldsymbol{f}}_i$ appear identically, work with the collective spin $\hat{\boldsymbol{F}} = \sum_i \hat{\boldsymbol{f}}_i$, such that

$$\hat{H}_{\mathrm{s}} = \hbar \omega_{\mathrm{s}} \hat{F}_z. \tag{3.5}$$

3.2.1 Dispersive interactions between a spin ensemble and a single-mode optical cavity

The interaction Hamiltonian describing atoms coupled to the cavity field is[2]

$$\hat{H}_I = \hbar \sum_i \sum_{g,e} \left[g^+_{g;e}(\hat{\boldsymbol{r}}^i) \hat{c}_+ \hat{\sigma}^i_{e;g} \delta_{m+1,m'} + g^-_{g;e}(\hat{\boldsymbol{r}}^i) \hat{c}_- \hat{\sigma}^i_{e;g} \delta_{m-1,m'} + \mathrm{h.c.} \right], \tag{3.6}$$

summing over all atoms i and over all possible transitions from the ground-state manifold $g = |f = 2, m\rangle$ to the excited states on the D_2 line of ^{87}Rb, where $g^{\pm}_{g;e}$ is the polarization-dependent coupling strength, and we have written it in terms of a Zeeman basis defined by the spin projection m onto the cavity axis, such that $\hat{f} \cdot \boldsymbol{k} |f, m\rangle = m |f, m\rangle$. The density operators acting on atom i are $\hat{\sigma}^i_{\alpha;\beta} = |\alpha\rangle_i \langle\beta|_i$ where $\alpha, \beta \in \{g, e\}$ index the atomic ground and excited states, respectively. I define the resonant coupling strength g_0 to be the cavity–atom coupling strength for an atom localized at a cavity antinode and driven on the D_2 cycling transition between $F = 2$ and $F' = 3$.

The terms of the above Hamiltonian describe the exchange of angular momentum between the cavity mode and the spins, with each term representing absorption or emission of a circularly polarized cavity photon and a corresponding spin-changing transition adding or removing spin angular momentum along the cavity axis $\boldsymbol{k}$. Only transitions for which $\Delta m = \pm 1$ are allowed, as encoded by the $\delta_{m,m'}$ terms. As described in detail in Ref. [73], for cavity–atom detuning $\Delta_{\mathrm{ca}} = \omega_{\mathrm{c}} - \omega_{\mathrm{a}}$ large in magnitude compared to the natural linewidth of the excited states and the coupling strength g_0, we can adiabatically eliminate the excited states to produce a spin-dependent dispersive interaction Hamiltonian. This describes effective dynamics within the ground-state manifold and has the form

$$\begin{aligned} \hat{H}_I \approx \hbar g_{\mathrm{c}} |U(\boldsymbol{r})|^2 \Big[& \alpha_0 (\hat{n}_+ + \hat{n}_-) + \alpha_1 (\hat{n}_+ - \hat{n}_-) \hat{F}_k \\ & + \alpha_2 \left\{ (\hat{n}_+ + \hat{n}_-)(\hat{F}_k)^2 - \hat{c}^\dagger_- \hat{c}_+ (\hat{F}_+)^2 - \hat{c}^\dagger_+ \hat{c}_- (\hat{F}_-)^2 \right\} \Big], \end{aligned} \tag{3.7}$$

[2] I am here using m to mean m_F the magnetic quantum number of the total atomic angular momentum.

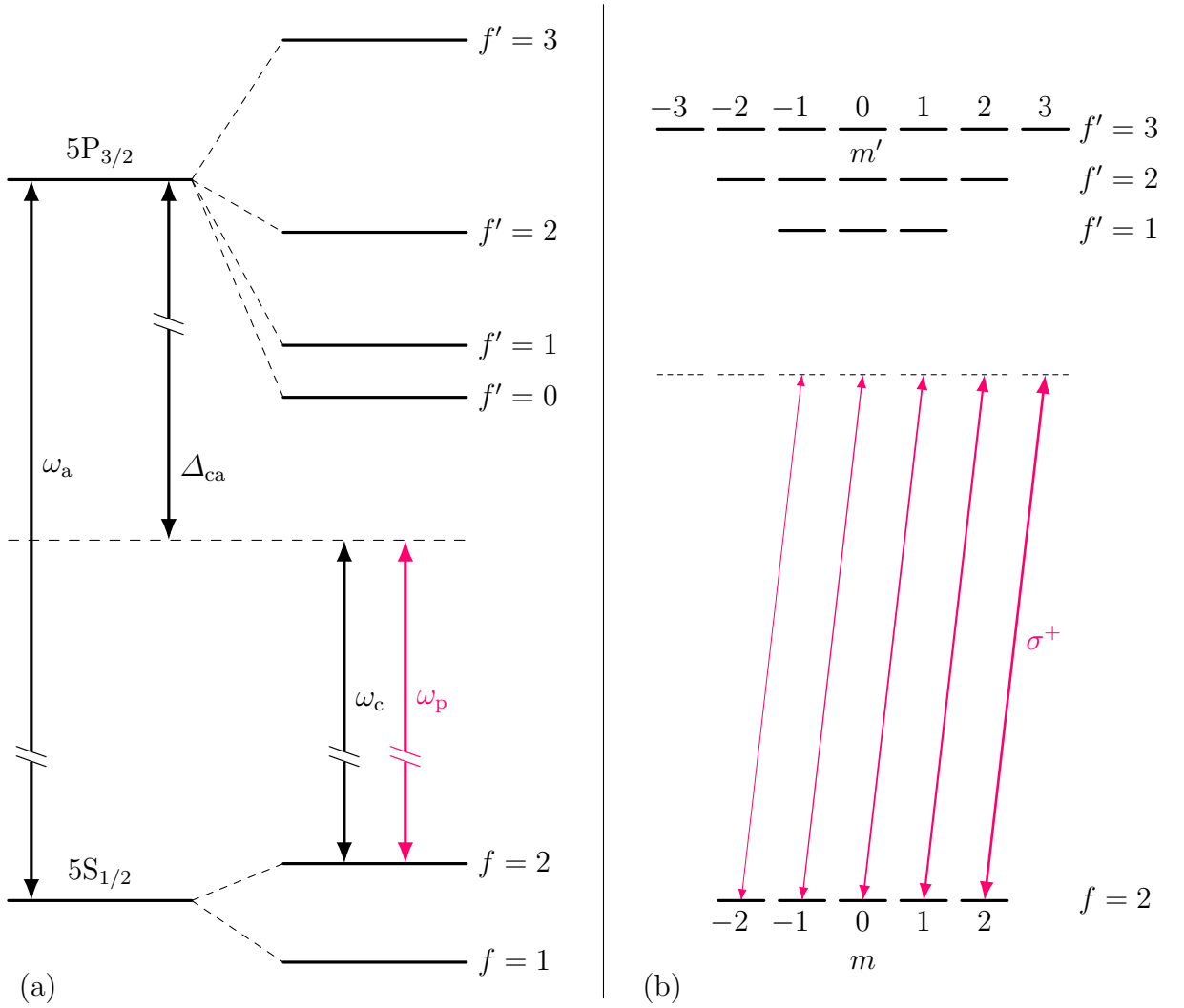


Figure 3.1: (a) Energy levels of the D_2 transition in ^{87}Rb. The atomic transition frequency ω_a is $2\pi \times 384.230\,484\,468\,5(62)$ THz which corresponds to a vacuum wavelength 780.241 209 686(13) nm. The hyperfine corrections, defined here as the frequency shifts of the f manifolds with respect to the fine-structure $5S_{1/2}$ and $5P_{3/2}$ states, are $\Delta_f = \{4.27167663181519(6), 2.56300597908911(4)\}$ GHz for the $f = \{1, 2\}$ ground state manifolds [30] and $\Delta_{f'} = \{302.0738(88), 229.8518(56), 72.9113(32), 193.7408(46)\}$ MHz for the $f' = \{0, 1, 2, 3\}$ excited states [32]. The depicted vertical scales of the ground and excited state manifolds differ. (b) Schematic of the dispersive coupling limit, with the cavity and external field taken here to be aligned. Vertical axis not to scale. *Adapted from Ref. [73].*

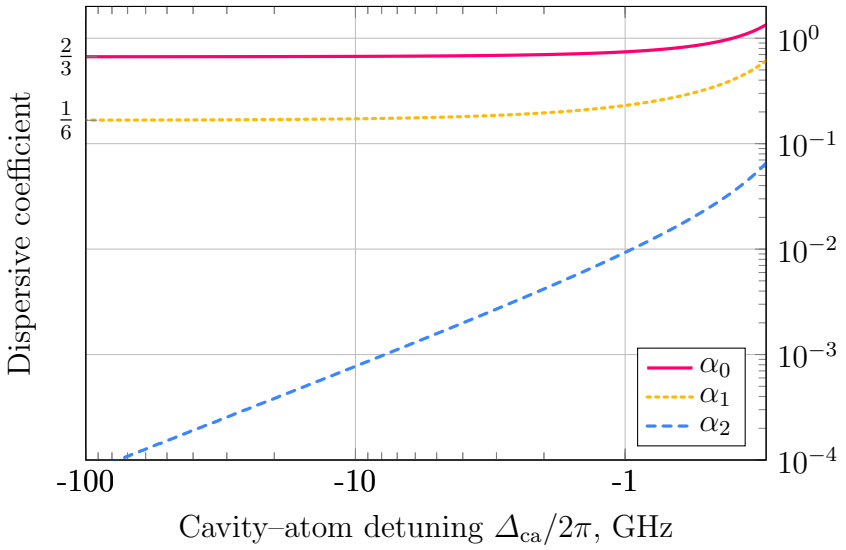


Figure 3.2: Dispersive spin coupling coefficients for ^{87}Rb in the $f = 2$ ground state as a function of the cavity–atom detuning Δ_{ca} from the D_2 transition. The coefficients α_0, α_1, and α_2 are the relative strengths of the scalar, vector, and tensor interactions, respectively. For $|\Delta_{ca}|/2\pi \gtrsim 1 - 10\,\text{GHz}$, the scalar and vector coefficients approach asymptotic values $\alpha_0 \to 2/3$, $\alpha_1 \to 1/6$, while the tensor interaction becomes negligible as $\alpha_2 \to 0$.

in terms of scalar, vector, and tensor interactions with the collective spin. $|U(\boldsymbol{r}_i)|^2$ is the spatially dependent dimensionless relative cavity pump intensity and in general leads to position-dependent coupling, through which the system can couple to motional degrees of freedom of the atoms and the phenomena of cavity optomechanics (discussed in Sec. 1.3). For all work discussed in this dissertation the atoms are positioned at an antinode of the cavity field, where the spatial dependence of the coupling is small, letting us take $|U(\boldsymbol{r})|^2 = 1$.

The above interaction further simplifies in the case that the magnitude of the detuning is much larger than the scale of the excited-state hyperfine structure, which in ^{87}Rb contains shifts of $\Delta_{f'} = \{-302, -230, -73, +194\}$ MHz [32]. For $|\Delta_{ca}| \gg |\Delta_{f'}|$, the tensor light shift becomes negligible, and we only consider the scalar and vector shifts.

We can also understand this interaction in terms of the Stokes polarization operators for the two orthogonal optical modes of the cavity

$$\hat{P}_x = -\frac{1}{2}\left(\hat{c}_+^\dagger \hat{c}_- + \hat{c}_-^\dagger \hat{c}_+\right) \qquad \hat{P}_y = \frac{\imath}{2}\left(\hat{c}_+^\dagger \hat{c}_- - \hat{c}_-^\dagger \hat{c}_+\right) \tag{3.8}$$

$$\hat{P}_z = \frac{1}{2}\left(\hat{c}_+^\dagger \hat{c}_+ - \hat{c}_-^\dagger \hat{c}_-\right) \qquad \hat{P}_0 = \left(\hat{c}_+^\dagger \hat{c}_+ + \hat{c}_-^\dagger \hat{c}_-\right) \tag{3.9}$$

which obey standard commutation relations $[\hat{P}_i, \hat{P}_j] = \imath\epsilon_{ijk}\hat{P}_k$ and $[\hat{P}_0, \hat{P}_i] = 0$. In these terms the interaction Hamiltonian is

$$\hat{H}_I \approx \hbar g_c |U(\boldsymbol{r})|^2 \left(\alpha_0 \hat{P}_0 N_a + 2\alpha_1 \hat{P}_z \hat{F}_k + \alpha_2 \left[\hat{P}_0 (\hat{F}_k)^2 + \hat{P}_+ (\hat{F}_-)^2 + \hat{P}_- (\hat{F}_+)^2\right]\right). \tag{3.10}$$

Prior calculations [73] determined the coupling constants for ^{87}Rb $F = 2$ atoms on the D_2 transition in the limit of large $\Delta_{\rm ca}$ to be $\alpha_0 \to 2/3$, $\alpha_1 \to 1/6$, and $\alpha_2 \to 0$. Dropping the tensor term in the case of large detuning and thus vanishingly small α_2, the interaction Hamiltonian is then

$$\hat{H}_I/\hbar = \sum_{\pm}[(\alpha_0 g_{\rm c} N_{\rm a} \pm \alpha_1 g_{\rm c}\hat{F}_z\cos\chi) \pm \alpha_1 g_{\rm c}\hat{F}_x \sin\chi]\hat{n}_{\pm}. \tag{3.11}$$

3.2.2 Full cavity–spin optodynamical Hamiltonian

In the dispersive limit described above, the Hamiltonian of the system (not including coupling to external radiation fields) is

$$\hat{H}/\hbar = \omega_{\rm s}\hat{F}_z + \sum_{\pm}[(-\Delta \pm g_{\rm s}\hat{F}_z\cos\chi) \pm g_{\rm s}\hat{F}_x\sin\chi]\hat{n}_{\pm}, \tag{3.12}$$

in terms of the pump detuning from the scalar-shifted cavity resonance $\Delta \equiv \Delta_{\rm pc} - \alpha_0 g_{\rm c} N_{\rm a}$ and the spin coupling strength $g_{\rm s} \equiv \alpha_1 g_{\rm c}$. In terms of the Stokes polarization operators it is

$$\hat{H}/\hbar = \omega_{\rm s}\hat{F}_z - \Delta_{\rm pc}\hat{P}_0 + g_{\rm c}\left(\alpha_0\hat{P}_0 + 2\alpha_1\hat{P}_z\hat{F}_k\right), \tag{3.13}$$

In comparison to the transverse spin components $\hat{F}_x, \hat{F}_y$ which essentially oscillate at the Larmor frequency $\omega_{\rm s}$, we will see that the longitudinal spin $\hat{F}_z$ varies relatively slowly (except for a small, fast oscillation around the slowly drifting average value). Anticipating this, we define $\hat{\Delta}_z \equiv \Delta + g_z\hat{F}_z$ to be the detuning between the pump and the vector-shifted cavity, which we understand to be a slowly varying "average" detuning when averaged over the fast Larmor precession cycle. From this point onwards, we consider only one driven polarization (and continue to neglect the linear birefringence $\Delta_b/\kappa \ll 1$), so we define $\hat{n} \equiv \hat{n}_-$ and $\hat{c} \equiv \hat{c}_-$ and write the system Hamiltonian in the form we will use for the remainder of the work:

$$\hat{H}/\hbar = \omega_{\rm s}\hat{F}_z - \left(\hat{\Delta}_z + g_x\hat{F}_x\right)\hat{n}. \tag{3.14}$$

For convenience we have introduced the coupling strengths of the x and z spin components $g_x \equiv g_{\rm s}\sin\chi$ and $g_z \equiv g_{\rm s}\cos\chi$.

To fully describe the dynamics, we must also consider the coupling of the cavity to the external radiation field, which we can imagine consists of an incident coherent drive plus a zero-temperature Markovian reservoir. A coherent drive of amplitude η can be incorporated by a Hamiltonian term $\hat{H}_{\rm d} = \hbar(\eta^*\hat{c}^\dagger + \eta\hat{c})$. Coupling to the reservoir requires treatment as an open quantum system; this leads to input vacuum noise and dissipation of the cavity field, as described in Refs. [90–92].

3.2.3 Conceptual picture of the system

Considering the Hamiltonian in Eq. (3.14), note that for $|g_{\rm s}|$ vanishingly small compared to $\omega_{\rm s}$, the system factors into just the bare energy of the cavity plus that of the spins.

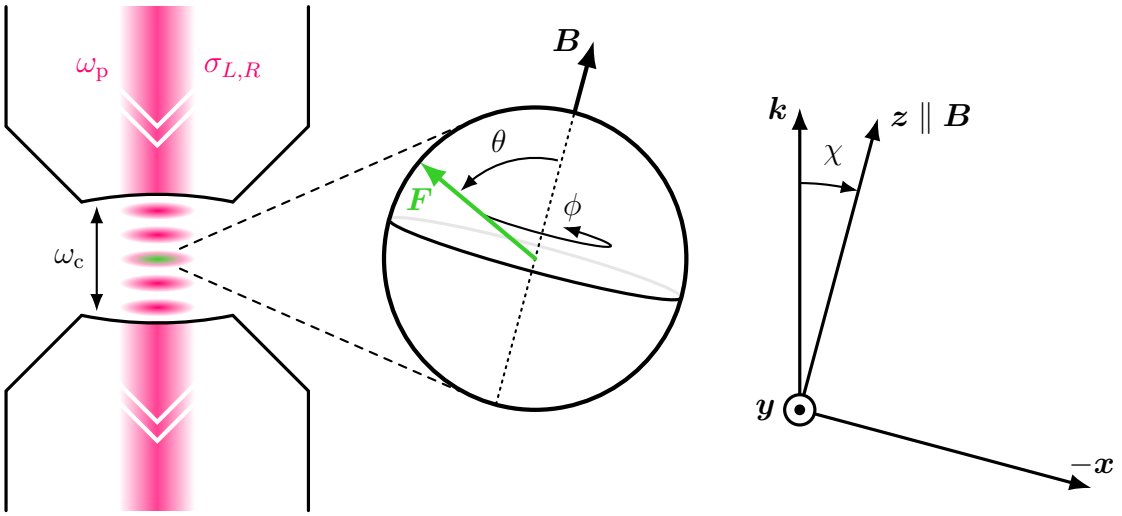


Figure 3.3: Cavity spin optodynamics system schematic. Atoms localized at an antinode of the cavity pump field. A magnetic field $\boldsymbol{B} = B\boldsymbol{z}$ is applied at an angle χ away from the cavity axis $\boldsymbol{k}$, which lies in the x–z plane. The cavity pump light is circularly polarized. There is a coupling between the cavity field and the collective spin of the atoms $\boldsymbol{F}$, which can be described in spherical coordinates on the collective Bloch sphere. The light transmitted through the cavity can be collected on a homodyne or heterodyne detector (not shown).

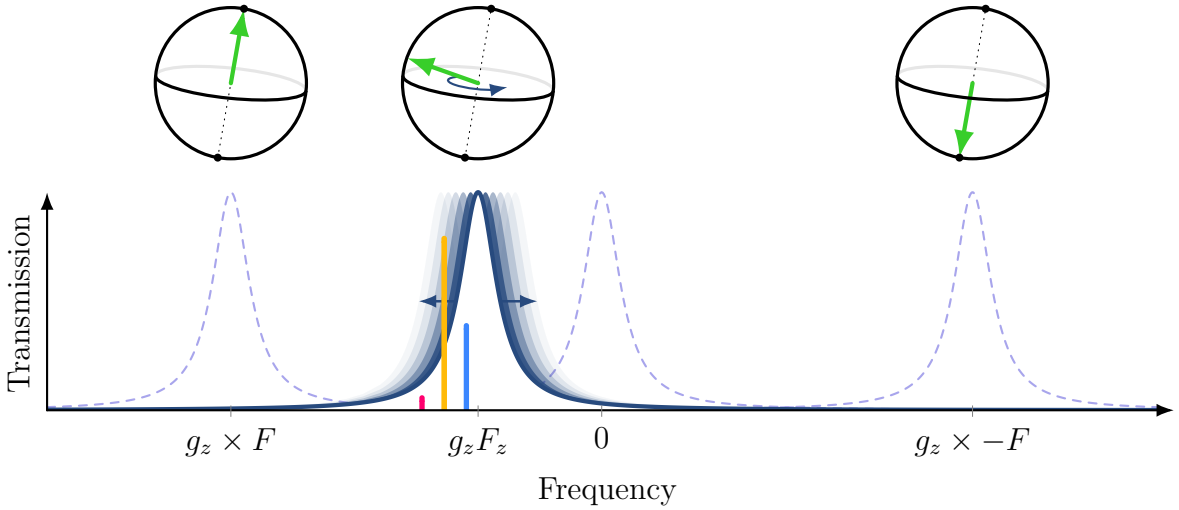


Figure 3.4: Schematic of the cavity transmission and light spectrum, shown for the case $\omega_s = \kappa$. Our experimental work was performed in the unresolved-sideband case $\omega_s \ll \kappa$, while the theoretical analysis of the next chapter considers arbitrary ratio of κ and ω_s including the case shown here. Sideband amplitudes are not to scale. Adapted from Ref. [7].

Inclusion of just the $g_z\hat{F}_z\hat{n}$ interaction term (equivalent to the "longitudinal field" case $\chi = 0$) introduces cavity feedback effects [93], but as it commutes with the bare energy terms, it introduces energy shifts but does not change the eigenstates of the system.

On the other hand, the $g_x\hat{F}_x\hat{n} \propto g_x(\hat{F}_+ + \hat{F}_-)\hat{n}$ term does not commute with the bare energy terms. Considering this term $\propto g_x$ as the sole perturbative interaction to the bare Hamiltonian, we might expect that to see transitions between neighboring Zeeman levels, with each transition exchanging energy $\hbar\omega_\mathrm{s}$ between the spins and the cavity mode. This term $\propto g_x$ resembles the interaction found in a standard optomechanical Hamiltonian, there responsible for Stokes and anti-Stokes processes that exchange energy between the mechanical mode and the cavity [50, 55, 94]. Each such Stokes (anti-Stokes) scattering event destroys a cavity photon and creates one with $\hbar\omega_\mathrm{s}$ less (more) energy, while adding (removing) $\hbar\omega_\mathrm{s}$ energy to the spins. Importantly, within the cavity, the system will preferentially scatter on either the Stokes or anti-Stokes line depending on which one produces light closer to resonance with the cavity. This process is observable in real-time by inspection of the light leaving the cavity. For cavity pump light at ω_p the Stokes and anti-Stokes processes generate light at $\omega_\mathrm{p} - \omega_\mathrm{s}$ and $\omega_\mathrm{p} + \omega_\mathrm{s}$ respectively[3]. In the case that this is the only interaction term (corresponding to the "transverse field" case $\chi = \pi/2$) then whichever of the Stokes or anti-Stokes processes is relatively stronger will remain that way throughout the evolution of the system because the average detuning Δ is static (assuming fixed N_a). Over time, the asymmetric scattering rates will lead to drift of $\hat{F}_z$ as the spin approaches either the north or south pole of the collective Bloch sphere depending on the sign of Δ. This process is analogous to cavity optomechanical cooling [95–101].

Now we turn our attention to the case of a tilted field $0 < \chi < \pi/2$ where the Hamiltonian is given by Eq. (3.14). We can understand this by imagining either of the two limits above and turning the field angle by a small amount. The general picture is that the $\hat{F}_x$ term drives a drift of $\hat{F}_z$ in a direction that depends on the average detuning, which itself depends on the value of $\hat{F}_z$. For some values of $\hat{F}_z$ then the drift might be towards the north pole while for others it would be towards the south pole. There exists an equilibrium point where the Stokes and anti-Stokes processes are roughly even: where the average detuning is zero.

There are then two cases that we describe as having either positive or negative feedback gain, determined by the relative signs of g_s (through Δ_ca), which circular polarization mode is being driven (as we earlier had both $\hat{n}_+$ and $\hat{n}_-$ which appeared in the interaction term with different signs), and the direction of the magnetic field (a rotation by 180° around $\boldsymbol{y}$ would change the relative sign between the interaction term and the Zeeman term). With our conventions, the sign of the feedback is

$$\begin{aligned}\operatorname{sgn}(\text{feedback}) &= \operatorname{sgn} g_\mathrm{s} \times \operatorname{sgn}\cos\chi \times \operatorname{sgn}(\hat{n}_+ - \hat{n}_-) \\ &= \operatorname{sgn}(g_z) \times \operatorname{sgn}(\hat{n}_+ - \hat{n}_-)\end{aligned} \tag{3.15}$$

[3]These frequencies describe the first-order sidebands, which for weak interaction offer a good description of the phenomenon at hand. There are higher-order effects, including Stokes and anti-Stokes scattering of light that is already at $\omega_\mathrm{p} \pm \omega_\mathrm{s}$, and the tensor interaction term which we neglect.

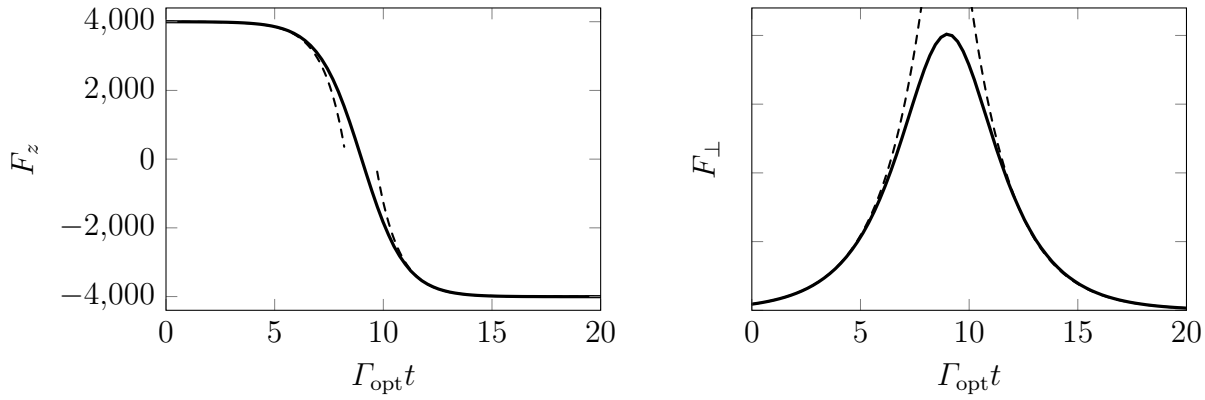


Figure 3.5: Semiclassical dynamics of the transverse-field ($\chi = \pi/2$) cavity–spin system with the $F = 4000$ spin prepared near a pole with $F_z = F - 1$ and the cavity driven below resonance. Near the poles, the longitudinal spin evolves like $F_z(t) = F - (F - F_z(0))e^{\Gamma t}$, and the magnitude of the transverse spin like $F_\perp(t) = F_\perp(0)e^{-\Gamma t/2}$ where $F_\perp^2 = F_x^2 + F_y^2$. The heating/damping rate Γ_{opt} used here is Γ_z taken to the transverse-field case $\chi = 0$ with $\Delta \neq 0$. Figure reproduced from Ref. [73].

In the positive-gain case, positive (negative) average detuning causes drift of $\hat{F}_z$ that shifts the average detuning to be even more positive (negative), and in each case the system will drift toward a pole of the collective Bloch sphere. In this way, the system amplifies fluctuations away from the equilibrium point.

In the negative-gain case, considered for the remainder of this work, the interplay works oppositely: the drift of $\hat{F}_z$ is such that the average detuning evolves in the direction of zero, and the system drifts toward the equilibrium point. Assuming the system is able to reach it[4], we determine that the steady-state or equilibrium value of the longitudinal spin will be

$$F_z^{\text{equil}} = -\frac{\Delta}{g_z}, \tag{3.16}$$

which depends on the cavity pump frequency through Δ but not on the initial spin state. In this case the spin system exhibits damping, akin to stabilization of a feedback system with negative gain. This is different than the analogy to standard optomechanical cooling from earlier because here the system can "cool" to any latitude on the collective Bloch sphere rather than just to one of the poles.

3.2.4 Semiclassical equations of motion

In the Heisenberg picture, the Hamiltonian in Eq. (3.14) generates time-evolution of the operators given by the Heisenberg equations of motion. We will also include coupling to

[4]Spin dephasing limits this, as well as the dynamic range of the spin (it cannot go beyond the poles of the collective Bloch sphere).

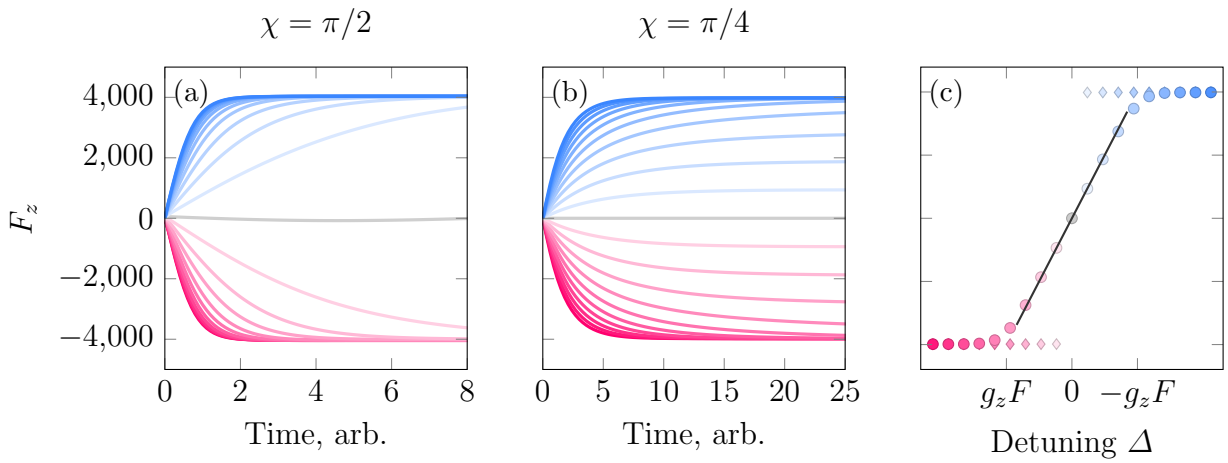


Figure 3.6: Semiclassical dynamics for a spin $F = 4000$ initialized at the equator in a cavity driven by a pump at various detunings. Positive-(negative-)detuning trajectories are shown in blue (red) and darker lines correspond to larger detuning magnitude. (a) Transverse field case. The trajectories tend towards either the north or south pole of the collective Bloch sphere except for the case $\Delta = 0$. (b) Tilted field case under negative (stabilizing) feedback conditions. The trajectories tend towards steady-state values of F_z proportional to the detuning as in Eq. (3.16). (c) The steady-state value of F_z as a function of the detuning. The circles are for the negative-feedback condition shown in (b), while the diamonds show simulations under positive-feedback conditions. Under negative feedback, the steady-state value of F_z follow Eq. (3.16) near $\Delta = 0$ (black line).

external radiation modes that incorporate a coherent drive and dissipation in Lindblad form. I examine the resulting equations in greater detail in Ch. 4, but for now I will work with a semiclassical version of these equations in which the operators are treated like classical numbers, and focus on the expectation values of the operators and thus ignore the vacuum input noise.

Including the drive η and the cavity field decay rate κ, the semiclassical equations are

$$\begin{aligned} \dot{F}_x &= -\omega_s F_y + g_z n F_y \\ \dot{F}_y &= \omega_s F_x - n(g_z F_x - g_x F_z) \\ \dot{F}_z &= -g_x n F_y \\ \dot{c} &= \imath \Delta_z c + \imath g_x F_x \, c + \eta - \kappa c. \end{aligned} \tag{3.17}$$

The evolutions of the spin components depend on torques from the external magnetic field and the effective magnetic field of the cavity mode: in this picture, cavity photons act on the spins like a fictitious magnetic field oriented along the cavity axis. The cavity field accumulates phase depending on detuning, is driven by coherent input η and decays at rate κ. I integrate these equations numerically and show the results in Figs. 3.5, 3.6, and 3.7.

Note that evolution under these equations of motion produces rapid modulation of F_z. It turns out that this is due to the misalignment of the total magnetic field and the external field, the latter of which we have used as the quantization axis. Rotating to the frame defined by the average total field essentially eliminates the fast modulation, as would averaging the dynamics over the Larmor precession period. In Ch. 4, I discuss this further and introduce linearized equations of motion that offer the same clarification. I show in Fig. 3.7(b) a comparison between the dynamics with and without the fast modulation.

As shown in detail in Ch. 4 for the quantum-mechanical versions of the above equations, we can trace out the cavity degrees of freedom by finding an approximate form of the cavity field in terms of the spin, then substitute back in to find effective equations of motion in terms of just the spin. Solving the above equations for the cavity field we find

$$c(t) \approx \sqrt{\bar{n}} \left(1 + \frac{\imath g_x}{2} \left[(\kappa + \imath(-\Delta_z + \omega_\mathrm{s}))^{-1} F_+ + (\kappa + \imath(-\Delta_z - \omega_\mathrm{s}))^{-1}\right] F_-\right). \tag{3.18}$$

Substituting this back in, for $F_z^{\mathrm{equil}} = 0$ the longitudinal spin evolves according to

$$F_z \approx -\Gamma_z F_z, \tag{3.19}$$

where

$$\Gamma_z \equiv -2\bar{n} g_x^2 g_z F^2 \kappa \omega_\mathrm{s} / (\kappa^2 + {\omega_\mathrm{s}}^2)^2 \tag{3.20}$$

is the damping rate. Note that the sign of the damping rate matches Eq. (3.15).

The evolution of the transverse spin components meanwhile is modified to precession at an effective Larmor frequency $\omega_\mathrm{s}' = \omega_\mathrm{s} + g_z \bar{n}$ due to the fictitious field. The fictitious field also leads to an average reorientation of the total magnetic field such that precession does not occur in the original plane selected by the external field. This produces fast oscillation of F_z in the basis determined by the external field axis. If the depth of cavity modulation $|g_x|F/\kappa$ is not too large then the photon number does not fluctuate very far from its mean value and we can regard this field reorientation as almost static. Then we can equivalently consider a basis determined by the total field axis and absorb the static shifts into redefinitions of the variables.

3.2.5 Atomic scattering and excited-state adiabatic elimination

Atoms exposed to light will generally scatter photons. A photon resonant with an atomic transition can be absorbed to create an atomic excitation, which will undergo spontaneous decay with rate Γ. Off-resonant photons can also be scattered. Considering a two-level atom in free-space subject to a coherent drive of Rabi frequency Ω and detuning Δ_a, the probability of finding the atom in its excited state is $P_\mathrm{e} \sim (\Omega/\Delta_\mathrm{a})^2$ for $|\Delta_\mathrm{a}| \gg \Gamma$. The scattering rate is then $\Gamma_\mathrm{sc} \sim \Gamma(\Omega/\Delta_\mathrm{a})^2$.

Now consider the atom coupled to a driven cavity with resonant coupling strength g_0, field decay rate κ (photon loss rate 2κ), and average photon number $\bar{n}$. We take the cavity

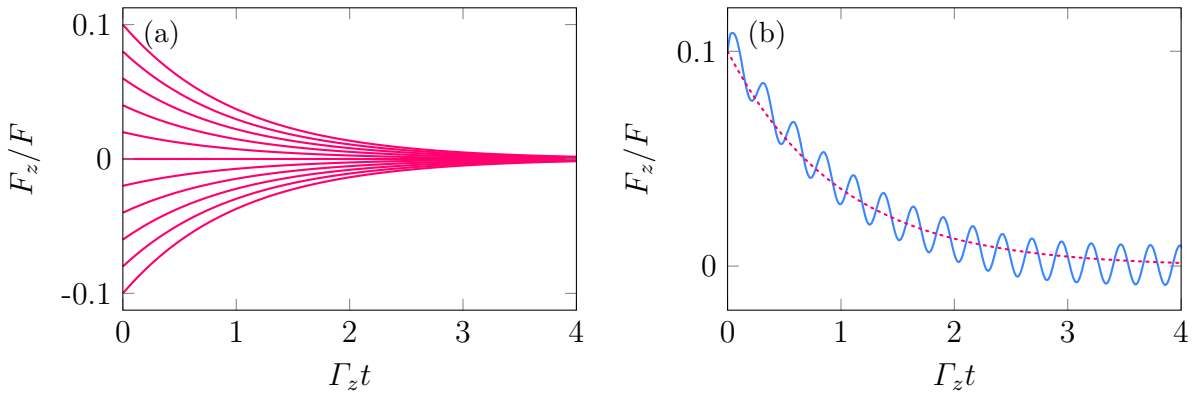


Figure 3.7: Semiclassical dynamics in a tilted field for a spin initialized away from the equator in a cavity driven by a pump with $\Delta = 0$ ($F_z^{\text{equil}} = 0$). The trajectories are nearly exponential with decay rate Γ_z and approach the steady-state value given by Eq. (3.16), here taken to be $F_z = 0$. (a) Several trajectories for different initial displacements from the equator. (b) Damping under the full semiclassical equations of motion Eqs. (3.17) (solid line) versus the linearized equations described in the text and analogous to Eqs. (4.86) (dotted line).

to be far-detuned from the atomic transition with detuning $\Delta_{\text{ca}} = \omega_{\text{c}} - \omega_{\text{a}}$ taking on the role of Δ_{a}. The scattering rate is then

$$\Gamma_{\text{sc}} \sim \bar{n}\Gamma \frac{g_0^2}{\Delta_{\text{ca}}^2}. \tag{3.21}$$

This amounts to a spin decoherence process that we neglected by adiabatically eliminating the excited atomic states. For our experimental parameters, the scattering rate is roughly $\Gamma_{\text{sc}} \sim 14\,\text{s}^{-1}$, which is much smaller than the damping rate Γ_z observed in Fig. 3.9 (and our predictions for it in Ref. [6] and reported in Ch. 4). This decoherence sets in on timescales $\sim 1/\Gamma_{\text{sc}} \gg 1/\Gamma_z$. This indicates that neglecting this decoherence in our analysis should not be significantly misleading on timescales $\sim 1/\Gamma_z$. But as we will see in Ch. 4, scattering introduces a limit [102–106] to the system behavior at long times $> 1/\Gamma_z$.

3.2.6 Optical detection of collective atomic spin states

The description in this section follows that of Ref. [7] closely.

With the magnetic field and cavity axes aligned ($\chi = 0$), we have $\hat{F}_k = \hat{F}_z$, and Eq. (3.14) becomes

$$\hat{H}^-/\hbar = \omega_{\text{s}}\hat{F}_z - \left(\Delta_{\text{pc}} - \alpha_0 g_{\text{c}} N_{\text{a}} + \alpha_1 g_{\text{c}}\hat{F}_z\right)\hat{n}, \tag{3.22}$$

where the superscript indicates that we are driving the mode corresponding to $\hat{n}_-$, and which commutes with the z component of $\hat{F}$ (which we sometimes call the "spin energy" or the "longitudinal spin"). In this configuration we can drive the cavity, vary ("sweep") the frequency of the driving laser, and measure the power of light transmitted through

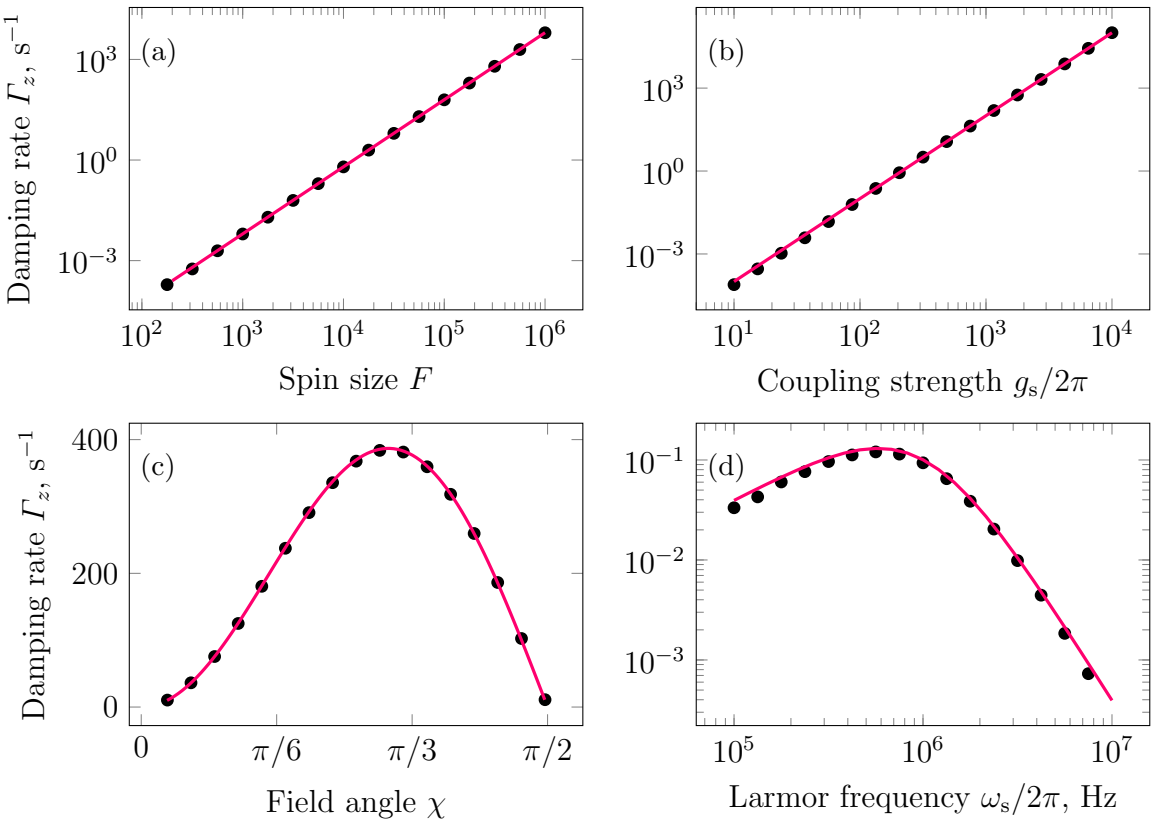


Figure 3.8: Values of the damping rate Γ_z from fits to semiclassical simulations (points) and from Eq. (3.20) (lines). The parameters are $\kappa = \omega_s = 2\pi \times 1\,\mathrm{MHz}$, $g_s = \kappa/10^4$, $\bar{n} = 20$, $\chi = 10^{-2}$, and $F = 4000$ (except where that parameter is varied along the horizontal axis).

the cavity as a function of the drive frequency; we fit a Lorentzian function to this and extract the dispersively shifted cavity–atom resonant frequency. Combined with a subsequent measurement performed at the end of each experimental sequence after the atoms have been expelled, this amounts to a measurement of the dispersive shift

$$\begin{aligned}\hat{\Delta}_N^- &= -\alpha_0 g_c N_a + \alpha_1 g_c \hat{F}_z \\ &= \frac{1}{6} g_c \left(-4N_a + \hat{F}_z\right)\end{aligned} \tag{3.23}$$

and thus measures a combination of the total atom number and the spin projection $\hat{F}_z$. In the above expression I have substituted the asymptotic numerical values for α_0 and α_1 discussed earlier. To distinguish the two unknown[5] quantities and realize measurements of

[5]Experimentally, the initial atom number varies slightly from one experimental run to the next due to fluctuations in the state preparation process, and the atom number measured at various times through the experiment will reflect a small degree of atom loss, also variable.

N_a and $\hat{F}_z$ separately, we need to perform a second measurement.

We measure the dispersive shift again but driving the cavity with the opposite circular polarization. This realizes the Hamiltonian

$$\hat{H}^+/\hbar = \omega_\mathrm{s}\hat{F}_z - \left(\Delta_\mathrm{pc} - \alpha_0 g_\mathrm{c} N_\mathrm{a} - \alpha_1 g_\mathrm{c}\hat{F}_z\right)\hat{n}, \tag{3.24}$$

which differs from $\hat{H}^-$ in the sign of the $\hat{F}_z$ term. Repeating the frequency sweep now measures the dispersive shift

$$\begin{aligned}\hat{\Delta}_N^+ &= -\alpha_0 g_\mathrm{c} N_\mathrm{a} - \alpha_1 g_\mathrm{c}\hat{F}_z \\ &= \frac{1}{6} g_\mathrm{c}\left(-4N_\mathrm{a} - \hat{F}_z\right).\end{aligned} \tag{3.25}$$

We accomplish this by synchronously controlling a pair of liquid-crystal variable waveplates (LCVWPs): the first, located before the cavity in the pump beam path, rapidly switches the polarization of the light driving the cavity. The second is in the path of the cavity output light before the polarization-sensitive heterodyne detector and ensures that it tracks the driving polarization. With measurements of both $\Delta_N^\pm$ (plus knowledge of , we can determine

$$N_\mathrm{a} = -\frac{3}{4}\frac{\Delta_N^+ + \Delta_N^-}{g_\mathrm{c}} \tag{3.26}$$

$$F_z = -3\frac{\Delta_N^+ - \Delta_N-}{g_\mathrm{c}}. \tag{3.27}$$

There are other experimental methods to perform a pair of Δ_N measurements that also amount to switching the sign of the $\hat{F}_z$ term to decouple N_a and $\hat{F}_z$. One would be to flip the magnetic field orientation from $\chi = 0$ to $\chi = 180°$ such that $\hat{F}_k = -\hat{F}_z$. In our experiment this field reorientation, limited by the L/R time constant of the electromagnetic coils, is too slow to be practical. Another is to apply a radio-frequency pulse to the spins that drives a π-pulse to map $\hat{F}_z \to -\hat{F}_z$ between the two Δ_N measurements. This method was used historically in our experiment [73] but the calibration is more sensitive than the approach with the LCVWPs, which is why we switched to using the variable waveplates.

We have also demonstrated a third method, explained in Ref. [7], in which we drive the cavity with linearly polarized light. This excites both non-degenerate circularly polarized eigenmodes[6] of the cavity–atom system and produces sweep traces that are no longer Lorentzian but instead are bimodal[7] from which we can extract both $\Delta_N^\pm$ directly from a single sweep.

We perform this optical measurement of N_a and $\hat{F}_z$ immediately after preparing the atomic ensemble in the cavity before switching the field configuration to engineer the Hamiltonian under study, and after a set interaction time we rotate the field back and repeat the measurement. In this way we determine N_a and $\hat{F}_z$ of before and after the interaction.

[6]Here I am neglecting linear birefringence of the cavity. Refer to Sec. 2.2.2 for a discussion.

[7]So long as the spin projection onto the cavity axis is not zero.

3.3 Observation of autonomous cavity–spin feedback

In this section, I discuss some of the results of experiments completed in 2023 and published along with an initial theoretical model in Ref. [6], and draw from that text somewhat.

The state and evolution of quantum systems can be tailored by feedback control [107–110], as in the case of classical control theory. At a scientific level, the development of a quantum control theory, one that integrates entanglement and nonclassical effects of dissipation and measurement, opens a new line of inquiry into nonequilibrium and open quantum systems. At an applied level, feedback control allows quantum devices to operate robustly, mitigating errors in system preparation and calibration as well as the effects of decoherence. Feedback control underpins important tasks including error correction in quantum computation [111–113] and sensing [114–116], entanglement purification [117], and adaptive measurement [118]. Quantum feedback control can be divided broadly into two categories: measurement-based and autonomous feedback. In the measurement-based approach, properties of a quantum system are read out classically; the measurement record is used by an external classical control device to alter the coherence, dissipation, and measurement operations on the system [93, 119–124]. The feedback system's design must account for noise and backaction that are intrinsic to quantum measurement. By comparison, in autonomous (or coherent) quantum feedback, the corrective response that steers a subsystem is built into the quantum system itself. Control is achieved by structuring the drive and dissipation of an open quantum system so that entropy is extracted as the quantum system is steered to a desired state. Examples of such schemes include autonomous error correction in bosonic code spaces [125–127], quantum state preparation [128–133], optical noise cancellation [134], and spin squeezing of atoms in a driven optical resonator [135].

3.3.1 Experimental results

The experimental sequence begins with stages of cooling, trapping, transport, state preparation, and other steps that are described in Ch. 2.1 and with greater detail in Refs. [7, 73]. We measure the atom number dispersively as described in Sec. 3.2.6, then use a radio-frequency radiation pulse prepare the atomic cloud in a coherent spin state, typically with $\langle \hat{F}_z(t=0) \rangle = 0$ such that $\Delta_z(t=0) = \Delta$. We tilt the field to an intermediate angle χ typically around $30 - 60°$, and then initiate the optodynamic feedback interaction by ramping up the cavity pump laser, held at a fixed frequency. The cavity–spin system is then allowed to evolve under constant external conditions for a set period of time during which a portion of the light leaving the cavity is measured in real-time with our balanced heterodyne detector [48, 49, 56]. This allows us to reconstruct the Stokes and anti-Stokes scattering rates throughout the evolution of the system. After the interaction time we ramp down the intensity of the cavity pump, return the field to alignment with the cavity axis, and perform a dispersive measurement of N_a and $\hat{F}_z$. We then eject the atoms from the cavity and measure the frequency of the empty cavity, which completes the experimental cycle.

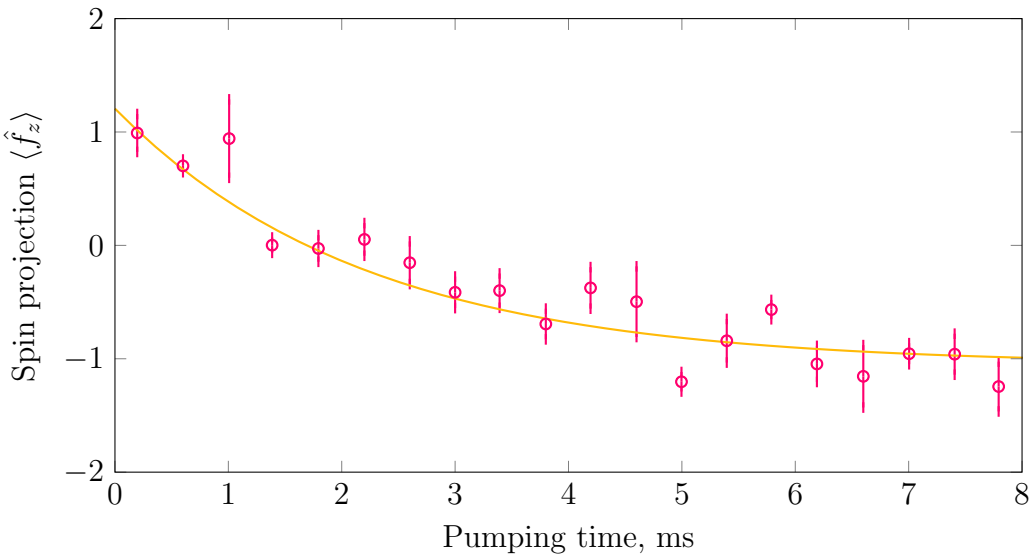


Figure 3.9: Time-domain response of the autonomous feedback system to a step impulse. The spin is prepared near $\langle \hat{f}_z \rangle = +1$ and the system is driven with a constant pump detuning Δ that corresponds to $F_z^{\text{equil}}/N_{\text{a}} = -1$ for a varying amount of time, after which the spin projection is determined by dispersive measurement (circles) to reconstruct the average spin trajectory. An exponential fit is used to extract the damping rate $\Gamma = 450(60)\,\text{s}^{-1}$ (line). Error bars represent standard errors on the mean, taken over 20 repetitions of the experiment. The data were recorded at $\chi = 60°$. Figure adapted from Ref. [6].

By repeating the experiment with different choices of Δ, we observe that the final spin closely follows the behavior predicted by Eq. (3.16) within a certain setpoint tuning range, outside of which either the equilibrium point is inaccessible given the finite dynamic range of the spin or the damping is too slow to reach the setpoint before dephasing (or the conclusion of the interaction time). The measurements, previously reported in Refs. [6, 7], are in agreement with our model for the determined system parameters.

We also conduct measurements in another configuration, where all system parameters are held fixed but we change the interaction time across different realizations, allowing us to halt the evolution at different time points and measure the longitudinal spin projection as a function of time. These data have been previously reported alongside those described above, and I also show them here in Fig. 3.9. They show the longitudinal spin undergoes exponential damping toward the setpoint determined by Δ. The damping rate is determined experimentally to be $450(60)\,\text{Hz}$ for our system parameters, which agrees roughly with the theoretical model reported in Refs. [6, 7] and with that to be derived in Ch. 4.

3.4 Conclusion

In this work and in the more complete description of the experiments in Refs. [6, 7], we demonstrated and explained autonomous feedback generated by the dissipation of a driven cavity onto a collective spin, and shown that it stabilizes the spin at an energy (longitudinal spin) determined by the cavity pump frequency. Feedback can not only steer the measured quantity, here the components of the collective spin, but in principle can also affect fluctuation and the noise spectrum. The spin responds to and entangles with quantum noise of the cavity field, generating fluctuations in the longitudinal and transverse spin components. Simultaneously, coherent feedback that stabilizes the longitudinal spin should suppress longitudinal spin fluctuations. The balance between quantum-optical fluctuations and dissipation is the subject of Ch. 4 of this dissertation.

The cavity emission offers a real-time record of the feedback dynamics. In Ch. 4, I also study the information encoded in this optical signal and how it can be used to enhance the feedback stabilization through additional measurement-based feedback.

Chapter 4

Cavity–optodynamical autonomous spin squeezing

In this chapter, I will theoretically analyze the spin squeezing generated by the optodynamical Hamiltonian introduced in Ch. 3. The material in this chapter is being prepared as part of a forthcoming manuscript.

4.1 Introduction

Squeezing, as a form of entanglement, is a strictly quantum-mechanical phenomenon; it is a reduction of the uncertainty associated with a particular system variable and the corresponding increase of the uncertainty associated with the conjugate of that variable [136]. Considering a spin F, the Heisenberg uncertainty principle states

$$V_y V_z \geq |\langle[\hat{F}_y, \hat{F}_z]\rangle|^2/4 = \langle\hat{F}_x\rangle^2/4, \tag{4.1}$$

where V_z (often written $\Delta {F_z}^2$) represents the variance of measured values of $\hat{F}_z$, and we work with $\hbar = 1$ and unitless spin variables. Consider a collective spin with mean spin vector oriented along $\boldsymbol{x}$. The components along $\boldsymbol{y}$ and $\boldsymbol{z}$ are then bound by $V_y V_z \geq F^2/4$. Absence of entanglement among the elementary spins would realize the special case $V_y = V_z$ and we call such an unentangled state a coherent spin state (CSS)[1]. A state with entanglement can have a reduced uncertainty in one of the transverse components but an increased uncertainty in the other transverse component, a property called squeezing.

Quantum fluctuations of light set a limit on the possible precision of measurements performed with an interferometer, and fluctuations of a spin set a limit on the precision of measurements using the spin to, for example, measure the strength of an unknown magnetic field. By entangling the light, or spins, the fluctuations can be made to destructively interfere such that the measurement sensitivity increases [137]. The production entanglement and

[1]Some authors use the term *spin coherent state*.

squeezing of a spin ensemble has become an active area of research in recent years as well, motivated largely by its application in quantum-enhanced metrology using spins [137–143], similar to the situation with light.

In this work I will explore a system that I predict to squeeze the variance V_z of a spin ensemble. I will follow a convention in which I use the term squeezing to specifically refer to states that not only feature a reduced variance but that possess entanglement among the elementary spins in such a way as to reduce the noise-to-signal ratio $V_z/|\langle\hat{\boldsymbol{F}}\rangle|^2$ relevant for metrological purposes [35]. At various points I will refer to the "longitudinal" and the "transverse" spin components. By longitudinal spin I will mean $\hat{F}_z$, the component of the spin along the quantization axis set by the external magnetic field, and the transverse spin $F_\perp$ will mean the spin component transverse to the longitudinal spin but aligned with the mean spin vector. I will sometimes refer to it this way rather than referring to $\hat{F}_x$ or $\hat{F}_y$ specifically because the external magnetic field causes fast precession in the $\boldsymbol{x}-\boldsymbol{y}$ plane. Ordinarily one might move into a frame rotating at the precession frequency, but I do not do that here.

Optodynamical damping, discussed previously in Sec. 3.3, brings the spin toward an asymptotic state through the coherent feedback effect mediated by the cavity mode through the dispersive interaction and the cavity drive and dissipation. Meanwhile, the cavity is also subject to input noise and thus experiences fluctuation. The light-induced noise on the spin can also be understood as the backaction that necessarily accompanies an optical measurement of the spin state. Dissipation of the cavity mode — the effect of coupling it to the outside world through the mirrors — is responsible for the input noise, a necessary consequence of the measurement of the cavity by the environment. Similarly, measurement of the spin by the environment through the cavity is tied to the fluctuation of the spin. The combined effects of optodynamical damping and heating due to backaction cause the collective spin to eventually reach a steady state (in the absence of other effects, of which we will later consider scattering).

The relation between coherent feedback and so-called "quantum nondemolition" (QND) measurements has been explored previously in optomechanics, where in a minimally perturbed QND measurement configuration a cavity can cause mechanical squeezing by acting as a squeezed reservoir, under certain specific driving conditions [144].

4.1.1 Analysis roadmap

In this section I will derive expressions for the time-dependent statistics of the spin distribution. I will find that the cavity–spin interaction damps the mean spin to a longitudinal projection selected by the cavity drive laser frequency, and further that the same interaction damps fluctuation of the longitudinal spin, leading (for some parameter choices) to a reduction in the state's variance compared to that of a coherent spin state, including in the steady-state; meanwhile the interaction and backaction cause diffusion of the transverse spin, increasing the variance of the transverse spin distribution. Considering both components, I show that the spin distribution can be unconditionally squeezed by the cavity–spin inter-

action examined here; further, knowledge of the cavity field dynamics via a measurement record of the output light leads to steady-state conditional squeezing beyond the optimal unconditional squeezing.

I will begin with the Hamiltonian derived in Eq. (3.14) and restated here for reference:

$$\hat{H} = \omega_{\rm s}\hat{F}_z - (\hat{\Delta}_z + g_x\hat{F}_x)\hat{n}, \tag{4.2}$$

having set $\hbar = 1$. The remaining derivation still involves quite a few steps, which I have outlined here:

1. Motivating digression into rate equations (Sec. 4.2.1)
2. Heisenberg–Langevin equations of motion in Lindblad form (Sec. 4.3)
3. Solve for an approximate expression for the optical field (Sec. 4.3.1)
4. Derive effective equations of motion for spin (Sec. 4.3.2)
5. Formal solution of the equations of motion (Sec. 4.4)
6. Analysis of the unconditional squeezing parameter (Sec. 4.6.1)
7. Analysis of the conditional squeezing parameter (Sec. 4.6.2)

For concreteness I choose an example set of "fiducial" experimental parameters listed in Table 4.1. The composite parameters defined throughout the text are listed in Table 4.2 with their values derived from the chosen experimental parameters. Along the way I will utilize various approximations that limit the analysis validity to certain parameter limits. In Table 4.3 I present a mostly complete list of these along with their values for the example parameters to facilitate comparison of the various criteria. Somewhat inconsistently, I occasionally refer to them explicitly in the text like this: (Asm. 1 in Table 4.3).

I approach this problem in three related ways. One is an analytical treatment of the dynamics, detailed in Sec. 4.3 and onwards. The other two are as follows: a rate equation approach, where I calculate the rates at which the system would transition between neighboring Zeeman sublevels and solve for the steady-state under the condition of detailed balance; and a numerical approach in which I solve for the steady-state of the Lindblad equation.

4.2 Steady-state spin distribution

4.2.1 Rate equations and detailed balance

Consider the $2F + 1$ Zeeman levels $|m\rangle \equiv |F, m\rangle$ of the collective spin F in an externally applied magnetic field along the $\boldsymbol{z}$ axis. We can hope to describe a steady state achieved by the collective spin as one in which there is detailed balance among for rate equations of population transfer among the sublevels. The population transfer rates are determined by

the quantum fluctuations of the cavity photon number at the Larmor frequency $\omega_{\rm s}$. These fluctuations are quantified by the intra-cavity photon shot-noise spectrum

$$S^m_{nn}(\omega) = \frac{2\kappa}{\kappa^2 + (-\Delta - m g_z + \omega)^2}\bar{n}, \tag{4.3}$$

which is spin-state dependent because of the vector dispersive shift on the cavity.

The interaction term of the Hamiltonian is

$$\hat{H}_I \approx -\hbar\frac{g_x}{2}\,\hat{c}^\dagger\hat{c}\,(\hat{F}_+ + \hat{F}_-). \tag{4.4}$$

The transition rate $\Gamma_\uparrow$ from state $|m\rangle \to |m+1\rangle$ is

$$\Gamma_\uparrow = P_m\frac{g_x^2}{4}\left|\langle m+1|\hat{F}_+|m\rangle\right|^2 S^m_{nn}(-\omega_{\rm s}), \tag{4.5}$$

in terms of the population P_m in state $|m\rangle$. Similarly, the reverse process occurs at rate

$$\Gamma_\downarrow = P_{m+1}\frac{g_x^2}{4}\left|\langle m|\hat{F}_-|m+1\rangle\right|^2 S^{m+1}_{nn}(+\omega_{\rm s}). \tag{4.6}$$

The matrix elements are $\langle m\pm1|\hat{F}_\pm|m\rangle = \sqrt{F(F+1) - m(m\pm1)}$. Detailed balance requires $\Gamma_\uparrow = \Gamma_\downarrow$, which leads to the population ratio

$$\begin{aligned}\frac{P_{m+1}}{P_m} &= \frac{S^m_{nn}(-\omega_{\rm s})}{S^{m+1}_{nn}(+\omega_{\rm s})} \\ &= \frac{\kappa^2 + (\omega_{\rm s} - (1+m)g_z)^2}{\kappa^2 + (\omega_{\rm s} + m g_z)^2},\end{aligned} \tag{4.7}$$

assuming that there are no other processes that transfer population among the sublevels.

We then find the relative sublevel populations by the products of successive ratios, and normalize to the absolute sublevel populations by additionally invoking the normalization condition $\sum_m P_m = 1$.

$$\frac{P_j}{P_i} = \frac{S^i_{nn}(-\omega_{\rm s})}{S^{i+1}_{nn}(+\omega_{\rm s})} \times \frac{S^{i+1}_{nn}(-\omega_{\rm s})}{S^{i+2}_{nn}(+\omega_{\rm s})} \times \cdots \times \frac{S^{j-1}_{nn}(-\omega_{\rm s})}{S^{j}_{nn}(+\omega_{\rm s})}. \tag{4.8}$$

The recurrence relation determines the entire population distribution. To quantify the distribution, I assume $g_{\rm s} \ll \kappa$ and find in terms of m that

$$\begin{aligned}\frac{P_{m+1}}{P_{m-1}} &= \frac{S^{m+1}_{nn}(-\omega_{\rm s})}{S^{m}_{nn}(+\omega_{\rm s})} \times \frac{S^{m}_{nn}(-\omega_{\rm s})}{S^{m-1}_{nn}(+\omega_{\rm s})} \\ &\approx 1 - \frac{8m\, g_z\omega_{\rm s}}{\kappa^2 + \omega_{\rm s}^2}\end{aligned} \tag{4.9}$$

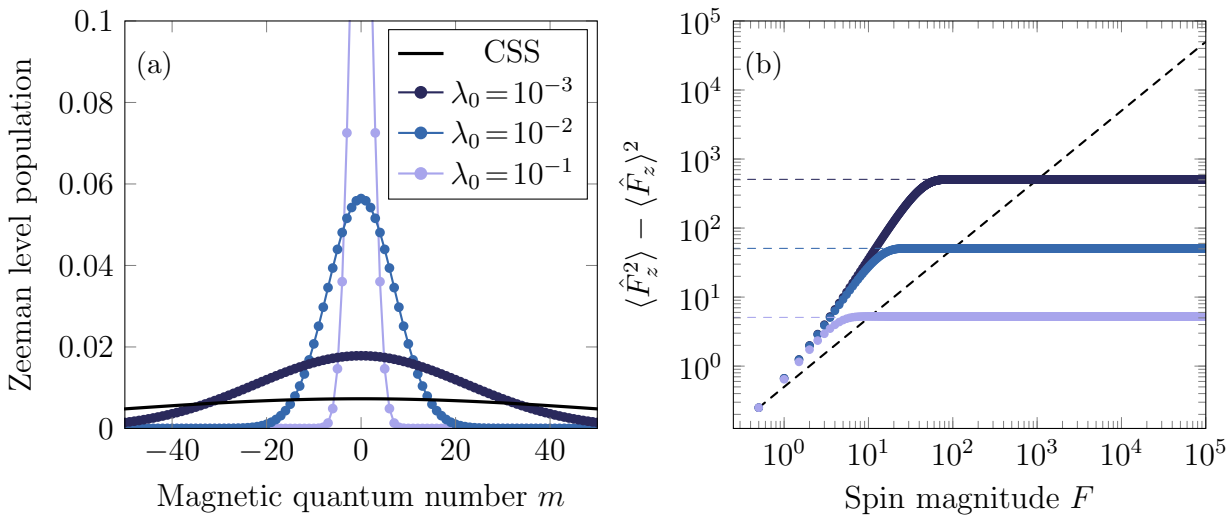


Figure 4.1: (a) The population distribution of a coherent spin state (CSS) at the Bloch sphere equator and steady-state population distributions of the rate equations Eqs. (4.5) and (4.6) for $\Delta = 0$ and several values of λ and $\chi = 1°$. The spin magnitude is $F = 6{,}000$. The variance of each distribution is given by Eq. (4.12). The distributions are discrete; the lines are visualization guides. (b) The variance of the steady-state distributions in (a) shown for varying spin magnitude F. The steady-state variances asymptote to $1/2\lambda_0$ at large F.

is the ratio of populations spaced by $\Delta m = 2$ (chosen so that the resulting expressions are symmetric around a given choice of m). Consider in comparison the ratio of two Gaussian functions of m with relative displacement $\Delta m = 2$ and variance $\langle \hat{F}_z^2 \rangle$:

$$\begin{aligned} \frac{\mathcal{N}(m+1, \langle \hat{F}_z^2 \rangle)}{\mathcal{N}(m-1, \langle \hat{F}_z^2 \rangle)} &= \exp\left(-\frac{(m+1)^2}{2\langle \hat{F}_z^2 \rangle}\right) \exp\left(+\frac{(m-1)^2}{2\langle \hat{F}_z^2 \rangle}\right) \\ &= \exp\left(-\frac{2m}{\langle \hat{F}_z^2 \rangle}\right) \\ &\approx 1 - \frac{2m}{\langle \hat{F}_z^2 \rangle} \end{aligned} \tag{4.10}$$

For a large spin near the equator we assume $F^2 \gg \langle \hat{F}_z^2 \rangle$ (Asm. 2 in Table 4.3). Eqs. (4.9) and (4.10) imply a Gaussian population distribution[2] with variance

$$\langle \hat{F}_z^2 \rangle \approx \frac{\kappa}{4|g_z|} \frac{\kappa^2 + \omega_s^2}{\kappa \omega_s} \equiv \frac{1}{2\lambda}, \tag{4.11}$$

[2]For a small spin $F \not\gg 1$, or a large spin near a pole of the Bloch sphere $F^2 \not\gg \langle \hat{F}_z^2 \rangle$, the Gaussian distribution does not "fit" within the Zeeman subspace and will partially accumulate at one or both poles.

for dimensionless parameter $\lambda \equiv 2|g_z|\omega_\mathrm{s}/(\kappa^2 + {\omega_\mathrm{s}}^2)$ and is only valid[3] for $\lambda < 1$.

The variance is minimized for $\omega_\mathrm{s} = \kappa$, with minimum value

$$\langle \hat{F}_z^2 \rangle_\mathrm{min} = \frac{\kappa}{2|g_z|} \equiv \frac{1}{2\lambda_0}, \tag{4.12}$$

defining dimensionless parameter $\lambda_0 \equiv |g_z|/\kappa$, again limited to the case $\lambda_0 < 1$.

The variance of a coherent spin state in a direction orthogonal to the mean spin vector $\langle \hat{\boldsymbol{F}} \rangle$ is $F/2$, so the steady-state perpendicular variance derived here is smaller than that for a coherent state for $\lambda F > 1$. This is visualized in Fig. 4.1. Explicitly, the ratio of this steady-state variance to the variance of a coherent spin state along the equator is

$$\frac{\langle \hat{F}_z^2 \rangle_\mathrm{min}}{\langle \hat{F}_z^2 \rangle_\mathrm{CSS}} = \frac{\kappa}{F|g_z|} = \frac{1}{\lambda_0 F}. \tag{4.13}$$

Variance reduction is necessary, but not sufficient, to indicate squeezing of $\hat{F}_z$; in the time that it takes the distribution to narrow along the z direction, the precession in the x–y plane could have completely dephased. But this simple rate equation analysis has offered a hint that the system may exhibit interesting statistics, and motivates the more complete analysis that follows.

4.2.2 Numerical steady-state solution of the Lindblad equation

The Lindblad equation for the system density operator $\hat{\rho}$, including cavity dissipation $\hat{c}$, is

$$\dot{\hat{\rho}} = -\frac{\imath}{\hbar}\left[\hat{H}, \hat{\rho}\right] + \kappa\left(\hat{c}\hat{\rho}\hat{c}^\dagger - \frac{1}{2}\left(\hat{c}^\dagger\hat{c}\hat{\rho} + \hat{\rho}\hat{c}^\dagger\hat{c}\right)\right) \tag{4.14}$$

We construct the Liouvillian $\mathcal{L}$ where $\dot{\hat{\rho}} = \mathcal{L}(\hat{\rho})$ and solve for the steady-state density matrix $\lim_{t\to\infty}\hat{\rho}$ that satisfies

$$\mathcal{L}(\hat{\rho}) = 0. \tag{4.15}$$

Using the `qutip` package in Python I calculate the steady state numerically, from which I evaluate the steady-state population distribution and $\lim_{t\to\infty}\langle \hat{F}_z^2 \rangle$.

For steady-state calculations I make the driving strength small to correspond to $\bar{n} \ll 1$ so that I may truncate the Fock-state basis to only a few levels. For the larger spin sizes I use only a two-dimensional Fock-state basis. The spin is handled by a collective spin basis. The results are shown in Fig. 4.2 and agree with the result from the prior section, up to a small numerical factor difference.

[3]Consideration of the case $\lambda_0, \lambda > 1$ is beyond the scope of this work. In such a case one may expect complicated nonlinear dynamics because the vector dispersive shift of the cavity is not small compared to κ, meaning that flipping one individual atomic spin shifts the cavity by $\sim \kappa$.

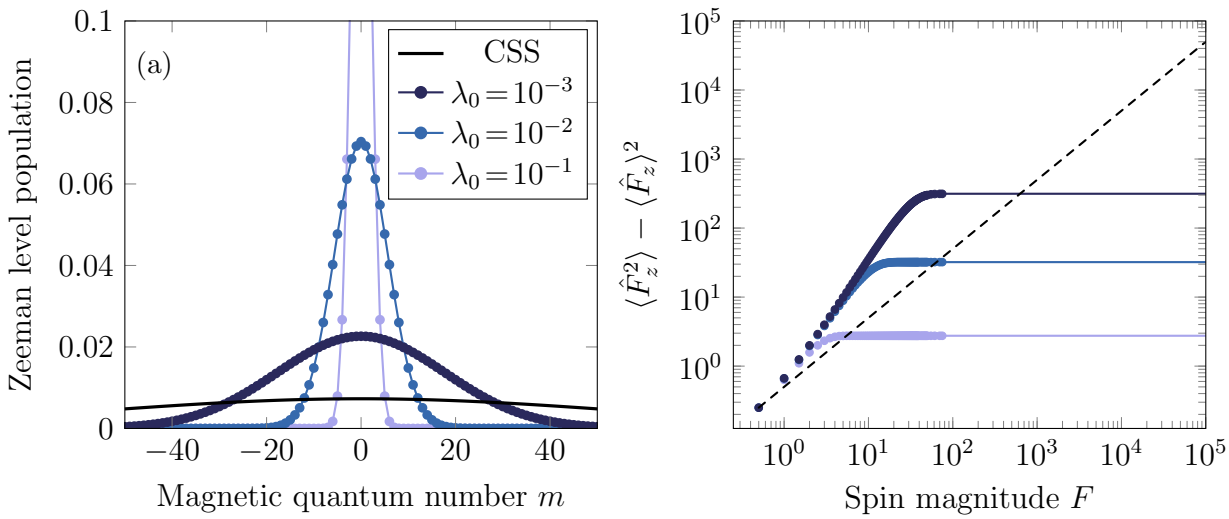


Figure 4.2: (a) The population distribution of a coherent spin state (CSS) at the Bloch sphere equator and steady-state population distributions for $\Delta = 0$ calculated by numerical solution of the Lindblad steady state as in Eq. (4.15) for several values of λ_0 and $\chi = 1°$. The spin magnitude is $F = 6{,}000$. (b) The variance of the steady-state distributions in (a) shown for varying spin magnitude F. The values for spin $F > 75$ are extrapolated from the asymptotic behavior determined from smaller spins.

4.3 Cavity–spin Heisenberg–Langevin equations

For clarity I will restate the spin optodynamical Hamiltonian Eq. (3.14) discussed earlier. Setting $\hbar = 1$, the Hamiltonian is

$$\hat{H} = \omega_s \hat{F}_z - (\hat{\Delta}_z + g_x \hat{F}_x)\hat{n} \tag{4.16}$$

where again $\hat{\Delta}_z \equiv \Delta + g_z \hat{F}_z$, and the coupling strengths are $g_x \equiv g_s \sin\chi$ and $g_z \equiv g_s \cos\chi$.

I begin this analysis by writing down Heisenberg equations of motion from the Hamiltonian. In doing so I will now also include terms describing the external coupling, namely the cavity drive strength η, the Lindblad input noise operator $\hat{\xi}$ describing the vacuum noise coupled into the cavity, and the cavity field decay rate κ. The resulting equations are

$$\begin{aligned}
\dot{\hat{F}}_x &= -\omega_s \hat{F}_y + g_z \hat{n} \hat{F}_y \\
\dot{\hat{F}}_y &= \omega_s \hat{F}_x - \hat{n}(g_z \hat{F}_x - g_x \hat{F}_z) \\
\dot{\hat{F}}_z &= -g_x \hat{n} \hat{F}_y \\
\dot{\hat{c}} &= \imath \hat{\Delta}_z \hat{c} + \imath g_x \hat{F}_x \hat{c} + \eta - \kappa \hat{c} + \sqrt{2\kappa}\hat{\xi},
\end{aligned} \tag{4.17}$$

The evolutions of the spin components depend on the torques from the external magnetic field and the effective magnetic field of the cavity mode. The cavity field accumulates phase depending on the detuning, is driven by a coherent input η and input noise $\hat{\xi}$, and decays at rate κ. The input noise is defined such that $\langle\hat{\xi}(t)\rangle = 0$ and $\langle\hat{\xi}(t)\hat{\xi}^\dagger(t')\rangle = \delta(t-t')$.

We can also use these equations in an alternative, equivalent form, written instead in terms of the spin raising and lowering operators:

$$\begin{aligned}\dot{\hat{F}}_\pm &= \pm\imath(\omega_\mathrm{s} - g_z\hat{n})\hat{F}_\pm \pm g_x\hat{n}\hat{F}_z \\ \dot{\hat{F}}_z &= \tfrac{\imath}{2}g_x\hat{n}(\hat{F}_+ - \hat{F}_-) \\ \dot{\hat{c}} &= \imath\hat{\Delta}_z\hat{c} + \tfrac{\imath}{2}g_x(\hat{F}_+ + \hat{F}_-)\hat{c} + \eta - \kappa\hat{c} + \sqrt{2\kappa}\hat{\xi}\end{aligned} \tag{4.18}$$

The classical drive will lead to a mean displacement of $\hat{c}$, while we will be most interested in the fluctuation of $\hat{c}$ around its mean value, where we choose the phase of the classical drive such that the mean value is real. We write $\hat{c} = \bar{c} + \hat{b}$, where $\bar{c} = \sqrt{\bar{n}}$ is the mean value and $\hat{b}$ is the fluctuation around the mean. The cavity photon number operator is then $\hat{n} = \hat{c}^\dagger\hat{c} = \bar{n} + \sqrt{\bar{n}}(\hat{b}^\dagger + \hat{b}) + \hat{b}^\dagger\hat{b}$. The mean photon number will lead to a (small, for $g_\mathrm{s}\bar{n} \ll \omega_\mathrm{s}$) reconfiguration of the average magnetic field, and introduces the effective Larmor frequency $\omega_\mathrm{s}' = \omega_\mathrm{s} + g_z\bar{n}$ which we absorb into ω_s. We will drop the second-order fluctuation term $\hat{b}^\dagger\hat{b}$, assuming it is small relative to the terms that scale with $\bar{n}$ and $\sqrt{\bar{n}}$. Then we can replace $\hat{n} \simeq \bar{n} + \sqrt{\bar{n}}(\hat{b}^\dagger + \hat{b})$ in the equations of motion which leads to

$$\begin{aligned}\dot{\hat{F}}_\pm &= \pm\imath\big(\omega_\mathrm{s} - g_z\sqrt{2\bar{n}}\,\hat{b}^\mathrm{AM}\big)\hat{F}_\pm \pm g_x\sqrt{2\bar{n}}\hat{b}^\mathrm{AM}\hat{F}_z \\ \dot{\hat{F}}_z &= \tfrac{\imath}{2}g_x\sqrt{2\bar{n}}\,\hat{b}^\mathrm{AM}(\hat{F}_+ - \hat{F}_-) \\ \dot{\hat{b}} &= \imath\hat{\Delta}_z\hat{b} + \tfrac{\imath}{2}g_x(\hat{F}_+ + \hat{F}_-)\hat{b} - \kappa\hat{b} + \sqrt{2\kappa}\hat{\xi},\end{aligned} \tag{4.19}$$

where I have dropped terms[4] that scale with only the classical portion $\bar{n}$ of $\hat{n}$.

4.3.1 Solution for the cavity field

In order to reduce the dynamical system to just the spin sector, eliminating the cavity field, we want an explicit expression for the cavity field to then substitute into the equations of motion for the spin operators. This is tricky because of the time-dependence of $\hat{F}_z$, so we restrict our analysis to the condition that $\hat{F}_z$ varies slowly compared to the rate κ. This condition has two parts[5] because the dynamics of $\hat{F}_z$ exhibit multiple phenomena:

1. small oscillations on fast timescale ω_s, and

2. average nutation of the spin at a rate that I will call Γ_z, to be discussed in detail later.

[4]One such term leads to an average shift in the Larmor frequency, so that the effective precession frequency is actually $\omega_\mathrm{s}' \equiv \omega_\mathrm{s} - g_z\bar{n}$. This shift is small for $g_z\bar{n} \ll \omega_\mathrm{s}$ so I absorb this into ω_s going forward.

[5]We might additionally want to require slowness of the diffusion of the longitudinal spin. We will see that this is satisfied as it is also much slower than κ.

We can neglect the second phenomena in deriving an effective expression for the cavity field by the assumption $\Gamma_z \ll \kappa$, which can be verified later when I derive an explicit expression for Γ_z. The first one leads to higher-order sidebands in the cavity field spectrum. We will neglect these under the assumption of small modulation depth $F|g_x| \ll \kappa$, and the related assumption of small vector dispersive shift oscillation[6] $Fg_x^2 g_z \bar{n}/\kappa^2 \omega_{\rm s} \ll 1$ and consider $\hat{\Delta}_z$ as slowly varying compared to the fast timescale κ.

It would not be sufficient for our purposes to solve for the cavity field in terms of expectation values of the spin operators, because that would preclude the possibility of conditional feedback, where the cavity has partially measured the spin and acts back on it conditioned on its measured value. In what follows we identify the spin operators with their conditional values as sampled by the cavity [145–148].

With this understanding, I solve Eqs. (4.17) for $\hat{c}(t)$ as follows.

$$\begin{aligned}
\hat{c}(t) &= \exp\left(-\int_0^t dt_1 \left[-\imath\big(g_x\hat{F}_x(t_1) + \hat{\Delta}_z(t_1)\big) + \kappa\right]\right) \\
&\quad \times \left(\hat{c}(0) + \int_0^t dt_1 \exp\left(\int_0^{t_1} dt_2 \left[-\frac{\imath}{2}\left(g_x\big(\hat{F}_+(t_2) + \hat{F}_-(t_2)\big) + \hat{\Delta}_z(t_2)\right) + \kappa\right]\right)\right. \\
&\qquad\qquad \left.\times \left[\eta + \sqrt{2\kappa}\,\hat{\xi}(t_1)\right]\right) \qquad (4.20) \\
&\simeq \exp\left(-\int_0^t dt_1 \left[-\frac{\imath}{2}\left(g_x\big(e^{\imath\omega_{\rm s}t_1}\hat{F}_+(0) + e^{-\imath\omega_{\rm s}t_1}\hat{F}_-(0)\big) + \hat{\Delta}_z(0)\right) + \kappa\right]\right) \\
&\quad \times \left(\hat{c}(0) + \int_0^t dt_1 \exp\left(\int_0^{t_1} dt_2 \left[-\frac{\imath}{2}\left(g_x\big(e^{\imath\omega_{\rm s}t_2}\hat{F}_+(0) + e^{-\imath\omega_{\rm s}t_2}\hat{F}_-(0)\big) + \hat{\Delta}_z(0)\right) + \kappa\right]\right)\right. \\
&\qquad\qquad \left.\times \left[\eta + \sqrt{2\kappa}\,\hat{\xi}(t_1)\right]\right).
\end{aligned}$$

We assume $Fg_x \ll \kappa, \omega_{\rm s}$, which we interpret as a condition of small modulation depth (that the precessing spin modulates the cavity by less than the cavity linewidth) and that the

[6] On a timescale $1/\omega_{\rm s}$, fast oscillation of $\hat{F}_z$ changes its value by approximately $\sim Fg_x^2\bar{n}/\kappa\omega_{\rm s}$. This leads to a vector dispersive shift modulation which for simplicity should be much less than the cavity linewidth; its amplitude is that of the fast $\hat{F}_z$ oscillations multiplied by g_z.

extent of the dynamic reorientation of the total magnetic field is small.

$$\begin{aligned}\hat{c}(t) &= \exp\left(\frac{-g_x}{2\omega_\mathrm{s}}\left[(1-e^{\imath\omega_\mathrm{s}t})\hat{F}_+(0)-(1-e^{-\imath\omega_\mathrm{s}t})\hat{F}_-(0)\right]-\big(\kappa-\imath\hat{\Delta}_z(0)\big)t\right)\\ &\quad\times\left(\hat{c}(0)+\int_0^t dt_1\,\exp\left(\frac{g_x}{2\omega_\mathrm{s}}\left[\big(1-e^{\imath\omega_\mathrm{s}t_1}\big)\hat{F}_+(0)-\big(1-e^{-\imath\omega_\mathrm{s}t_1}\big)\hat{F}_-(0)\right]+\big(\kappa-\imath\hat{\Delta}_z(0)\big)t_1\right)\right.\\ &\qquad\left.\times\left[\eta+\sqrt{2\kappa}\,\hat{\xi}(t_1)\right]\right)\\ &\simeq\left(1-\frac{g_x}{2\omega_\mathrm{s}}\left[(1-e^{\imath\omega_\mathrm{s}t})\hat{F}_+(0)-(1-e^{-\imath\omega_\mathrm{s}t})\hat{F}_-(0)\right]\right)e^{-\left(\kappa-\imath\hat{\Delta}_z(0)\right)t}\\ &\quad\times\left(\hat{c}(0)+\int_0^t dt_1\,\left(1+\frac{g_x}{2\omega_\mathrm{s}}\left[\big(1-e^{\imath\omega_\mathrm{s}t_1}\big)\hat{F}_+(0)-\big(1-e^{-\imath\omega_\mathrm{s}t_1}\big)\hat{F}_-(0)\right]\right)e^{\left(\kappa-\imath\hat{\Delta}_z(0)\right)t_1}\right.\\ &\qquad\left.\times\left[\eta+\sqrt{2\kappa}\,\hat{\xi}(t_1)\right]\right),\end{aligned}\tag{4.21}$$

Assuming initial transients have decayed ($t \gg 1/\kappa$), we can now fully evaluate the coherent portion of the cavity field in terms of the spin ladder operators; they carry complex coefficients describing the cavity susceptibility at the relative frequencies $\pm\omega_\mathrm{s}$ of the blue and red sidebands. We let $\eta \to \sqrt{\bar{n}}/\kappa$ and switch to $\hat{b} \equiv \hat{c} - \sqrt{\bar{n}}$ to handle the mean displacement.

$$\begin{aligned}\hat{b}(t) &\simeq \frac{\imath g_x\sqrt{\bar{n}}}{2}\left(\left[\kappa+\imath\big(-\hat{\Delta}_z(t)+\omega_\mathrm{s}\big)\right]^{-1}\hat{F}_+(t)+\left[\kappa+\imath\big(-\hat{\Delta}_z(t)-\omega_\mathrm{s}\big)\right]^{-1}\hat{F}_-(t)\right)\\ &\quad+\sqrt{2\kappa}\left(1-\frac{g_x}{2\omega_\mathrm{s}}\left[(1-e^{\imath\omega_\mathrm{s}t})\hat{F}_+(0)-(1-e^{-\imath\omega_\mathrm{s}t})\hat{F}_-(0)\right]\right)e^{-\left(\kappa-\imath\hat{\Delta}_z(0)\right)t}\\ &\qquad\times\int_0^t dt_1\,\left(1+\frac{g_x}{2\omega_\mathrm{s}}\left[\big(1-e^{\imath\omega_\mathrm{s}t_1}\big)\hat{F}_+(0)-\big(1-e^{-\imath\omega_\mathrm{s}t_1}\big)\hat{F}_-(0)\right]\right)\\ &\qquad\qquad\times e^{\left(\kappa-\imath\hat{\Delta}_z(0)\right)t_1}\hat{\xi}(t_1)\\ &\simeq\frac{\imath g_x\sqrt{\bar{n}}}{2}\left(\left[\kappa+\imath\big(-\hat{\Delta}_z(t)+\omega_\mathrm{s}\big)\right]^{-1}\hat{F}_+(t)+\left[\kappa+\imath\big(-\hat{\Delta}_z(t)-\omega_\mathrm{s}\big)\right]^{-1}\hat{F}_-(t)\right)\\ &\quad+\sqrt{2\kappa}\int_0^t dt_1\,e^{-(\kappa-\imath\hat{\Delta}_z(0))(t-t_1)}\\ &\qquad\times\left(1+\frac{g_x}{2\omega_\mathrm{s}}\left[(e^{\imath\omega_\mathrm{s}t}-e^{\imath\omega_\mathrm{s}t_1})\hat{F}_+-(e^{-\imath\omega_\mathrm{s}t}-e^{-\imath\omega_\mathrm{s}t_1})\hat{F}_-\right]\right)\hat{\xi}(t_1),\end{aligned}\tag{4.22}$$

and finally we find the cavity field to be

$$\hat{b}(t)=\frac{\imath g_x\sqrt{\bar{n}}}{2}\left(\left[\kappa+\imath\big(-\hat{\Delta}_z(t)+\omega_\mathrm{s}\big)\right]^{-1}\hat{F}_+(t)+\left[\kappa+\imath\big(-\hat{\Delta}_z(t)-\omega_\mathrm{s}\big)\right]^{-1}\hat{F}_-(t)\right)+\sqrt{\frac{2}{\kappa}}\hat{\xi}_\Delta(t).\tag{4.23}$$

We have defined the intra-cavity shot noise fluctuations as

$$\hat{\xi}_{\Delta}(t) = \int_0^t dt_1\, e^{-(\kappa - \imath\hat{\Delta}_z)(t-t_1)} \left(1 + \frac{g_x}{2\omega_{\rm s}}\left[(e^{\imath\omega_{\rm s}t} - e^{\imath\omega_{\rm s}t_1})\hat{F}_+ - (e^{-\imath\omega_{\rm s}t} - e^{-\imath\omega_{\rm s}t_1})\hat{F}_-\right]\right)\hat{\xi}(t_1). \tag{4.24}$$

to first order in $g_x/\omega_{\rm s}$. As a rough approximation we drop the term $\propto g_x/\omega_{\rm s}$, in which case the cavity noise reduces to

$$\begin{aligned}\hat{\xi}_{\Delta}(t) &\simeq \kappa \int_0^t dt_1 \exp\Big(-(\kappa - \imath\hat{\Delta}_z)(t-t_1)\Big)\,\hat{\xi}(t_1) \\ &\simeq \kappa \int_{-\infty}^t dt_1\, \exp\Big(-(\kappa - \imath\hat{\Delta}_z)(t-t_1)\Big)\,\hat{\xi}(t_1),\end{aligned} \tag{4.25}$$

assuming the initial transients have decayed. This has two-time correlation function

$$\Big\langle \hat{\xi}_{\Delta}(t)\,\hat{\xi}^{\dagger}_{\Delta}(t')\Big\rangle = \Big[\hat{\xi}_{\Delta}(t), \hat{\xi}^{\dagger}_{\Delta}(t')\Big] = \frac{\kappa}{2}\exp\Big(\imath\hat{\Delta}_z(t-t') - \kappa|t-t'|\Big). \tag{4.26}$$

The cavity quadratures are

$$\begin{aligned}\hat{b}^{\rm AM}(t) &= \frac{\hat{b}^{\dagger}(t) + \hat{b}(t)}{\sqrt{2}} = \frac{g_x\sqrt{\bar{n}/2}}{2}\Big(\mathrm{Re}[\alpha](\hat{F}_+ + \hat{F}_-) + \imath\,\mathrm{Im}[\alpha](\hat{F}_+ - \hat{F}_-)\Big) + \sqrt{\frac{2}{\kappa}}\hat{\xi}^{\rm AM}_{\Delta}(t) \\ \hat{b}^{\rm PM}(t) &= \frac{\hat{b}^{\dagger}(t) - \hat{b}(t)}{\sqrt{2}} = \frac{g_x\sqrt{\bar{n}/2}}{2}\Big(\mathrm{Re}[\beta](\hat{F}_+ + \hat{F}_-) + \imath\,\mathrm{Im}[\beta](\hat{F}_+ - \hat{F}_-)\Big) + \sqrt{\frac{2}{\kappa}}\hat{\xi}^{\rm PM}_{\Delta}(t),\end{aligned} \tag{4.27}$$

in terms of the coefficients

$$\alpha \equiv \frac{-2\hat{\Delta}_z}{\hat{\Delta}_z^2 + (\kappa + \imath\omega_{\rm s})^2} \qquad \text{and} \qquad \beta \equiv \frac{2(\kappa + \imath\omega_{\rm s})}{\hat{\Delta}_z^2 + (\kappa + \imath\omega_{\rm s})^2}. \tag{4.28}$$

The AM quadrature of the filtered noise has two-time correlation function

$$\Big\langle \hat{\xi}^{\rm AM}_{\Delta}(t)\,\hat{\xi}^{\rm AM}_{\Delta}(t')\Big\rangle = \frac{\kappa}{2}\cos\big(\hat{\Delta}_z[t-t']\big)e^{-\kappa|t-t'|} \tag{4.29}$$

and two-time commutator

$$\Big[\hat{\xi}^{\rm AM}_{\Delta}(t), \hat{\xi}^{\rm AM}_{\Delta}(t')\Big] = \frac{\imath\kappa}{2}\sin\big(\hat{\Delta}_z[t-t']\big)\exp\big(-\kappa|t-t'|\big). \tag{4.30}$$

Examining $\hat{\Delta}_z$, we note that $\hat{\Delta}_z/g_z = (\Delta/g_z) + \hat{F}_z$, which depends on the experimentally imposed Δ and $\hat{F}_z$ with a proportionality constant of g_z. We will see that the $\hat{F}_z$ dynamics exhibit damping, so we will think of $\hat{\Delta}_z$ as an "error signal" between the "setpoint" $g_z\hat{F}_{z,\rm set} = \Delta$ and the "measurement" $-g_z\hat{F}_z$. We choose the setpoint to be at the equator of the

collective Bloch sphere, setting $\Delta = 0$, and focusing our attention on spin states near the equator where $\langle \hat{F}_z \rangle = 0$.

(Asms. 2, 7): Following this reasoning we will assume that $|\hat{\Delta}_z|/\kappa$ is small, and that $\hat{F}_z^2 \ll F(F+1)$. We expand the coefficient α for $|\hat{\Delta}_z| \ll \kappa$, finding

$$\hat{\Delta}_z \ll \kappa \qquad \mathrm{Re}[\alpha] \longrightarrow \frac{-2(\kappa^2-\omega^2)}{(\kappa^2+\omega^2)^2}\hat{\Delta}_z \qquad \mathrm{Im}[\alpha] \longrightarrow \frac{4\kappa\omega}{(\kappa^2+\omega^2)^2}\hat{\Delta}_z. \tag{4.31}$$

which simplifies the form of the cavity field. Likewise, the AM cavity noise correlation function reduces to

$$\left\langle \hat{\xi}_\Delta^{\mathrm{AM}}(t)\, \hat{\xi}_\Delta^{\mathrm{AM}}(t') \right\rangle \simeq \frac{\kappa}{2} \exp\bigl(-\kappa|t-t'|\bigr), \tag{4.32}$$

while for the two-time commutator we have

$$\left[\hat{\xi}_\Delta^{\mathrm{AM}}(t)\, \hat{\xi}_\Delta^{\mathrm{AM}}(t') \right] \to 0. \tag{4.33}$$

4.3.2 Deriving the reduced spin equations of motion

We have solved for the effective cavity field in terms of the spin operators. Noting $\hat{c}^{\mathrm{AM}}(t) = \sqrt{2\bar{n}} + \hat{b}^{\mathrm{AM}}(t)$, we substitute into the equations of motion Eqs. (4.18). By dropping fast-oscillating terms and assuming $F \gg 1$ and $\hat{F}_z^2 \ll F^2$, we find[7]

$$\begin{aligned}
\dot{\hat{F}}_\pm &\simeq \pm\imath \left(\omega_{\mathrm{s}} + \bar{n} g_x^2 g_z \frac{\kappa^2 - {\omega_{\mathrm{s}}}^2}{(\kappa^2+{\omega_{\mathrm{s}}}^2)^2} \hat{F}_z(\hat{F}_z \mp 1) + 2g_z \sqrt{\frac{\bar{n}}{\kappa}} \hat{\xi}_\Delta^{\mathrm{AM}} \right) \hat{F}_\pm \\
\dot{\hat{F}}_z &\simeq 2\bar{n} g_x^2 g_z \frac{\kappa\omega_{\mathrm{s}}}{(\kappa^2+{\omega_{\mathrm{s}}}^2)^2} \left(F(F+1) - \hat{F}_z^2 \right) \hat{F}_z - \imath g_x \sqrt{\frac{\bar{n}}{\kappa}} \hat{\xi}_\Delta^{\mathrm{AM}}(t)(\hat{F}_- - \hat{F}_+).
\end{aligned} \tag{4.34}$$

which we approximate as

$$\begin{aligned}
\dot{\hat{F}}_\pm &\approx \pm\imath \left(\omega_{\mathrm{s}} + \sigma_\perp \hat{\xi}_\Delta^{\mathrm{AM}} \right) \hat{F}_\pm \\
\dot{\hat{F}}_z &\approx -\Gamma_z \hat{F}_z + \sigma_z\, \hat{\xi}_\Delta^{\mathrm{AM}}(t) \frac{\hat{F}_+ - \hat{F}_-}{2\imath}
\end{aligned} \tag{4.35}$$

[7]There are additional terms that show up here when performing this substitution naïvely. For example, in the equation for $\hat{F}_z$ one would find that the term $\propto \imath\mathrm{Re}[\alpha](\hat{F}_+ + \hat{F}_-)(\hat{F}_+ - \hat{F}_-)$ becomes anti-Hermitian. As $\hat{F}_z$ should remain Hermitian, this seems confusing. We resolve this by noticing that this term will have either a positive or negative sign depending on the relative order of $\hat{c}^{\mathrm{AM}}$ and $\hat{F}_y$ in the equation of motion for $\hat{F}_z$, which itself depends on the relative order of $\hat{n}$ and $\hat{F}$ in the original system Hamiltonian. As these operators commute in the Hamiltonian because they operate on different Hilbert spaces, there is no physical difference between writing $\hat{H} \sim \hat{n}\hat{F}$ and $\hat{H} \sim \hat{F}\hat{n}$. That this choice flips the sign of the anti-Hermitian term indicates that the term is unphysical, and that it comes from improperly keeping track of operator ordering along the way. I use the symmetrized version of the operators.

in terms of the noise amplitudes

$$\begin{aligned}\sigma_\perp &\equiv 2g_z\sqrt{\bar{n}/\kappa},\\ \sigma_z &\equiv -2g_x\sqrt{\bar{n}/\kappa}.\end{aligned} \tag{4.36}$$

and the optodynamical damping rate

$$\begin{aligned}\Gamma_z &\equiv -2\bar{n}g_x^2 g_z F(F+1)\kappa\omega_\mathrm{s}/(\kappa^2+{\omega_\mathrm{s}}^2)^2\\ &\simeq -2\bar{n}g_x^2 g_z F^2\kappa\omega_\mathrm{s}/(\kappa^2+{\omega_\mathrm{s}}^2)^2,\end{aligned} \tag{4.37}$$

or, in terms of a dimensionless linewidth–sideband parameter $\psi \equiv 2\kappa\omega_\mathrm{s}/(\kappa^2+\omega_\mathrm{s}^2)$,

$$\Gamma_z = -\tfrac{1}{2}\bar{n}F^2\frac{g_x^2 g_z}{\kappa\omega_\mathrm{s}}\psi^2. \tag{4.38}$$

The damping rate Γ_z derived here reduces to the damping rate β derived in Refs. [6, 7] in the unresolved-sideband regime, and (if we had not assumed $\Delta_\mathrm{pc} \neq 0$) to the damping rate Γ_opt derived in Ref. [73] for the specific case $\chi = \pi/2$.

Note that $\psi \leq 1$ and it attains its maximum value 1 for $\kappa = \omega_\mathrm{s}$, while Γ_z peak at $\omega_\mathrm{s} = \kappa/\sqrt{3}$. Now that we have an explicit expression for Γ_z we can assess our earlier assumption $\Gamma_z \ll \kappa$. This amounts to $-2\bar{n}g_x^2 g_z F^2\omega_\mathrm{s}/(\kappa^2+{\omega_\mathrm{s}}^2)^2 \ll 1$. For very large collective-coupling strength $g_\mathrm{s}F$, or very large photon numbers at intermediate coupling strength, this assumption may break down.

The evolution equations above show that on short timescales $\sim 1/\omega_\mathrm{s}$ the $\hat{F}_\pm$ operators evolve essentially as $\hat{F}_\pm \sim e^{\pm\imath\omega_\mathrm{s}}\hat{F}_\pm$, while on longer timescales the precession phase diffuses as the precession rate is subject to fluctuation; meanwhile, $\hat{F}_z$ exhibits both fluctuation and damping.

Consider for a moment the sign of the damping rate Γ_z. We can see by inspection that its sign flips under a sign-flip of g_z. The explicit minus sign out front is from our choice of driving polarization that picked $\hat{n}_-$ rather than $\hat{n}_+$, so Γ_z would also flip sign if we switch to the other polarization. Thus the behavior of the sign of Γ_z is consistent with Eq. (3.15). In the language of feedback systems as discussed in Ref. [6, 7], we identity Γ_z with the damping rate or closed-loop gain of the feedback system.

4.3.3 Damping and the atomic scattering rate

Let us recall the scattering rate Eq. 3.21 and compare it to the optodynamical damping rate derived above. If the scattering rate Γ_sc is greater than Γ_z, the spin will decohere before damping, and any interesting dynamics will be circumvented. This suggests that to observe damping, we want to be in the case $|\Gamma_z/\Gamma_\mathrm{sc}| \gg 1$. This ratio is

$$\begin{aligned}\frac{|\Gamma_z|}{\Gamma_\mathrm{sc}} &= \frac{-2\bar{n}g_x^2 g_z F^2\kappa\omega_\mathrm{s}/(\kappa^2+{\omega_\mathrm{s}}^2)^2}{\bar{n}\Gamma_\mathrm{e}g_0^2/\Delta_\mathrm{ca}^2}\\ &= CF^2\frac{g_\mathrm{s}}{\kappa}\frac{\sin^2\chi\cos\chi}{72},\end{aligned} \tag{4.39}$$

where $C = g_0^2/\kappa\Gamma_\mathrm{e}$ is again the cooperativity. I will generally assume that $\Gamma_z \gg \Gamma_\mathrm{sc}$ such that scattering is negligible on the timescale of the damping, but revisit this in Sec. 4.6.3.

4.4 Dynamics of the reduced spin equations

I will now derive solutions to the stochastic equations derived above in Eqs. (4.35). From these solutions I will calculate the variances of the spin distribution for conjugate coordinates. The variance of $\hat{F}_z$ and $\hat{F}_\pm$ will each depend on the integrated cavity-filtered input noise correlation function. To begin with, I write solutions to the stochastic equations of motion derived earlier, and from these calculate the expectation values of several operators that will be used throughout this section.

According to its stochastic equation of motion, the transverse spin components undergo precession and undamped diffusion. Consider a spin initialized in the coherent state described by $\langle\hat{F}_z(0)\rangle = 0$ and $\langle\hat{F}_\pm(0)\rangle = F$. The stochastic equation has the solution

$$\begin{aligned}\hat{F}_\pm(t) &= \exp\left(\pm\imath\left[\omega_\mathrm{s}t + \sigma_\perp\int_0^t dt'\,\hat{\xi}_\Delta^\mathrm{AM}(t')\right]\right)\hat{F}_\pm(0)\\ &= \exp\left(\pm\imath\omega_\mathrm{s}t\right)\exp\left(\imath\sigma_\perp\int_0^t dt'\,\hat{\xi}_\Delta^\mathrm{AM}(t')\right)\hat{F}_\pm(0),\end{aligned} \tag{4.40}$$

while the stochastic equation of motion for the longitudinal spin operator has the solution

$$\hat{F}_z(t) = \exp\left(-\Gamma_z t\right)\hat{F}_z(0) + \sigma_z\int_0^t dt'\,\exp(-\Gamma_z[t-t'])\,\hat{\xi}_\Delta^\mathrm{AM}(t')\frac{\hat{F}_+(t') - \hat{F}_-(t')}{2\imath}. \tag{4.41}$$

We will need the expectation value and the two-time correlation function of the transverse spin in the derivations of the variances, so for clarity I derive them now and refer back to them as needed. The former is

$$\begin{aligned}\left\langle\hat{F}_\pm(t)\right\rangle &= \exp\left(\pm\imath\omega_\mathrm{s}t\right)\left\langle\exp\left(\imath\sigma_\perp\int_0^t dt'\,\hat{\xi}_\Delta^\mathrm{AM}(t')\right)\hat{F}_\pm(0)\right\rangle\\ &\simeq \exp\left(\pm\imath\omega_\mathrm{s}t\right)\left(1 - D_\perp\int_0^t\int_0^t dt'dt''\left\langle\hat{\xi}_\Delta^\mathrm{AM}(t')\hat{\xi}_\Delta^\mathrm{AM}(t'')\right\rangle + \cdots\right)\left\langle\hat{F}_\pm(0)\right\rangle,\end{aligned} \tag{4.42}$$

in terms of powers of the correlation function of the cavity-filtered noise, where odd powers of the series drop out because the expectation value of the noise operator vanishes. We substitute for this and integrate to find

$$\begin{aligned}\left\langle\hat{F}_\pm(t)\right\rangle &= \exp\left(\pm\imath\omega_\mathrm{s}t\right)\left(1 - D_\perp\frac{\kappa}{2}\int_0^t\int_0^t dt'\,dt''\,e^{-\kappa|t'-t''|} + \cdots\right)\left\langle\hat{F}_\pm(0)\right\rangle\\ &= \exp\left(\pm\imath\omega_\mathrm{s}t\right)\left(1 - D_\perp\left(t - \frac{1}{\kappa}\left(1 - e^{-\kappa t}\right)\right) + \cdots\right)\left\langle\hat{F}_\pm(0)\right\rangle\\ &\simeq \exp\big((\pm\imath\omega_\mathrm{s} - D_\perp)t\big)\big\langle\hat{F}_\pm(0)\big\rangle,\end{aligned} \tag{4.43}$$

in terms of the transverse diffusion constant $D_\perp \equiv \sigma_\perp^2/2$. The latter is, for a spin state at the equator with $\langle \hat{F}_z(t)\rangle = 0$,

$$\begin{aligned}\left\langle \hat{F}_\mp(t)\,\hat{F}_\pm(t')\right\rangle &= \left\langle \exp\left(\mp\imath\sigma_\perp\int_0^t dt_1\,\hat{\xi}_\Delta^{\rm AM}(t_1)\right)\exp\left(\pm\imath\sigma_\perp\int_0^{t'} dt_1\,\hat{\xi}_\Delta^{\rm AM}(t_1)\right)\right\rangle \\ &\qquad\times\left\langle \hat{F}_\mp(0)\hat{F}_\pm(0)\right\rangle e^{\mp\imath\omega_{\rm s}(t-t')} \\ &= \left\langle \exp\left(\imath\sigma_\perp\int_t^{t'} dt_1\,\hat{\xi}_\Delta^{\rm AM}(t_1) + \frac{\sigma_\perp^2}{2}\int_0^t\int_0^{t'} dt_1\,dt_2\left[\hat{\xi}_\Delta^{\rm AM}(t_1),\hat{\xi}_\Delta^{\rm AM}(t_2)\right]\right)\right\rangle \\ &\qquad\times F(F+\tfrac{1}{2})\,e^{\mp\imath\omega_{\rm s}(t-t')},\end{aligned} \tag{4.44}$$

by the Baker–Campbell–Hausdorff formula. The commutator vanishes for $|\hat{\Delta}_z| \ll \kappa$, leaving

$$\begin{aligned}\left\langle \hat{F}_\mp(t)\,\hat{F}_\pm(t')\right\rangle &\simeq \left(1+\imath\sigma_\perp\int_t^{t'} dt_1\,\langle\hat{\xi}_\Delta^{\rm AM}(t_1)\rangle - \frac{\sigma_\perp^2}{2}\int_t^{t'}\int_t^{t'} dt_1\,dt_2\left\langle\hat{\xi}_\Delta^{\rm AM}(t_1)\,\hat{\xi}_\Delta^{\rm AM}(t_2)\right\rangle + \cdots\right) \\ &\qquad\times F(F+\tfrac{1}{2})\,e^{\mp\imath\omega_{\rm s}(t-t')} \\ &\simeq F(F+\tfrac{1}{2})\exp\Big(\mp\imath\omega_{\rm s}(t-t') - D_\perp|t-t'|\Big)\end{aligned} \tag{4.45}$$

The two-time transverse spin correlation function is oscillatory in the time difference and has correlation time $1/D_\perp$, which will turn out to be long compared to the dynamics of interest[8].

4.4.1 Variance of the spin transverse to the field axis

The transverse spin variance is $V_\perp(t) \equiv \langle \hat{F}_+(t)\hat{F}_-(t)\rangle - \langle\hat{F}_+(t)\rangle\langle\hat{F}_-(t)\rangle$. The product term is, as calculated above,

$$\begin{aligned}\left\langle \hat{F}_\pm(t)\hat{F}_\mp(t)\right\rangle &= \left\langle \hat{F}^2 - \hat{F}_z(t)^2 \pm \hat{F}_z(t)\right\rangle \\ &= F(F+1) - \langle\hat{F}_z(t)^2\rangle\end{aligned} \tag{4.46}$$

for $\langle\hat{F}_z(t)\rangle = 0$. Note that for a coherent spin state on the equator, this value is $F(F+\frac{1}{2})$, while for the $m=0$ Zeeman sublevel $|F,m=0\rangle$ this value is $F(F+1)$ which we can approximate as $\langle\hat{F}_\pm(t)\hat{F}_\mp(t)\rangle \simeq F^2$ for $F \gg 1$ assuming that $\langle\hat{F}_z(t)^2\rangle$ does not become much larger than its initial (coherent spin state) value $\langle\hat{F}_z(0)^2\rangle = F/2$.

[8]There is a minor effect we neglected: a reduced longitudinal variance slightly increases the transverse variance as $\langle\hat{F}_\pm(t)\hat{F}_\mp(t)\rangle = \langle\hat{F}^2\rangle - \langle\hat{F}_z(t)^2\rangle \pm \langle\hat{F}_z(t)\rangle$. The transverse variance scales as $\sim F^2$. As we will see, the longitudinal variance decays from $F/2$; assuming this, the error here is $\sim F/2 \ll F^2$.

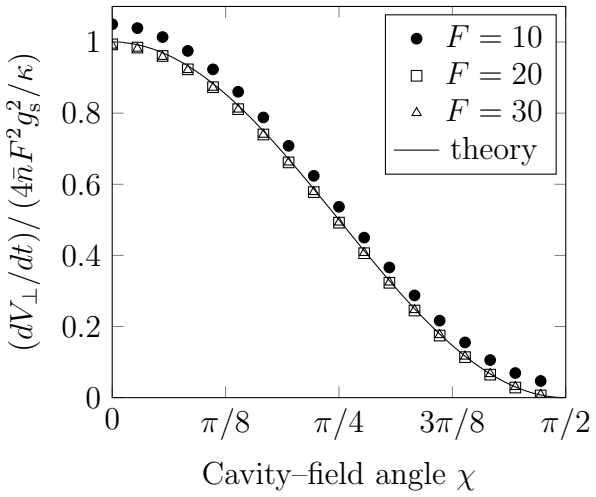


Figure 4.3: Comparison between the analytic expression Eq. (4.47) and the results of numerical solution of the Lindblad equation for several values of the spin magnitude with coupling strength $|g_s|/\kappa = 10^{-3}$. Specifically, I calculate the evolution of the density matrix for a period of time $T \gg 1/\kappa, 1/\omega_s$, and evaluate $\langle \hat{F}_+(t)\hat{F}_-(t)\rangle - \langle \hat{F}_+(t)\rangle\langle \hat{F}_-(t)\rangle$ from Eq. (4.47) and extract the linear slope (neglecting fast oscillations on the timescale $1/\omega_s$). This is a numerical check of the analytic expression for $V_\perp$ and $D_\perp$; the numerics and analytic expression appear to converge as F increases.

Combining these expressions, we find

$$\begin{aligned} V_\perp(t) &= \langle \hat{F}_+(t)\hat{F}_-(t)\rangle - \langle \hat{F}_+(t)\rangle\langle \hat{F}_-(t)\rangle \\ &= F(F+1) - \langle \hat{F}_z(t)^2\rangle - \exp(-2D_\perp t)\langle \hat{F}_+(0)\rangle\langle \hat{F}_-(0)\rangle \\ &= F(F+\tfrac{1}{2}) - F^2\exp(-2D_\perp t) \\ &\simeq \tfrac{1}{2}F + 2F^2 D_\perp t \end{aligned} \tag{4.47}$$

The transverse variance begins at $F/2$, that of a coherent spin state on the equator, and for $D_\perp t \ll 1$ grows linearly with time as the spin precession phase undergoes diffusion.

4.4.2 Variance of the spin component along the field axis

As for the longitudinal spin variance $V_z \equiv \langle \hat{F}_z^2\rangle - \langle \hat{F}_z\rangle^2$, for a spin state at the equator for which $\langle \hat{F}_z\rangle = 0$ we have

$$\begin{aligned} V_z(t) = e^{-2\Gamma_z}\langle \hat{F}_z(0)^2\rangle + \sigma_z^2\int_0^t\int_0^t dt_1\, dt_2\, \exp\left(-\Gamma_z[2t - t_1 - t_2]\right) \\ \times \left\langle \frac{\hat{F}_-(t_1) - \hat{F}_+(t_1)}{-2\imath}\hat{\xi}_\Delta^{\mathrm{AM}}(t_1)\,\hat{\xi}_\Delta^{\mathrm{AM}}(t_2)\frac{\hat{F}_+(t_2) - \hat{F}_-(t_2)}{2\imath}\right\rangle. \end{aligned} \tag{4.48}$$

Dropping fast-oscillating terms, the expectation value in the above integrand is

$$\begin{aligned}\langle\cdots\rangle &\simeq \frac{1}{4}\left\langle \hat{F}_-(t_1)\,\hat{\xi}_\Delta^{\mathrm{AM}}(t_1)\,\hat{\xi}_\Delta^{\mathrm{AM}}(t_2)\,\hat{F}_+(t_2) + \hat{F}_+(t_1)\,\hat{\xi}_\Delta^{\mathrm{AM}}(t_1)\,\hat{\xi}_\Delta^{\mathrm{AM}}(t_2)\,\hat{F}_-(t_2)\right\rangle \\ &\simeq \frac{1}{4}\left(\left\langle \hat{F}_-(t_1)\,\hat{F}_+(t_2)\right\rangle + \left\langle \hat{F}_+(t_1)\,\hat{F}_-(t_2)\right\rangle\right)\left\langle \hat{\xi}_\Delta^{\mathrm{AM}}(t_1)\,\hat{\xi}_\Delta^{\mathrm{AM}}(t_2)\right\rangle \\ &= \frac{F(F+\frac{1}{2})}{2}\frac{\kappa}{2}\cos(\omega_{\mathrm{s}}(t_1-t_2))\exp\bigl(-(\kappa+D_\perp)|t_1-t_2|\bigr),\end{aligned} \tag{4.49}$$

having substituted the two-time correlation functions derived earlier. The variance is

$$\begin{aligned}V_z(t) = \frac{F}{2}e^{-2\Gamma_z t} + F(F+\tfrac{1}{2})\frac{\sigma_z^2}{2}\frac{\kappa}{2}\int_0^t\!\!\int_0^t dt_1\,dt_2\,\exp\left(-\Gamma_z[2t-t_1-t_2]\right) \\ \times\cos(\omega_{\mathrm{s}}(t_1-t_2))\exp(-(\kappa+D_\perp)|t_1-t_2|).\end{aligned} \tag{4.50}$$

The result has transient damped oscillations at the Larmor frequency; we are interested in timescales much longer than $1/\kappa$ and $1/\omega_{\mathrm{s}}$, where we find

$$V_z(t) \simeq \frac{F}{2}e^{-2\Gamma_z t} + F(F+\tfrac{1}{2})\frac{D_z}{\Gamma_z}\frac{\kappa}{2}\left[\frac{\kappa+D_\perp+\Gamma_z}{(\kappa+D_\perp+\Gamma_z)^2+{\omega_{\mathrm{s}}}^2} - \frac{(\kappa+D_\perp-\Gamma_z)e^{-2\Gamma_z t}}{(\kappa+D_\perp-\Gamma_z)^2+{\omega_{\mathrm{s}}}^2}\right]. \tag{4.51}$$

Here we define the longitudinal diffusion constant $D_z \equiv \sigma_z^2/2$. We are assuming that the longitudinal damping and transverse diffusion rates are much smaller than the cavity decay rate and the Larmor frequency: $\Gamma_z, D_\perp \ll \kappa, \omega_{\mathrm{s}}$. Then

$$\begin{aligned}V_z(t) &\simeq \frac{F}{2}e^{-2\Gamma_z t} + F(F+\tfrac{1}{2})\frac{D_z}{2\Gamma_z}\frac{\kappa^2}{\kappa^2+{\omega_{\mathrm{s}}}^2}(1-e^{-2\Gamma_z t}) \\ &= \left(\frac{F}{2} - F(F+\tfrac{1}{2})\frac{D_z'}{2\Gamma_z}\right)e^{-2\Gamma_z t} + F(F+\tfrac{1}{2})\frac{D_z'}{2\Gamma_z},\end{aligned} \tag{4.52}$$

which defines a modified longitudinal diffusion constant $D_z' \equiv D_z\kappa^2/(\kappa^2+{\omega_{\mathrm{s}}}^2) = \frac{1}{2}D_z\psi\kappa/\omega_{\mathrm{s}}$. For $F \gg 1$,

$$V_z(t) \simeq \left(\frac{F}{2} - \frac{D_z' F^2}{2\Gamma_z}\right)\exp\left(-2\Gamma_z t\right) + \frac{D_z' F^2}{2\Gamma_z}. \tag{4.53}$$

The longitudinal variance decays exponentially towards the steady-state asymptote[9]

$$\begin{aligned}\lim_{t\to\infty} V_z(t) &= \frac{D_z' F^2}{2\Gamma_z} \\ &= \frac{\kappa}{|g_z|}\frac{1}{\psi},\end{aligned} \tag{4.54}$$

[9]This expression for the steady-state variance matches the one derived in Eq. (4.11) up to a factor of 2.

where again $\psi \equiv 2\kappa\omega_{\rm s}/(\kappa^2+\omega_{\rm s}^2)$. Compared to a coherent spin state on the equator, for which $\langle \hat{F}_z^2(0)\rangle = F/2$,

$$\lim_{t\to\infty}\frac{V_z(t)}{V_z(0)} = \frac{D_z' F}{\Gamma_z} = \frac{1}{F|g_z|}\frac{\kappa^2+{\omega_{\rm s}}^2}{\omega_{\rm s}} = \frac{2\kappa}{Fg_z}\frac{1}{\psi} \tag{4.55}$$

Note that increasing $\omega_{\rm s}$ beyond κ to go into the resolved-sideband limit does not further reduce the variance, as $\psi/\kappa = 2\omega_{\rm s}/(\kappa^2+{\omega_{\rm s}}^2)$ peaks at $\omega_{\rm s}=\kappa$. Given a value of κ, the optimal value of $\omega_{\rm s}$ is $\omega_{\rm s}=\kappa$ where $\psi = 1$. The minimum variance for a given κ is

$$\lim_{t\to\infty} V_z(t) = \frac{\kappa}{|g_z|}, \tag{4.56}$$

which corresponds to the variance reduction

$$\lim_{t\to\infty}\frac{V_z(t)}{V_z(0)} = \frac{2\kappa}{F|g_z|}. \tag{4.57}$$

For $Fg_z \gg \kappa$, this describes a substantial decrease in the variance.

We have simultaneously assumed (Asms. 11, 12) the limit of small modulation depth $Fg_x \ll \kappa$, and (to achieve a large variance reduction) the condition $Fg_z \gg \kappa$. In principle, these can be simultaneously satisfied by precise tuning of χ with sufficient magnetic field uniformity, to satisfy

$$(Fg_z \gg \kappa \gg Fg_x) \Longrightarrow (\cos\chi \gg \kappa/Fg_{\rm s} \gg \sin\chi) \tag{4.58}$$

which requires $\chi \ll \kappa/Fg_{\rm s}$. To generate optodynamical phenomena, we must also have $\chi \neq 0$. This implies working in a field configuration of very small but non-zero χ, meaning a field nearly aligned with the cavity axis. Assuming such fine control of χ is achievable, the conditions for significant longitudinal variance reduction ultimately boil down to $\kappa/Fg_{\rm s} \ll 1$. If sufficiently fine control of χ is impractical, or to quicken the damping process (which occurs on timescale $1/\Gamma_z \sim 1/\sin^2\chi$ for small χ), one can consider relaxing the requirement of small modulation depth, but this is beyond the scope of this work. Similarly, we have simultaneously assumed $\Gamma_z \gg \Gamma_{\rm sc}$ and $\Gamma_z \ll \kappa, \omega_{\rm s}$.

We have expressions now for both V_z and $V_\perp$. Let us check with the uncertainty principle:

$$\begin{aligned} 1 &\leq (2/F)^2\, V_z \times V_\perp \\ &\leq (2/F)^2 \left[\left(\frac{F}{2} - \frac{D_z' F^2}{2\Gamma_z}\right)\exp\left(-2\Gamma_z t\right) + \frac{D_z' F^2}{2\Gamma_z}\right] \times \left[\tfrac{1}{2}F + 2F^2 D_\perp t\right] \\ &\leq 1 + 2(D_z' F + 2D_\perp F - \Gamma_z)\, t + \mathcal{O}(\Gamma_z^2 t^2), \end{aligned} \tag{4.59}$$

which I have expanded as a power series for intermediate interaction times $t \sim T$ where $1/\kappa, 1/\omega_{\rm s} \ll T \ll 1/\Gamma_z$, as in (Asms. 9, 10, 13, and 14). This must be ≥ 1 at all times; violations of this indicate with certainty a breakdown of our assumptions. To begin simply,

let us enforce positivity of the first-order term in this expansion. We can transform this into a condition on the magnitude of the coupling strength $g_{\rm s}$. This is

$$\begin{aligned} |g_{\rm s}| &\leq \frac{2\kappa}{F}(4\cot\chi\csc\chi+\sec\chi) \\ &\lesssim \frac{8\kappa}{F\chi^2}, \end{aligned} \tag{4.60}$$

for $\chi \ll 1$. The above condition is equivalent to

$$\chi^2 \ll \frac{8\kappa}{F|g_{\rm s}|}, \tag{4.61}$$

which can be rewritten $\chi g_x F \lesssim 8\kappa$, or $u \lesssim 8/\chi$ and is true if the modulation depth is not too large (in which case $\chi < \kappa/F|g_{\rm s}|$).

4.5 Measurement of non-commuting observables

I will now consider this from a slightly different perspective. Transmitted photons have measured a combination of the longitudinal spin and the transverse spin. These measurements are accompanied by backactions that drive diffusion of the transverse spin and longitudinal spin respectively. Assuming unit detection efficiency (or equivalently, consider the measurement rates to be the total rate of measurement of the system by the outside world, whether it be the environment or the photodetectors). Considering the information carried by photons leaving the cavity and the photon flux, the diffusion and measurement rates are then [146]

$$\begin{aligned} D_\perp &= \frac{2\bar{n}g_z^2}{\kappa} \\ D'_z &= \frac{2\bar{n}g_x^2}{\kappa}\frac{\kappa^2}{\kappa^2+\omega_{\rm s}^2} \\ M_z &= \frac{2\bar{n}g_z^2}{\kappa} \\ M_\perp &= \frac{2\bar{n}g_x^2}{\kappa}\frac{\kappa^2}{\kappa^2+\omega_{\rm s}^2} \end{aligned} \tag{4.62}$$

Note the correspondences $D_\perp = M_z$ and $D'_z = M_\perp$. Also note the factors of $\kappa^2/(\kappa^2+{\omega_{\rm s}}^2)$ which come from the fact that in the resolved-sideband limit, over the lifetime of the cavity the spin precession has wound around and around, meaning that the information written to the transmitted light about the transverse spin has undergone destructive interference. In the unresolved-sideband limit on the other hand, within a cavity lifetime the spin has not precessed far and the transmitted light has sampled a well-defined precession phase. This phenomenon modifies the rate at which the transverse spin is measured $M_\perp$ and also the strength of the resulting backaction on the longitudinal spin D'_z.

The longitudinal damping rate Γ_z depends on the rate at which the cavity measures the longitudinal spin M_z, and the "gain" with which the cavity feeds this back to the spin, $G = -(\omega_s/g_z)(Fg_x/\kappa)^2[\kappa^2/(\kappa^2+{\omega_s}^2)]^2$, with $\Gamma_z = M_z G$. The gain depends on the modulation depth $u = Fg_x/\kappa$ and the sideband resolution $\kappa^2/(\kappa^2 + {\omega_s}^2)$; these determine how strongly the cavity is modulated and with what phase-sensitivity it can steer the spin.

As the system evolves, there is competition between the measurements incrementally collapsing the state and the backaction diffusion spreading the state. For short times, the longitudinal competition causes that variance to evolve as[10]

$$\frac{\mathrm{d}}{\mathrm{d}t}V_z = F^2 D'_z - F\Gamma_z, \tag{4.63}$$

while the transverse competition causes the *conditional* transverse variance to evolve as

$$\frac{\mathrm{d}}{\mathrm{d}t}\tilde{V}_\perp = 2F^2 D_\perp - F^2 M_\perp. \tag{4.64}$$

As for the product $V_z\tilde{V}_\perp$ at short times,

$$\begin{aligned}\frac{\mathrm{d}}{\mathrm{d}t}\left(V_z\tilde{V}_\perp\right) &= \tfrac{1}{2}F\left(\frac{\mathrm{d}}{\mathrm{d}t}V_z + \frac{\mathrm{d}}{\mathrm{d}t}\tilde{V}_\perp\right)\\ &= \tfrac{1}{2}F\left(F^2 D'_z - F\Gamma_z + 2F^2 D_\perp - F^2 M_\perp\right)\\ &= \tfrac{1}{2}M_z F^2\left(2F - G\right).\end{aligned} \tag{4.65}$$

This must be positive, which places a limit on the gain:

$$G < 2F. \tag{4.66}$$

This is satisfied if the modulation depth $|g_x|F/\kappa$ is not too large: roughly $(g_x F/\kappa)^2 \lesssim |g_z|F/\omega_s$.

4.6 Autonomous spin squeezing

In this section I will further analyze and compare the longitudinal and transverse behaviors to evaluate whether, and to what degree, the resulting state can be considered squeezed.

I will next consider the case where the information carried by light leaving the cavity is completely lost to the environment and examine what we can still know about the state of the spins. Afterwards, I will extend the squeezing analysis to consider measurement of the cavity output. Finally, I will include the effects of scattering from the atomic excited states.

[10]The sporadic factors of 2 seem a little surprising to me; it's possible that I missed some along the way. Alternatively, these might encode that the longitudinal measurement is measuring a slowly varying quantity while the transverse measurement is measuring an oscillatory one. Analogous to the efficiency difference between homodyne and heterodyne measurement, the transverse measurement splits its time between measuring the amplitude and phase, resulting in 1/2 relative efficiency for each.

4.6.1 Unconditional squeezing

A spin state may exhibit squeezing if the distribution of a spin component in a direction orthogonal to that of the average spin vector has smaller variance than that of a coherent spin state, and if the average spin vector length is not too significantly decreased. Metrologically relevant spin squeezing is quantified by the parameter ζ where

$$\zeta \equiv 2F \frac{\Delta F_z^2}{|\langle \boldsymbol{F} \rangle|^2}, \tag{4.67}$$

for a spin squeezed along $\boldsymbol{z}$, and we identify squeezed states by the criterion $\zeta < 1$ as described in Ref. [35]. For our spin located on the equator

$$\begin{aligned} |\langle \boldsymbol{F} \rangle|^2 &= \langle \hat{F}_+ \rangle \langle \hat{F}_- \rangle + \langle \hat{F}_z \rangle^2 \\ &= e^{-2D_\perp t} \langle \hat{F}_+(0) \rangle \langle \hat{F}_-(0) \rangle + e^{-2\Gamma_z t} \langle \hat{F}_z(0) \rangle^2 \\ &= F^2 e^{-2D_\perp t}. \end{aligned} \tag{4.68}$$

Substituting our results into the expression for ζ, we find

$$\begin{aligned} \zeta &= 2F \left[\left(\frac{F}{2} - \frac{D_z' F^2}{2\Gamma_z} \right) \exp\left(-2\Gamma_z t\right) + \frac{D_z' F^2}{2\Gamma_z} \right] F^{-2} \exp(2D_\perp t) \\ &= \left[\left(1 - \frac{D_z' F}{\Gamma_z} \right) \exp\left(-2\Gamma_z t\right) + \frac{D_z' F}{\Gamma_z} \right] \exp(2D_\perp t) \end{aligned} \tag{4.69}$$

(Asms. 9, 10, 13, 14): If the system squeezes, we expect that at intermediate times the squeezing should initially fall linearly with time from when the interaction begins because V_z decreases exponentially while the opposing effect enters at higher order through $|\langle \boldsymbol{F} \rangle|^2$. Thus in a power series in time for ζ, we expect a negative first-order term to indicate squeezing. If the first-order term is positive, the squeezing parameter increases immediately and we do not expect it to dip back down below unity at any interaction duration. For these intermediate times, we find for ζ the following series in t:

$$\zeta \simeq 1 - 2\left(\Gamma_z - D_\perp - D_z' F\right) t + \mathcal{O}\big(\Gamma_z^2 t^2\big) + \mathcal{O}\big(D_\perp^2 t^2\big), \tag{4.70}$$

from which we predict that the system exhibits (unconditional) squeezing for

$$\Gamma_z > D_\perp + D_z' F, \tag{4.71}$$

which establishes conditions on the various system parameters[11]. For significant squeezing $\zeta \ll 1$ we then require

$$\frac{D_\perp}{\Gamma_z} + \frac{D_z' F}{\Gamma_z} \ll 1. \tag{4.72}$$

[11]It turns out that if the coefficient of the first-order term is negative then the coefficient of the second-order term is positive.

This indicates that for the system to exhibit significant squeezing, the longitudinal damping rate must be strong compared to the rates of both longitudinal and azimuthal spin angle diffusion. In particular, it must be much stronger than the rate of longitudinal diffusion, by a factor F, for the longitudinal asymptotic variance to be smaller than the variance of the initial coherent state. We can separate this into (Asms. 18 and 19) on the dynamics of $\hat{F}_z$ and the transverse spin and define a parameter describing each part:

$$\Phi \equiv \frac{\Gamma_z}{D_\perp} \gg 1, \qquad \text{and} \qquad \Theta \equiv \frac{\Gamma_z}{D'_z F} \gg 1. \tag{4.73}$$

I now construct an auxiliary parameter that I call Υ defined as

$$\Upsilon \equiv (\Phi - 1)(\Theta - 1), \tag{4.74}$$

which has the property that $\Upsilon \gg 1$ iff Eq. (4.72) is satisfied. For $\Phi \gg 1$ and $\Theta \gg 1$ this parameter reduces to $\Upsilon = \Phi \times \Theta$. In terms of this parameter Θ, the squeezing parameter is

$$\zeta = \left[\left(1 - \Theta^{-1}\right) \exp(-2\Gamma_z t) + \Theta^{-1}\right] \exp(2D_\perp t) \tag{4.75}$$

The squeezing parameter is minimized at time

$$t_{\min} = \frac{1}{2\Gamma_z} \log \Upsilon, \tag{4.76}$$

for $\Upsilon \geq 1$. For $\Upsilon < 1$ the squeezing parameter ζ does not fall below unity after any interaction duration, leading to the same condition derived above: $\Upsilon > 1 \Longrightarrow \Gamma_z > D_\perp + F D'_z$.

At $t = t_{\min}$, the squeezing parameter attains its minimum value

$$\zeta_{\min} = \Upsilon^{1/\Phi} \left(\frac{1}{\Upsilon} + \frac{1}{\Theta}(1 - 1/\Upsilon)\right) \exp(1/2F). \tag{4.77}$$

Under (Asms. 4, 20): $F \gg 1$ and $\Upsilon \gg 1$, this simplifies to

$$\zeta_{\min} \approx \Upsilon^{1/\Phi} \left(\frac{1}{\Upsilon} + \frac{1}{\Theta}\right), \tag{4.78}$$

which can approach the limit $\zeta_{\min} \sim D'_z F/\Gamma_z \to 2\kappa/F g_z$ in the case that the longitudinal damping is so much faster than the transverse diffusion that the system reaches the longitudinal steady state before appreciably diffusing, which would need $\Gamma_z/\Upsilon D'_z F \ll 1$ and $D_\perp/\Gamma_z \lll 1$. and $D_\perp/\Gamma_z \lll 1$.

Consider the relation between the condition $\Phi > 1$ and the small modulation depth condition $F g_x < \kappa$. For $\omega_s = \kappa$, each of these conditions has a boundary in the parameter space plane of g_s and F, with small modulation depth requiring $g_s < \kappa/F \sin\chi$, while $\Phi > 1$ requires $g_s > 4\omega_s/F^2\psi^2 \sin\chi \tan\chi$. For $\omega_s = \kappa$, these two boundaries intersect at the point $F = 4\cot\chi$, $g_s = \kappa/4\cos\chi$. Therefore satisfying the two inequalities requires $F > 4\cot\chi \sim 4/\chi$. Within the small modulation depth restriction, optimal squeezing occurs for large F and coupling strength approaching the modulation depth limit, where the squeezing parameter has limiting value $\zeta_{\min} \to 2(\kappa/F g_x)\tan\chi \sim 2(\kappa/F g_x)\chi$.

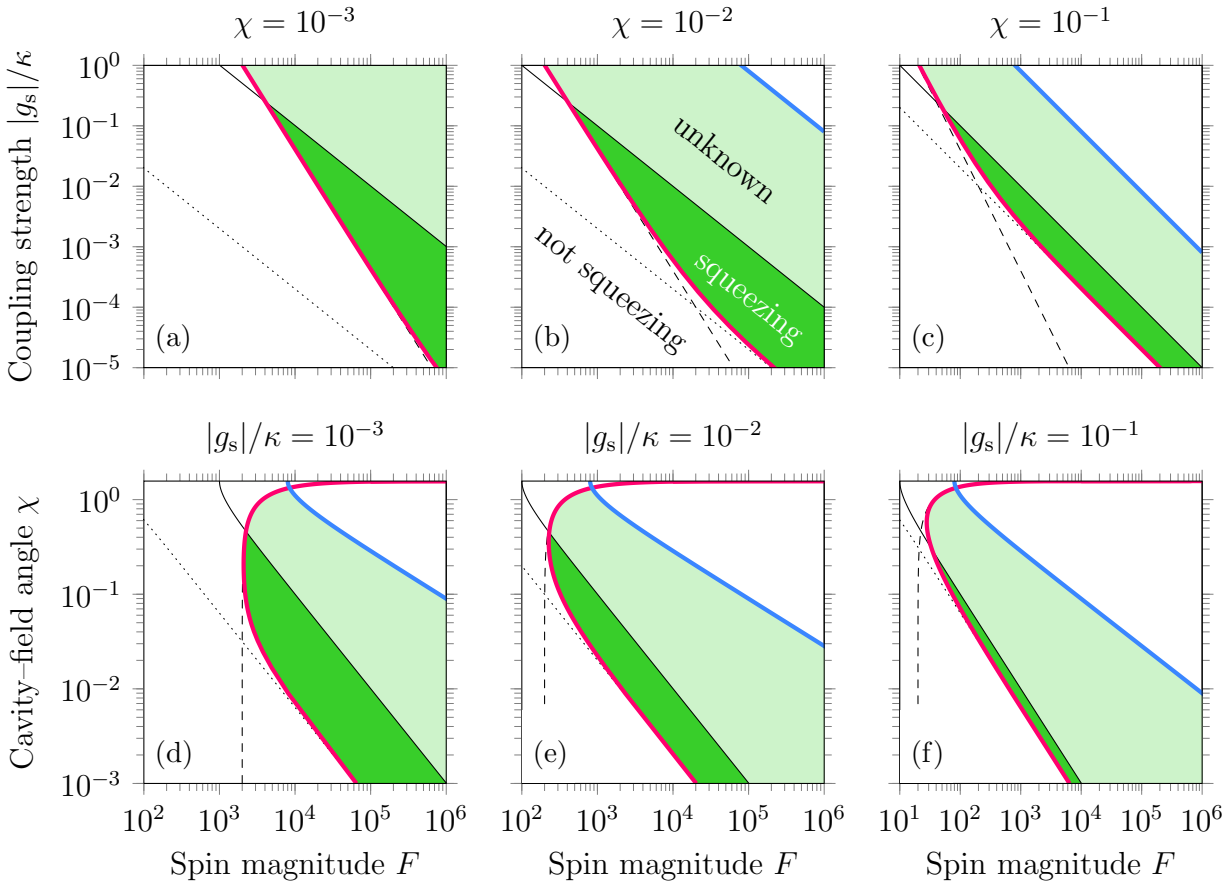


Figure 4.4: Predicted phase diagram of the unconditional squeezing phenomenon for optodynamical stabilization in the absence of scattering. The bold line separating the 'not squeezing' region from the 'squeezing' and 'unknown' regions is determined by Eq. (4.71). The dashed lines are determined by the conditions $\Theta, \Phi > 1$, and the solid line represents modulation depth $g_x F < \kappa$. Note the different horizontal limits of (c) and (f). The blue line corresponds to Eq. (4.66).

4.6.2 Conditional squeezing

Equipped with the heterodyne measurement record and its information about the light leaking from the cavity, a savvy experimentalist could do even better than the unconditional case above. The interaction between the spin and the cavity allows the cavity to measure the projection of the spin onto the cavity axis; this effectively measures both the longitudinal spin $\hat{F}_z$ and the transverse spin $\hat{F}_\perp$. The backaction of the longitudinal spin measurement drives diffusion of the transverse spin, and likewise the backaction of the transverse spin measurement drives diffusion of the longitudinal spin. The longitudinal spin is thus subject to both damping and diffusion, while the transverse spin sees only diffusion.

The transverse spin diffusion (precession phase diffusion) increases the transverse spin variance linearly with time as described in Eq. (4.47). Continuous measurement of the precession phase by the cavity, meanwhile, increases certainty in a manner inversely proportional to the measurement time. In a time t, a number of photons $2\kappa\epsilon\bar{n}t$ are detected, each carrying an amount of information about the phase of the transverse spin that scales with $(Fg_x/\kappa)^2$. Briefly ignoring the diffusion, the transverse spin uncertainty scales as [146]

$$V_\perp|_{\text{measurement}} = (4Mt + 2/F)^{-1} \tag{4.79}$$

for spin precession phase measurement rate $M \equiv 2\epsilon\bar{n}g_x^2\kappa/(\kappa^2 + \omega_{\text{s}}^2) = \epsilon\bar{n}g_x^2\psi/\omega_{\text{s}}$, where $\epsilon \in [0, 1]$ is the cavity photon detection efficiency.

Bayesian filtering allows us to construct an estimate of a dynamical variable in real time while it is subject to drift, diffusion, and imperfect measurement; in this case, we could use a Kalman filter, assuming a Gaussian distribution, to realize a real-time estimate of the phase and its variance. It should be roughly

$$V_\perp|_{\text{measurement}} \approx \frac{2}{F}\frac{2F^2D_\perp t + F/2}{4M_\perp t + 2/F} \tag{4.80}$$

From that variance, we can calculate the conditional spin magnitude. In the limit $t \to \infty$, or more specifically $t \gg 1/M$, the asymptotic form of the conditional variance of the transverse spin is

$$\lim_{t\to\infty} V_\perp|_{\text{measurement}} = \frac{F\cot^2\chi}{\epsilon}\left(\frac{\kappa^2}{\kappa^2 + {\omega_{\text{s}}}^2}\right)^{-1} \equiv V'_\perp, \tag{4.81}$$

where, as a reminder, we are still for the moment neglecting decoherence due to scattering. This leads to a conditional squeezing limit of roughly

$$\begin{aligned}
\zeta'_{\min} &= 2F\frac{\kappa}{|g_z|}\left(F^2\exp\left[-V'_\perp/F^2\right]\right)^{-1} \\
&= 2F\frac{\kappa}{|g_z|}\left(F^2\exp\left[-\frac{F\cot^2\chi}{\epsilon}\left(\frac{\kappa^2}{\kappa^2 + {\omega_{\text{s}}}^2}\right)^{-1}F^{-2}\right]\right)^{-1} \\
&= 2\frac{\kappa}{|g_z|F}\exp\left[\frac{\cot^2\chi}{F\epsilon}\left(\frac{\kappa^2}{\kappa^2 + {\omega_{\text{s}}}^2}\right)^{-1}\right] o
\end{aligned} \tag{4.82}$$

The uncertainty product must obey

$$\begin{aligned} 1 &\leq (2/F)^2 \, V_z \times V_\perp' \\ &\leq \frac{4}{F^2} \frac{\kappa}{g_z} \frac{2 \cot^2 \chi}{\epsilon}, \end{aligned} \tag{4.83}$$

which amounts to a condition on the coupling strength

$$\begin{aligned} |g_\mathrm{s}| &\leq \frac{8\kappa}{F^2 \epsilon} \cot \chi \csc \chi \\ &\lesssim \frac{2\kappa}{F^2 \epsilon} \frac{4}{\chi^2}, \end{aligned} \tag{4.84}$$

or on the modulation depth $u = g_x F/\kappa$

$$u \lesssim \frac{8}{\chi F \epsilon}. \tag{4.85}$$

Interestingly, the model considered here predicts that the steady state of the system is conditionally squeezed (in the absence of scattering). This implies that the experimenter need not track the cavity output record for the entire duration of the experiment to perform an appropriate conditional rotation. Instead, they could wait some time beyond when the system has reached its steady state, then begin tracking the cavity output record for a time long enough to resolve the precession phase, and then finally perform the conditional rotation to compensate for the random walk of the phase.

4.6.3 Scattering limit

Scattering limits us to timescales not much longer than $1/\Gamma_\mathrm{sc}$. Depending on the hierarchy of parameters, the "asymptotic" conditional squeezing limit may still be approached for intermediate times $1/\sqrt{D_\perp M} \ll T \ll 1/\Gamma_\mathrm{sc}$ for $\sqrt{D_\perp M} \gg \Gamma_\mathrm{sc}$.

Treating scattering simply as decay of the spin (assuming that scattered spins are lost when they leave the symmetrized space), we find

$$\begin{aligned} \dot{\hat{F}}_\pm &= \pm\imath\big(\omega_\mathrm{s} - g_z\sqrt{2\bar{n}}\,\hat{b}^\mathrm{AM}\big)\hat{F}_\pm \pm g_x\hat{n}\hat{F}_z - \Gamma_\mathrm{sc}\hat{F}_\pm \\ \dot{\hat{F}}_z &= \tfrac{\imath}{2} g_x\sqrt{2\bar{n}}\,\hat{b}^\mathrm{AM}(\hat{F}_+ - \hat{F}_-) - \Gamma_\mathrm{sc}\hat{F}_z \\ \dot{\hat{b}} &= \imath\hat{\Delta}_z\hat{b} + \tfrac{\imath}{2} g_x(\hat{F}_+ + \hat{F}_-)\hat{b} - \kappa\hat{b} + \sqrt{2\kappa}\hat{\xi}, \end{aligned} \tag{4.86}$$

The reduced equations are roughly

$$\begin{aligned} \dot{\hat{F}}_\pm &\approx \pm\imath\left(\omega_\mathrm{s} + \sigma_\perp \hat{\xi}_\Delta^\mathrm{AM}\right)\hat{F}_\pm - \Gamma_\mathrm{sc}\hat{F}_\pm \\ \dot{\hat{F}}_z &\approx -\Gamma_z\hat{F}_z + \sigma_z\,\hat{\xi}_\Delta^\mathrm{AM}(t)\frac{\hat{F}_+ - \hat{F}_-}{2\imath} - \Gamma_\mathrm{sc}\hat{F}_z \end{aligned} \tag{4.87}$$

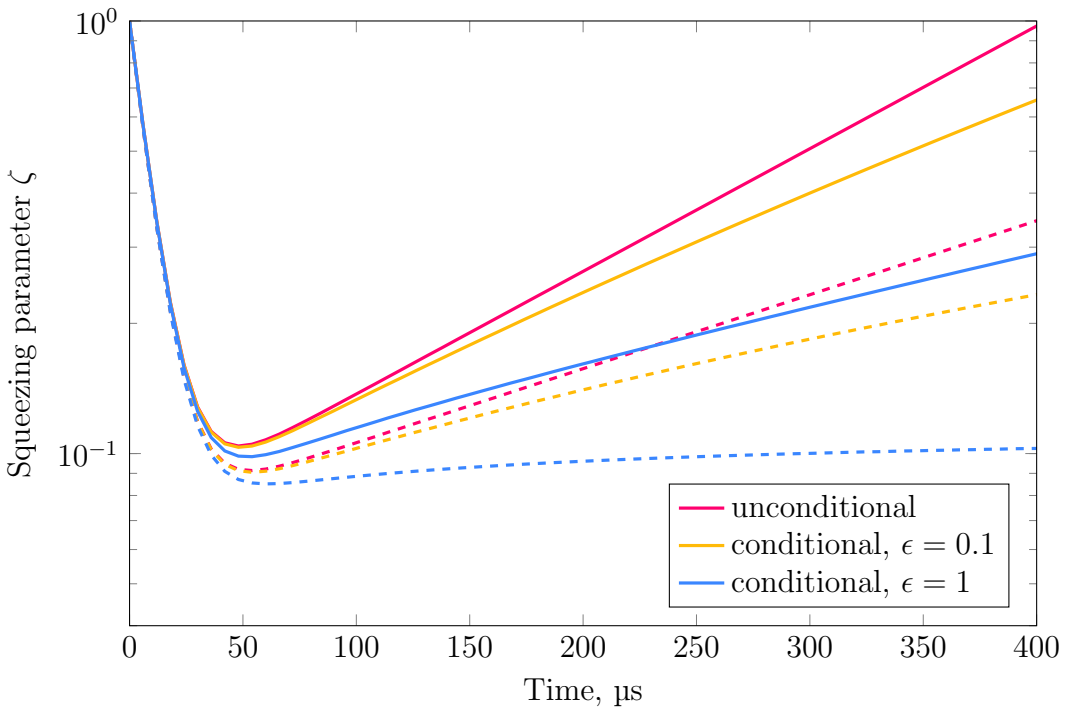


Figure 4.5: Predicted evolution of the squeezing parameter ζ, with (solid lines) and without (dashed lines) incorporating the effect of scattering from the atomic excited states, for the fiducial parameters of Tables 4.1 and 4.2. The squeezing parameter is plotted for $\epsilon = 1$ (perfect detection efficiency), $\epsilon = 0.1$, and the unconditional case (equivalent to $\epsilon = 0$).

I will assume that $\Gamma_z \gg \Gamma_{\rm sc}$. Further, I will only incorporate the scattering into the transverse spin (and thus the expected magnitude of the spin) but ignore the effect of scattering on the longitudinal variance. I think this will hopefully underestimate[12] the extent of squeezing because actually the longitudinal variance will shrink also. Then

$$\zeta = \left[\left(1 - \frac{D_z' F}{\Gamma_z}\right) \exp\left(-2\Gamma_z t\right) + \frac{D_z' F}{\Gamma_z}\right] \exp(2D_\perp t) \exp(2\Gamma_{\rm sc} t). \tag{4.88}$$

Analysis of this new squeezing parameter is then analogous to the no-scattering analysis in Sec. 4.6.1 but with the replacement $D_\perp \to D_\perp + \Gamma_{\rm sc}$. The condition to achieve squeezing then becomes

$$\Gamma_z > D_\perp + \Gamma_{\rm sc} + D_z' F, . \tag{4.89}$$

Following the earlier analysis,

$$\Phi_{\rm sc} \equiv \frac{\Gamma_z}{D_\perp + \Gamma_{\rm sc}} \gg 1, \qquad \text{and} \qquad \Theta \equiv \frac{\Gamma_z}{D_z' F} \gg 1. \tag{4.90}$$

[12] As the scattering reduces the symmetric spin magnitude then Γ_z will also shrink, but I will neglect this "cross-term" under the assumption that $\Gamma_z \gg \Gamma_{\rm sc}$.

with

$$\Upsilon' \equiv (\Phi_{\rm sc} - 1)\,(\Theta - 1)\,. \tag{4.91}$$

The squeezing parameter is then

$$\zeta_{\rm sc} = \left[\left(1 - \Theta^{-1}\right)\exp(-2\Gamma_z t) + \Theta^{-1}\right]\exp(2[D_\perp + \Gamma_{\rm sc}]t) \tag{4.92}$$

in the presence of atomic scattering. The evolutions of ζ in unconditional and conditional cases, both with and without scattering, are shown in Fig. 4.5.

For $\Upsilon_{\rm sc} \geq 1$, the new unconditional squeezing parameter is minimized at time

$$t_{\rm min,sc} = \frac{1}{2\Gamma_z}\log\Upsilon_{\rm sc}. \tag{4.93}$$

At this time, the unconditional squeezing parameter attains its minimum value in the presence of scattering, which is

$$\zeta_{\rm min,sc} = {\Upsilon_{\rm sc}}^{1/\Phi_{\rm sc}}\left(\frac{1}{\Upsilon_{\rm sc}} + \frac{1}{\Theta}(1 - 1/\Upsilon_{\rm sc})\right)\exp(1/2F), \tag{4.94}$$

which simplifies as earlier to

$$\zeta_{\rm min,sc} \approx {\Upsilon_{\rm sc}}^{1/\Phi_{\rm sc}}\left(\frac{1}{\Upsilon_{\rm sc}} + \frac{1}{\Theta}\right). \tag{4.95}$$

Unlike the situation in Refs. [93, 135] where the squeezing and scattering scale the same with detuning, here we have $\Gamma_z \propto \Delta_{\rm ca}^{-3}$ while $\Gamma_{\rm sc} \propto \Delta_{\rm ca}^{-2}$. We cannot subvert the scattering limit by going to larger detuning, but within the dispersive limit scattering actually becomes relatively *more* impactful as the detuning increases, all else equal.

However, the ratio $\Gamma_z/\Gamma_{\rm sc}$ (discussed in Eq. (4.39)) scales as $\sim CF^2 g_{\rm s}/\kappa$. This implies that if we increase the detuning $\Delta_{\rm ca}$ (where $g_{\rm s} \sim 1/\Delta_{\rm ca}$) while correspondingly increasing F, we can keep the same modulation depth Fg_x/κ while increasing the ratio $\Gamma_z/\Gamma_{\rm sc}$. Let us call the modulation depth u, so that $u \equiv Fg_x/\kappa = \frac{1}{6}Fg_0^2/\Delta_{\rm ca}$ and constrain it to some constant value by changing F and $\Delta_{\rm ca}$ simultaneously. Then $\Gamma_z/\Gamma_{\rm sc} \sim CFu/\kappa$, so increasing F while keeping u fixed reduces the relative impact of scattering. This means that scattering becomes less significant for larger spin sizes (if one keeps the modulation depth the same).

I find that in the presence of scattering, for small χ the minimum value of ζ is[13]

$$\lim_{F\to\infty}\zeta_{\rm min,sc} = \frac{2\tan\chi}{u} \sim \frac{2\chi}{u}. \tag{4.96}$$

[13]Note that we have not considered any decoherence of the spins except for scattering.

Symbol	Description	Definition	Value
Δ_{ca}	Cavity–atom detuning	$\omega_{\mathrm{c}} - \omega_{\mathrm{a}}$	$2\pi \times -10\,\mathrm{GHz}$
Γ_{e}	^{87}Rb excited state decay rate		$2\pi \times 6.1\,\mathrm{MHz}$
g_0	QED coupling strength	$d_{\mathrm{cycling}}\sqrt{\omega_{\mathrm{a}}/2\hbar\epsilon_0 V_{\mathrm{mode}}}$	$2\pi \times 13\,\mathrm{MHz}$
g_{c}	Dispersive coupling strength	$g_0^2/\Delta_{\mathrm{ca}}$	$2\pi \times -17\,\mathrm{kHz}$
g_{s}	Spin coupling strength	$g_{\mathrm{c}}/6$	$2\pi \times -2.8\,\mathrm{kHz}$
κ	Cavity half-linewidth	–	$2\pi \times 1.0\,\mathrm{MHz}$
C	Resonant cavity QED cooperativity	$g_0^2/\kappa\Gamma_{\mathrm{e}}$	28
N_{a}	Atom number	–	5.0×10^3
F	Spin magnitude	$2N_{\mathrm{a}}$	1.0×10^4
Δ_{pc}	Bare cavity–pump detuning	$\omega_{\mathrm{p}} - \omega_{\mathrm{c}}$	$2\pi \times 56\,\mathrm{MHz}$
Δ	Scalar-shifted cavity detuning	$\Delta_{\mathrm{pc}} + \alpha_0 g_{\mathrm{c}} N_{\mathrm{a}}$	0
$\bar{n}$	Average photon number	–	20
χ	Cavity–field angle	–	20 mrad
T	Intermediate interaction time	–	5 µs
ϵ	Detection efficiency	–	5.0%
τ	Spin coherence time	–	$> 10\,\mathrm{ms}$
ω_{s}	Dark Larmor frequency	$\mu_B \lvert g_f \boldsymbol{B}\rvert/\hbar$	$2\pi \times 940\,\mathrm{kHz}$

Table 4.1: The system parameters with fiducial values for sample experimental conditions.

Symbol	Description	Definition	Value
g_x	Transverse coupling strength	$g_\mathrm{s}\sin\chi$	$2\pi\times-56\,\mathrm{Hz}$
g_z	Longitudinal coupling strength	$g_\mathrm{s}\cos\chi$	$2\pi\times-2.8\,\mathrm{kHz}$
ω_s'	Effective Larmor frequency	$\omega_\mathrm{s}-g_z\bar{n}$	$2\pi\times1.0\,\mathrm{MHz}$
Δ_z	Vector-shifted cavity detuning	$\Delta-g_zF_z$	$2\pi\times62\,\mathrm{kHz}^*$
ψ	Linewidth–sideband parameter	$2\kappa\omega_\mathrm{s}/(\kappa^2+\omega_\mathrm{s}^2)$	1
λ_0	Cavity–spin granularity	$\lvert g_z\rvert/\kappa$	2.8×10^{-3}
α,β	Optical transduction coeffs.	Eq. (4.28)	–
Γ_z	Optodynamical damping rate	$-\bar{n}F^2g_x^2g_z\psi^2/2\kappa\omega_\mathrm{s}$	$2\pi\times8.9\,\mathrm{kHz}$
σ_z	Longitudinal noise amplitude	$-2g_x\sqrt{\bar{n}/\kappa}$	$1.3\sqrt{\mathrm{Hz}}$
D_z	Longitudinal diffusion constant	$\sigma_z^2/2$	$2\pi\times127\,\mathrm{mHz}$
D_z'	Modified longitud. diffusion const.	$\frac{1}{2}D_z\psi\kappa/\omega_\mathrm{s}$	$2\pi\times63\,\mathrm{mHz}$
$\sigma_\perp$	Transverse noise amplitude	$2g_z\sqrt{\bar{n}/\kappa}$	$-63\sqrt{\mathrm{Hz}}$
$D_\perp$	Transverse diffusion constant	$\sigma_\perp^2/2$	$2\pi\times320\,\mathrm{Hz}$
ζ	Squeezing parameter	$2F\Delta F_\perp^2/\lvert\langle\boldsymbol{F}\rangle\rvert^2$	–
Φ	Transverse diffusion control	$\Gamma_z/D_\perp$	28
Θ	Longitudinal diffusion control	$\Gamma_z/D_z'F$	14
Υ	Combined control parameter	$(\Theta-1)(\Phi-1)$	355
t_min	Optimal uncond. squeezing time	$(\log\Upsilon)/2\Gamma_z$	$52\,\mu\mathrm{s}$
ζ_min	Uncond. squeezing limit	$\Upsilon^{1/\Phi}(1/\Upsilon+1/\Theta)$	0.091
$\zeta_\mathrm{min,sc}$	Uncond. squeezing limit with scattering	$\Upsilon_\mathrm{sc}^{1/\Phi_\mathrm{sc}}(1/\Upsilon_\mathrm{sc}+1/\Theta)$	0.10
M_z	Total longitudinal measurement rate	$2\bar{n}g_z^2/\kappa$	$2\pi\times160\,\mathrm{Hz}$
$M_\perp$	Total transverse measurement rate	$2\bar{n}g_x^2/\kappa$	$2\pi\times63\,\mathrm{mHz}$
$M_\perp\epsilon$	Transverse measurement rate	$2\epsilon\bar{n}g_x^2/\kappa$	$2\pi\times3.2\,\mathrm{mHz}$
Γ_sc	Incoherent scattering rate	$\bar{n}\Gamma_\mathrm{e}g_0^2/\Delta_\mathrm{ca}^2$	$2\pi\times210\,\mathrm{Hz}$

Table 4.2: The composite parameters with definitions and values derived from the system parameters. The numerical values of these parameters indicated are simply the analytic definitions evaluated for the chosen set of example parameter values in Table 4.1, and are provided to offer intuition for parameter scales and facilitate comparison under a set of realistic experimental conditions. The asterisk indicates that the numerical value provided corresponds to the root mean square value, as the quantity has an expectation value of zero.

Index	Description	Condition	Value
(1)	Dispersive interaction	$\lvert\Delta_{f'}\rvert/\lvert\Delta_{\mathrm{ca}}\rvert \ll 1$	3×10^{-2}
(2)	Spin near equator	$\langle F_z^2\rangle/F^2 \ll 1$	5×10^{-5}
(3)	Large photon number	$\bar{n}^{-1} \ll 1$	5×10^{-2}
(4)	Large spin magnitude	$F^{-1} \ll 1$	10^{-4}
(5)	Small spin coupling versus effective field	$\lvert g_{\mathrm{s}}\rvert/\omega_{\mathrm{s}} \ll 1$	3×10^{-3}
(6)	Small spin coupling versus cavity linewidth	$\lvert g_z\rvert/\kappa \ll 1$	3×10^{-3}
(7)	Resonant shifted cavity	$\Delta_z/\kappa \ll 1$	1×10^{-1}
(8)	Semi-resolved effective sideband regime	$\omega_{\mathrm{s}}/\kappa \sim 1$	1
(9)	Long timescales versus effective Larmor cycle	$1/\omega_{\mathrm{s}}T \ll 1$	3×10^{-2}
(10)	Long timescales versus cavity lifetime	$1/\kappa T \ll 1$	3×10^{-2}
(11)	Small modulation depth	$F\lvert g_x\rvert/\kappa \ll 1$	6×10^{-1}
(12)	Large collective dispersive shift	$\kappa/F\lvert g_z\rvert \ll 1$	4×10^{-2}
(13)	Damping slower than cavity decay	$\Gamma_z/\kappa \ll 1$	9×10^{-3}
(14)	Damping slower than effective Larmor freq.	$\Gamma_z/\omega_{\mathrm{s}} \ll 1$	9×10^{-3}
(15)	Short timescales versus damping time	$\Gamma_z T \ll 1$	3×10^{-1}
(16)	Short timescales versus transverse diffusion time	$D_\perp T \ll 1$	1×10^{-2}
(17)	Transverse diffusion small over cavity lifetime	$D_\perp/\kappa \ll 1$	3×10^{-4}
* (18)	Damping versus transverse diffusion	$D_\perp/\Gamma_z < 1$	4×10^{-2}
* (19)	Damping versus longitudinal diffusion	$D'_z F/\Gamma_z < 1$	7×10^{-2}
* (20)	Combined squeezing parameter	$1/\Upsilon < 1$	3×10^{-2}

Table 4.3: Table of the assumed conditions and their values for the fiducial parameters. Most conditions are assumed for the purposes of approximation and are together sufficient for squeezing to occur within the model; the asterisks indicate criteria necessary for squeezing.

Chapter 5

Cavity photoassociation spectroscopy of $^{87}Rb_2$

5.1 Introduction

In the past several decades, researchers have achieved enormous advances in the control of ultracold clouds of atoms [149–156] as well as individual atoms. The development of efficient laser and evaporative cooling techniques, optical and magnetic trapping, and robust state preparation and control have allowed for a multitude of incredible scientific developments and discoveries. Similar control of cold molecules trailed that of atoms due to the relative complexity of molecules. But across a wide range of applications for atoms exist numerous opportunities for new science with molecules, if more technically demanding.

Experiments with molecules differ from those with atoms for several reasons: many more states are available in a molecule than there are in its constituent atoms alone, with many more transitions to work with and great variability in the transition energies. Molecules also offer different sensitivity to electromagnetic fields, both external and environmental fields as well as the huge internal fields found within polar molecules that present a new pathway towards precision measurement of quantities such as the electron electric dipole moment. Molecular association and dissociation additionally represent the simplest processes found in chemistry and act as model systems for basic studies of fundamental chemistry. What role do properties like quantum coherence, quantum statistics and collective enhancement, and entanglement play in chemical reactions? Do these properties offer new tunability in chemical reactions, and can chemical reactions be used to control those properties?

We sought to further integrate ultracold molecules with the quantum optics toolbox. By tuning our optical cavity to resonance with molecular transitions, we can apply cavity QED concepts and techniques to achieve strong coupling on molecular optical transitions, to influence photochemical reactions toward particular products by resonantly enhancing decay pathways, and to develop molecular quantum information transduction to optical photons.

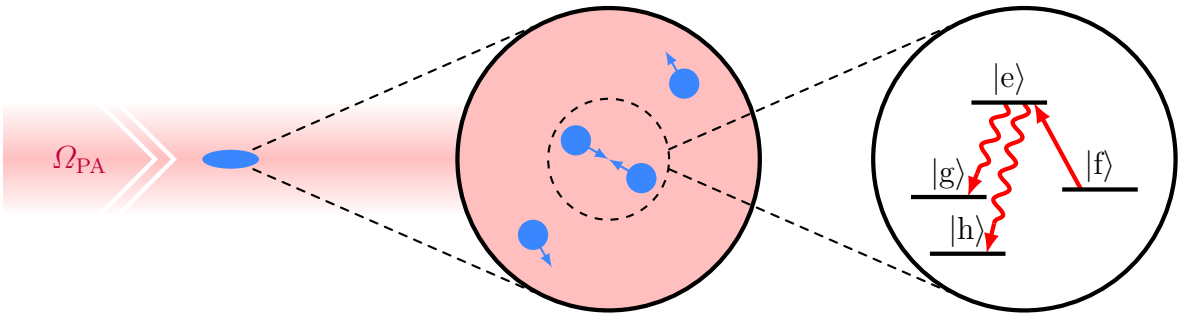


Figure 5.1: A cloud of atoms is subject to photoassociation light that drives colliding atom pairs into excited molecules which decay into various bound molecule levels.

5.2 Model and calculations of photoassociation rates

We decided to explore the production of cold molecules in E3 to try using the optical cavity for high-sensitivity readout of photoassociation experiments and to explore cavity-induced effects in photoassociation. Magnetically polarized rubidium atoms are loaded into a well of the standing-wave optical dipole trap in the optical cavity and an applied photoassociation laser couples them into rubidium dimer molecule states.

5.2.1 One-color photoassociation in free space

To begin with, consider two ^{87}Rb atoms in vacuum. There is a mutual interaction between them with a strength and sign that depends on the states of the atoms and the internuclear distance R. This is typically described in terms of the potential energy of the atomic pair as a function of R and is often described in terms of a power series in $1/R$. At long distances it is of induced-dipole–induced-dipole or van der Waals character. By choice, we work with molecular states that have mostly long-range nature, so the long-range portion of the potential mostly determines their properties, whereas the very sharp onset of the repulsive potential at shorter distances has less impact on the long-range molecules. The long-range portion of the potentials are relatively easy to calculate from atomic properties. The short-range form of the interaction is generally more difficult to calculate but can often be incorporated into the models through relatively simple parameters [149]. The states of interest for photoassociation are usually those with attractive long-range interactions.

The potential of two such atoms each in the ground S state has an attractive long-range interaction that originates physically from the van der Waals force, an induced-dipole–induced-dipole effect that scales like $1/R^6$. In the homo-nuclear dimer case with one atom in the ground S state and one in the excited P state, the interatomic potential is largely due to the resonant dipole–dipole interaction. That interaction scales like $\pm 1/R^3$, where there are two potentials that asymptote to the $S+P$ atomic limit, one attractive and one repulsive at long range. We are interested in the potential that gives rise to long-range bound molecular

states and thus focus on the long-range attractive potential. At short ranges the interaction becomes repulsive and the interaction potential thus has a minimum with a well that can host bound states. There are thus bound states of the ground manifold, those that connect to the $S+S$ atomic configuration at infinite distance, and bound states of the singly excited $S+P$ manifold. There are more quantum numbers that describe the various symmetries of the atom pair, and as the internuclear distance shrinks the potentials corresponding to the same atomic limit but different molecular symmetries split in energy. Each of these potential wells host corresponding to vibrational excitations around the equilibrium internuclear distance of the well. Further, rotation of the molecule along an axis perpendicular to the internuclear axis leads to a splitting of the vibrational states, but coupling to high rotational states is typically limited due to the angular momentum selection rules.

Photoassociation spectroscopy uses coherent light to probe transitions between states of the molecular potentials, measuring transition frequencies and strengths. These transitions can be between the unbound atomic "scattering" states or between two bound molecular states, and can be one- or multi-photon transitions. In our experiments we start with laser-cooled atoms and drive a transition to a bound excited molecular state. We call this configuration "one-color" photoassociation because we apply a single frequency of light. In some of our experiments we additionally use a second laser drive to couple the bound excited states down to bound ground states, a configuration we call "two-color" photoassociation. In the two-photon / two-color case, we will sometimes call the two transitions the "up-leg" and the "down-leg" transitions, where the up-leg is the transition from the unbound state to the bound excited state as it is the transition that raises the potential energy of the pair, while the down-leg is the transition between the bound states the couples the excited bound state to the ground bound state at lower potential energy.

When two free atoms approach one another they can scatter from their interatomic potential. The presence of light changes the effective potential that the atoms experience by coupling their initial states to the molecular manifolds. The presence of light resonant with a transition to one of the accessible molecular states generally raises the probability of the atoms scattering. In particular, as the atoms collide in the presence of near-resonant light, they can absorb a photon to be excited to a molecular state; this is specifically what is referred to by the term photoassociation. From that excited state they will quickly decay by emission of a photon. The decay takes the pair either back to the initial unbound state, or to a bound ground state.

An applied laser drive of intensity I and polarization $\hat{e}$ couples the incident unbound scattering state of energy E and partial wave ℓ to bound excited state $|\mathrm{e}\rangle$ with strength

$$V = \sqrt{\frac{2\pi I}{c}} \langle \mathrm{e} | \boldsymbol{d}_{\mathrm{m}} \cdot \hat{e} | \mathrm{f} \rangle \tag{5.1}$$

where $\boldsymbol{d}_{\mathrm{m}}$ is the molecular transition dipole moment, c is the speed of light, and I have let $\hbar = 1$. The free atom-pair state, here written $|\mathrm{f}\rangle$, is in fact actually a continuum and is specified by the incident kinetic energy E and scattering partial wave ℓ. The linewidth of the excited bound state $|\mathrm{e}\rangle$ is $\Gamma_{\mathrm{tot}} = \Gamma_{\mathrm{e}} + \Gamma_{\mathrm{b}}$, where Γ_{e} is the natural linewidth of the state

due to spontaneous emission, and Γ_b is due to stimulated emission decay that brings the pair back to the unbound scattering state. In the standard approximation that the system consists of just a single ground state and a single excited state, this is given by

$$\hbar\Gamma_\mathrm{b} = 2\pi|V|^2 \tag{5.2}$$

We can write this in approximate form

$$\hbar\Gamma_\mathrm{b} \approx 2\pi|V_C|^2|\langle \mathrm{e}|\mathrm{f}\rangle|^2 \tag{5.3}$$

where $\Omega_\mathrm{PA} = V_C/\hbar$ is the Rabi frequency, and where we have used the stationary-phase approximation that $\boldsymbol{d}_\mathrm{m}$ is slowly varying over a range around the Condon point R_C and that this region provides the primary contribution to the overlap integral. The Condon point R_C is where the ground state and excited state potentials differ by exactly the photon energy; due to the longer-range nature of the excited state potential, the ground-state potential is typically quite flat around R_C. The quantity $|\langle \mathrm{e}|\mathrm{f}\rangle|^2 \equiv \mathrm{FC}_\uparrow$ is known as the Franck–Condon factor (FCF) and describes the spatial overlap of the excited state wavefunction with the free atom-pair wavefunction. Given calculations of the wavefunctions the FCFs can be calculated directly, or the so-called reflection approximation can be used which expresses the FCF as [149]

$$|\langle \mathrm{e}|\mathrm{f}\rangle|^2 \approx \frac{\partial E_b}{\partial b}\frac{1}{|D_C|}|f_\ell(R_C, E)|^2 \tag{5.4}$$

where $\partial E_b/\partial b$ is the inverse density of states at b, D_C is the derivative with respect to R of the ground–excited potential difference evaluated at R_C, and $f_\ell(R_C, E)$ is the ground-state wavefunction also evaluated at R_C for partial wave ℓ.

What is the experimental observable that indicates the occurrence of photoassociation? There are multiple possibilities demonstrated by past experiments in the field: Some photoassociation experiments detect scattered fluorescence, while some others directly measure the number of molecules produced and can even do so with final-state selectivity — this is often performed with pulsed ionization followed by ion detection [149, 157]. Our experiment is already configured to measure atom numbers [56]; thus, as the photoassociated molecules are typically lost from the optical dipole trap confining the atoms, the simplest way for us to observe these scattering events is through the associated reduction in the atom number. However, there are effects other than photoassociation that lead to atom loss, including single-atom off-resonant light scattering and fluctuation of the trapping laser intensity. These both lead to heating, which in turn leads to loss of atoms from the trap as the hottest atoms gain enough kinetic energy to escape the trap [158, 159]. There also occur atomic Raman transitions that put atoms into untrapped atomic states . To distinguish photoassociation from these, we look specifically for laser frequency-dependent reduction in the atom number.

Excited molecules are lost approximately at rate Γ_e by spontaneous decay. The rate of scattering loss events for unbound atoms at kinetic energy E is then

$$K_p(E) = v_\mathrm{rel}\frac{\pi}{k^2}\sum_{\ell=0}^{\infty}(2\ell+1)\frac{\hbar\Gamma_\mathrm{e}\Gamma_\mathrm{b}(E,\ell)}{\Delta_1^2 + (\hbar\Gamma_\mathrm{tot}/2)^2}, \tag{5.5}$$

with $\Delta_1 \equiv E + h\nu - h\nu_0 - S_b(E)$ is the single-photon detuning, where ν is the laser frequency; ν_0 is the energy of the bound state relative to that of the unbound pair, assuming no kinetic energy. The total decay rate of the excited state is $\Gamma_{\rm tot} = \Gamma_{\rm b} + \Gamma_{\rm e}$, where $\Gamma_{\rm b}$ is the stimulated emission decay rate introduced earlier. Integrating over the thermal distribution of the vapor yields the detection rate constant as a function of temperature

$$K_p(T) = \frac{2}{\sqrt{\pi}} \int_0^\infty dE\, \sqrt{E}\, e^{-E/k_B T} K_p(E) \tag{5.6}$$

$$\approx \frac{\pi v_{\rm rel}}{k^2} |S_1|^2, \tag{5.7}$$

in terms of the wavenumber k, and approximating that the atoms are cold enough that only s-wave ($\ell = 0$) scattering contributes and that the Doppler shifts ($\sim$50 kHz for temperatures $\sim$10 µK) are small compared to the transition linewidths ($\sim$10 MHz), such that the thermal average simplifies. This is written in terms of the scattering probability [160–162]

$$|S_1|^2 = \frac{\Gamma_{\rm e}\Gamma_{\rm b}}{\Delta_1^2 + [(\Gamma_{\rm e} + \Gamma_{\rm b})/2]^2}. \tag{5.8}$$

The total collision event rate is then $K_p n^2$ in a gas of uniform density n. Assuming that every spontaneous emission from the excited state leads to a bound ground-state molecule that is lost from the trap (neglecting spontaneous decay back to the unbound states), the rate of atom loss from the trap is $2K_p n^2$. The rate of production of each of the various molecular states is more complicated, because it is determined by branching from the excited state: the sum of the production rates must equal the total pair loss rate, but not all ground states are populated equally. The couplings between the excited bound state $|{\rm e}\rangle$ and the ground bound states $|{\rm g}\rangle$ depend on the Franck–Condon factors $|\langle {\rm g}|{\rm e}\rangle|^2$. This typically leads to several prominent decay pathways populating various ro-vibrational ground states with non-vanishing spatial alignment with the excited state.

The near-resonant laser field thus enables photochemical reactions

$$2{\rm Rb} + h\nu \longrightarrow \sum_i {\rm Rb}_{2,(i)} + h\nu'_{(i)} \tag{5.9}$$

that occurs at a rate that depends on the laser intensity, the FCFs, and the density and temperature of the atomic vapor. The reagents (pairs of unbound atoms) react in the presence of light to form products (the bound ground-state-manifold molecules) by way of a reaction intermediate (the bound excited molecules). As the excited state has multiple decay pathways (back to the original state, or to a individual ro-vibrational bound states (i) of possibly multiple ground state manifolds of different symmetry), the specificity of this chemical reaction is limited.

5.2.2 Two-color photoassociation in free space

One can instead perform an alternative experiment in which the atoms are illuminated by two co-propagating laser drives. We consider the case that the second laser resonantly couples

the excited state down to a bound ground state with Rabi frequency $\Omega_{\mathrm{bb}}^2 \simeq \Omega_{\mathrm{a}}^2 |\langle \mathrm{g}|\mathrm{e}\rangle|^2$, where Ω_{a} is the Rabi frequency between the corresponding asymptotic atomic states, and $|\langle \mathrm{g}|\mathrm{e}\rangle|^2$ is the FCF for the bound–bound molecular transition. Analytic treatment of this configuration was derived in Refs. [160, 163], and I quote their result for the probability of scattering into $|\mathrm{g}\rangle$:

$$|S_2|^2 = \frac{\delta^2 \Gamma_{\mathrm{e}} \Gamma_{\mathrm{b}}}{[(\Gamma_{\mathrm{e}} + \Gamma_{\mathrm{b}})\delta/2]^2 + (\Delta_+ \Delta_-)^2}, \tag{5.10}$$

where δ is the two-photon detuning, the detuning of the two-photon transition from the initial scattering state to $|\mathrm{g}\rangle$, and $2\Delta_\pm = (\Delta_1 + \delta) \pm \sqrt{(\Delta_1 - \delta)^2 + 4\hbar^2 \Omega_{\mathrm{bb}}^2}$.

This expression indicates that on perfect two-photon resonance ($\delta = 0$) the probability of scattering a photon from the excited state goes to zero; this is a destructive quantum interference effect. This "transparency" feature can be very narrow and can be used to precisely measure the binding energy of the molecular ground states relative to the incident states. The transparency feature may be difficult to observe if $|\langle \mathrm{g}|\mathrm{e}\rangle|^2$ is small, while it may be more accessible for states with large Franck-Condon factors.

In terms of the photochemical reaction picture, the addition of the second resonant laser drive can enhance the reaction specificity by resonantly selecting a single level of the ground state manifold while all others are off-resonant; if the two laser drives have sufficient two-photon coherence, the atom pairs will end up in a coherent superposition of the initial state and the selected bound state while the scattering rate into other bound states from the excited state is suppressed.

5.2.3 Atom number during photoassociation

For a cloud of atoms of uniform density n subject to single-body losses at a rate β and two-body losses at rate $K_p = q|S|^2$, the atom density evolves as

$$\dot{n} = -2K_p n^2 - \beta n, \tag{5.11}$$

If the photoassociation losses happen slower than the atoms move within the trap, and we assume that the temperature is constant, then the shape of the atomic density distribution remains approximately constant as atoms are lost. In practice, the photoassociation experiments described here are performed over tens of milliseconds, but a significant fraction of the atoms are typically lost within the first ten milliseconds; this approximation may not be appropriate during that time given the radial trap frequency $\omega_{\mathrm{r}} \sim 2\pi \times 1\,\mathrm{kHz}$.

The atomic density distribution is approximately Gaussian with some radial and axial sizes $n(r,z) = N \exp\left[-((r/r_0)^2 + (z/z_0)^2)/2\right]/r_0^2 z_0 \sqrt{2\pi}$, and the atom number is given by the integral over the volume $V \sim \pi r_0^2 z_0$ (for convenience this is written in terms of $V_0 \equiv r_0^2 z_0 \sqrt{16\pi}$):

$$\dot{N} = -\int [2K_p n(r,z)^2 + \beta n(r,z)] r\, dr\, dz = -\frac{2K_p}{V_0} N^2 - \beta N, \tag{5.12}$$

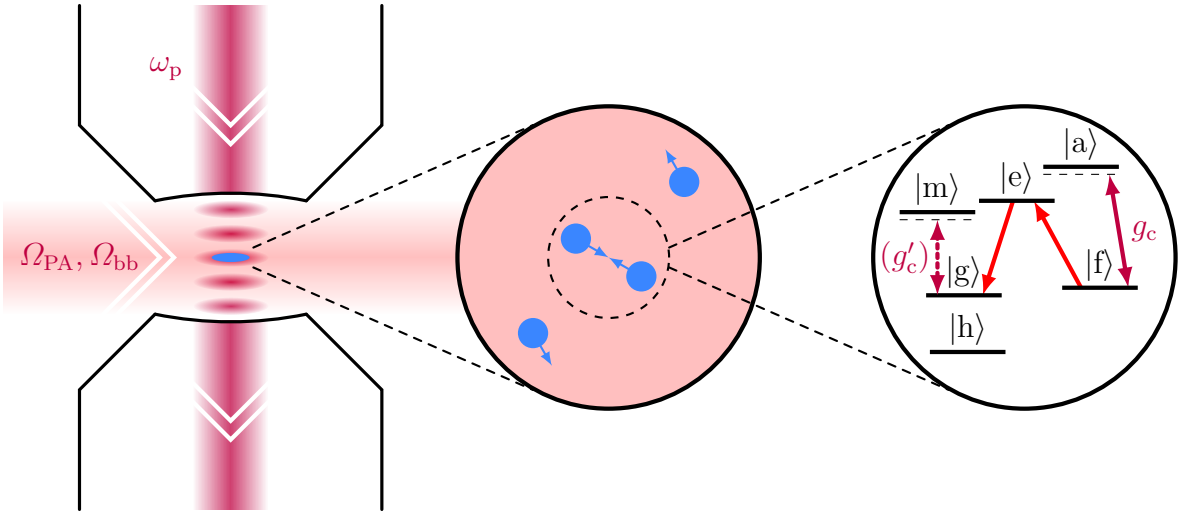


Figure 5.2: Atoms are held in a cavity mode standing wave optical dipole trap. Light applied from the side of the cavity photoassociates colliding atom pairs into excited molecules which decay into various bound molecule levels. Here, the cavity is nearly resonant with an atomic (bound–bound molecular) transition shown $|\mathrm{f}\rangle$ to $|\mathrm{a}\rangle$ ($|\mathrm{g}\rangle$ to an auxiliary molecular excited state $|\mathrm{m}\rangle$), facilitating nondestructive dispersive measurement of the atom (molecule) number.

and then by integrating in time, the atom number is

$$N(t) \simeq \frac{N(0)\exp(-\beta t)}{1+2(q/V_0)|S|^2 N(0)t}, \tag{5.13}$$

with $q \equiv \pi v_{\mathrm{rel}}/k^2$, where we have assumed that the single-body loss rate is small, but not completely negligible, such that the cross-terms between one- and two-body loss can be neglected.

We attribute to β all single-body loss processes. These include losses due to atomic scattering, which we can tune with the detuning from the bare atomic transition Δ_a; and other loss sources such as background gas collisions due to the chamber pressure. In our experiment the chamber pressure is good enough that these losses are not too large. Other neglected loss processes include three-body collisional losses, which are controlled by the atom density. In this experiment, the atom density is low enough that these losses are negligible.

5.2.4 Photoassociation in a cavity nearly resonant with an atomic transition

Consider now the one- and two-color photoassociation configurations with the atoms not in free space but within the volume of a single-mode optical cavity, with the cavity resonant

far off resonance from any of the molecular transitions, but nearly resonant with the atomic transition. This is the configuration ultimately utilized in many of our experiments, where we direct the photoassociation lasers toward the atomic cloud from the side of the cavity. The cavity in this case effectively plays no role in the photoassociation dynamics but allows for a highly sensitive dispersive measurement of the atom number N in real-time throughout the photoassociation interaction. For each experimental iteration we precisely measure the atom number before photoassociation by sweeping a laser across the cavity resonance, then fix the frequency of that laser near the cavity to obtain a time trace of the atom number throughout photoassociation, then repeat the sweep measurement to measure the final atom number. We fit our measured atom number traces to Eq. 5.13, which predicts the final atom number, as well as dynamics of the atom number during the interaction, in terms of the scattering probability $|S|^2$ and loss rate K_p. See Fig. 5.7.

5.2.5 Photoassociation in a cavity nearly resonant with a molecular transition

Another possible configuration involves setting the cavity nearly resonant with a bound–bound molecular transition from $|\mathrm{g}\rangle$ but not the one between $|\mathrm{g}\rangle$ and $|\mathrm{e}\rangle$. In this case, the cavity will not couple to the photoassociation excitation, but can potentially be used to dispersively measure the molecule number in an analogous way to how we typically use the cavity near atomic resonance to dispersively measure the atom number. We are interested in this as a way to observe the photoassociation process nondestructively, but did not have a chance to explore this configuration in our experiment.

5.2.6 Cavity-assisted photoassociation

One can also consider a new configuration, where a single photoassociation laser couples $|\mathrm{f}\rangle$ and $|\mathrm{e}\rangle$ as in Sec. 5.2.1, but where the cavity is nearly resonant with the bound–bound molecular transition rather than nearly resonant with the atomic transition[1]. Its dispersive shift will no longer be as sensitive to the atom number, and instead the molecular excitation can now couple to the cavity mode, exchanging into a cavity photon.

The cavity will be described with Fock states (number eigenstates) denoted $|0\rangle$, $|1\rangle$, and so on, with the combined molecule–cavity state labeled, for example, $|\mathrm{g}, 1\rangle \equiv |\mathrm{g}\rangle_{\mathrm{molecule}} \otimes |1\rangle_{\mathrm{cavity}}$. A classical drive applied from the side of the cavity couples $|\mathrm{f}, n\rangle$ and $|\mathrm{e}, n\rangle$ with Rabi frequency Ω_{PA}; the cavity is either driven or undriven, and its mode couples $|\mathrm{e}, n-1\rangle$ and $|\mathrm{g}, n\rangle$ with coupling strength $g = g_0\sqrt{n+1}$ which replaces the coupling Ω_{bb}. The state $|\mathrm{g}, n\rangle$ decays to $|\mathrm{g}, n-1\rangle$ by leakage into the cavity output at a rate $\Gamma_{\mathrm{b}} = 2\kappa$. Scattering now takes on a different nature as there are two distinguishable decay channels, one ("channel

[1]Note that since the photoassociation laser is incident from the side of the cavity, the two-photon transition now couples two light fields that are not co-propagating; this leads to a potentially problematic Doppler shift on the two-photon resonance.

a") by emission of a photon into free space from the state $|\mathrm{e},0\rangle$ to $|\mathrm{h},0\rangle$ where $|\mathrm{h}\rangle$ represents all molecular states other than the one resonantly coupled via the cavity, and one ("channel b") by emission of a photon into the cavity output taking $|\mathrm{e},0\rangle$ to $|\mathrm{g},1\rangle$; each channel has an associated scattering probability. The scattering probability into channel b is [160]

$$|S_b|^2 = \frac{\Gamma_\mathrm{b}\Gamma_\mathrm{b}\Omega_\mathrm{bb}^2}{(\Gamma_\mathrm{b}\Delta_1 + (\Gamma_\mathrm{e}+\Gamma_\mathrm{b})\Delta_2)^2/4 + ((\Gamma_\mathrm{e}+\Gamma_\mathrm{b})\Gamma_\mathrm{b}/4 - \Delta_1\Delta_2 + \Omega_\mathrm{bb}^2)^2}, \tag{5.14}$$

while the scattering probability into channel a is

$$|S_a|^2 = \frac{\Gamma_\mathrm{e}\Gamma_\mathrm{b}(\Delta_2^2 + \Gamma_\mathrm{b}^2/4)}{(\Gamma_\mathrm{b}\Delta_1 + (\Gamma_\mathrm{e}+\Gamma_\mathrm{b})\Delta_2)^2/4 + ((\Gamma_\mathrm{e}+\Gamma_\mathrm{b})\Gamma_\mathrm{b}/4 - \Delta_1\Delta_2 + \Omega_\mathrm{bb}^2)^2}. \tag{5.15}$$

In the case of $\Delta_1, \Delta_2 \to 0$,

$$|S_b|^2 = \frac{\Gamma_\mathrm{b}\Gamma_\mathrm{b}\Omega_\mathrm{bb}^2}{[(\Gamma_\mathrm{e}+\Gamma_\mathrm{b})\Gamma_\mathrm{b}/4 + \Omega_\mathrm{bb}^2]^2}, \tag{5.16}$$

$$|S_a|^2 = \frac{\Gamma_\mathrm{b}^2\Gamma_\mathrm{e}\Gamma_\mathrm{b}/4}{[(\Gamma_\mathrm{e}+\Gamma_\mathrm{b})\Gamma_\mathrm{b}/4 + \Omega_\mathrm{bb}^2]^2}. \tag{5.17}$$

The ratio of products $|S_b|^2/|S_a|^2 = \Omega_\mathrm{bb}^2\Gamma_\mathrm{b}/\Gamma_\mathrm{e}(\Delta_2^2 + \Gamma_\mathrm{b}^2/4) \to 4\Omega_\mathrm{bb}^2/\Gamma_\mathrm{b}\Gamma_\mathrm{e} = C$, the cooperativity, on resonance.

Once again revisiting the photochemical reaction perspective, the resonant cavity plays an interesting role. Although it does not drive the reaction, its presence enhances the probability and rate of the reaction proceeding through a particular decay pathway, thus increasing the specificity of the reaction as a greater fraction of the reagents and intermediates convert to one particular product over the other possibilities. We can write the chemical reaction as

$$2\mathrm{Rb} + h\nu_\mathrm{laser} \xrightarrow{\text{cavity}} \mathrm{Rb}_{2,(i)} + h\nu'_\mathrm{cavity} \tag{5.18}$$

where we indicate that the unbound pair reacts with the laser drive photon to produce a product molecule in a specific state (i) and a cavity photon. We consider the role of the cavity here to be that of a catalyst.

It is difficult to observe the molecular states if non-photo-associative losses surpass photoassociative losses. The off-resonant atomic scattering rate is $\Gamma_\mathrm{a} = \Gamma_\mathrm{e}\Omega_\mathrm{PA}^2/\Delta_\mathrm{a}^2$. The ratio of molecule-productive scattering to atomic scattering is $K_p/\Gamma_\mathrm{a} \sim q|S_b|^2/\Gamma_\mathrm{a}$ which is $\sim \Gamma_\mathrm{b}\Omega_\mathrm{a}^2\Delta_\mathrm{a}^2|\langle\mathrm{g}|\mathrm{e}\rangle|^2|\langle\mathrm{e}|\mathrm{f}\rangle|^2/\Gamma_\mathrm{e}D$, where D is the denominator in Eqs. 5.16 and 5.17. This rough scaling motivates our search for suitable experimental parameters and states; we see that we want to choose a large detuning from atomic resonance Δ_a to suppress atomic scattering and to select states accessible via transitions with favorable Franck-Condon factors.

5.3 Selection of molecular manifolds and states

We focus our attention on photoassociation transitions from the disassociated state to the 0_g^- excited state and deexcitation transitions from 0_g^- down to the $a^3\Sigma$ manifold as shown in Fig. 5.3, the selections of which we now motivate and explore.

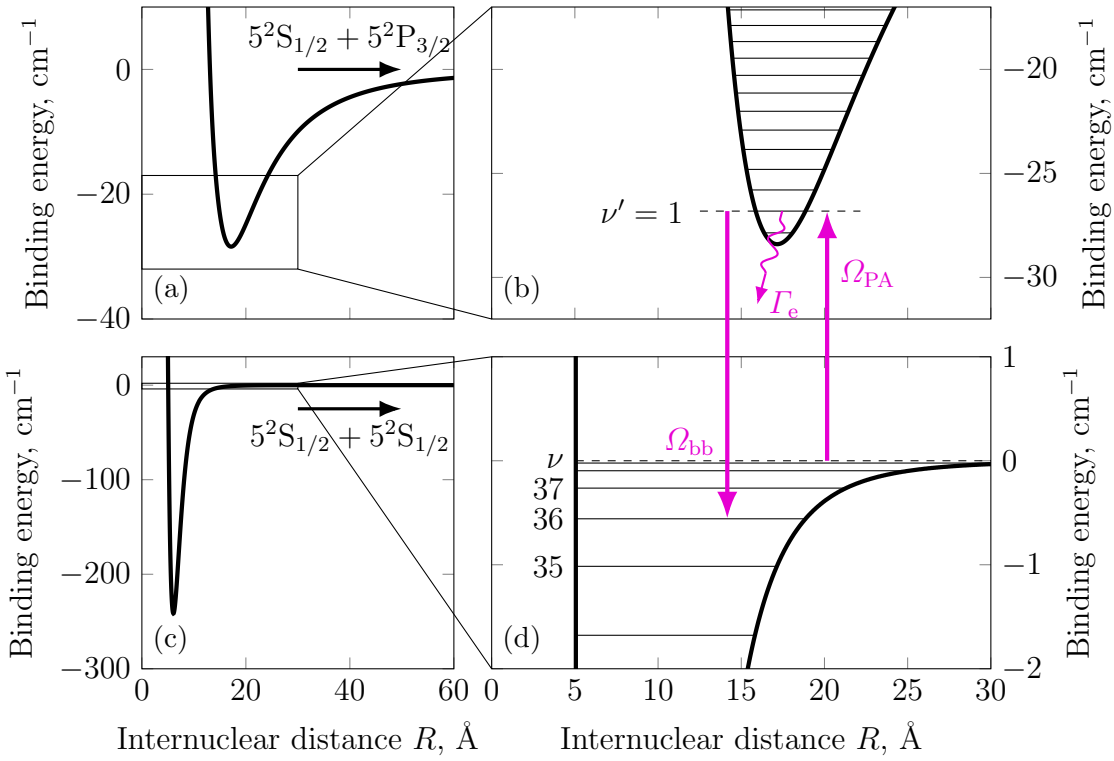


Figure 5.3: Vibrational energy level diagram of the $^{87}Rb_2$ $a^3\Sigma$ and 0_g^- potentials. (a) and (b) show the excited 0_g^- potential, while (c) and (d) show the ground $a^3\Sigma$ potential. (b) and (d) are zoomed into the potential in the regions indicated by the boxes in (a) and (c) respectively. The asymptotic atomic states are indicated in (a) and (c). The binding energies are relative to an unbound pair of atoms in the corresponding asymptotic atom states.

The process begins with the photoassociation of two unbound neutral atoms into a bound excited molecule. These bound excited molecules are bound in the sense that the wavefunction tends toward zero as the internuclear distance increases (or decreases), but they are unbound in the sense that their excitation can decay radiatively decay into unbound atomic states. Atoms are resonantly photoassociated into bound excited molecules at a rate that depends on the experimental configuration and the stimulated linewidth of the excited bound state described by [160, 164, 165]. To drive two-photon Raman transitions to these states requires two laser beams with the correct two-photon detuning and also sufficient relative phase coherence.

The 0_g^- state is asymptotically connected to $S_{1/2}$–$P_{3/2}$, meaning that as the internuclear distance is taken out to infinity, the 0_g^- state connects to the $S_{1/2}$–$P_{3/2}$ state of an excited pair of isolated atoms. The 0_g^- manifold was chosen because its states have very long spatial distributions, which makes them suitable for direct photoassociation due to their large Franck-Condon factors. On the other hand, coupling from such states into deeply bound

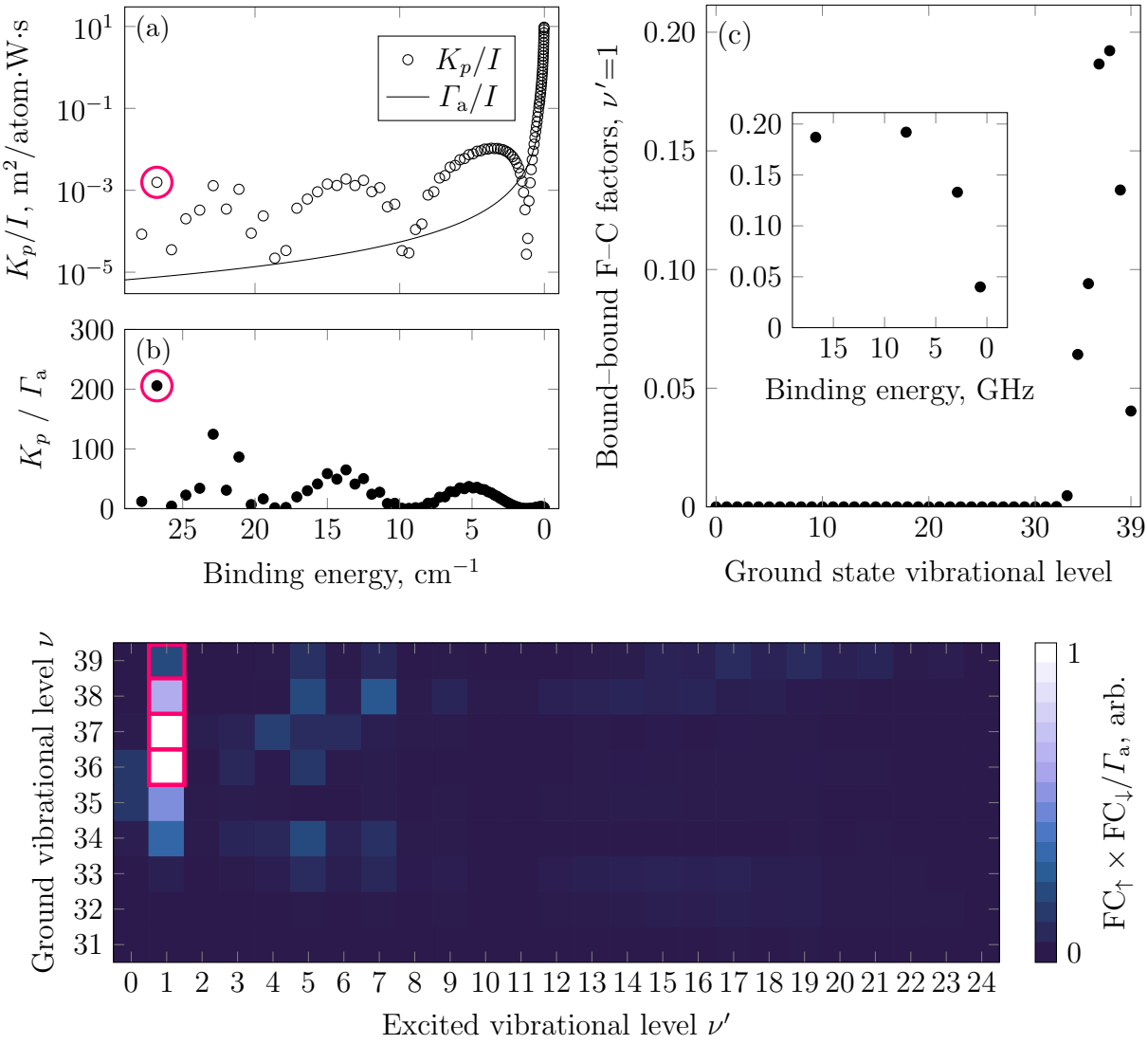


Figure 5.4: (a) The calculated one-color photoassociation rate K_p, normalized by the laser intensity I, plotted for transitions to the bound excited states of 0_g^- in the low-intensity limit for $T = 5\,\mu\text{K}$ and $n_{\text{Rb}} = 10^{12}$ cm^{-3}. (b) The ratio of the photoassociation rate K_p to the atomic scattering rate Γ_a. In both (a) and (b) the large circles highlight the selected $\nu' = 1$ excited state, which we selected for our experiments due to its favorable ratio $K_p/\Gamma_a \sim 200$ for our parameters. (c) The Franck–Condon factors (FCFs) for transitions between 0_g^- excited state $\nu' = 1$ and $a^3\Sigma$ ground states ν. The factors are small except for the most loosely bound states. The inset shows the four highest levels at their binding energies. (d) The product of the calculated FCFs $\text{FC}_\uparrow \equiv |\langle \text{e}|\text{f}\rangle|^2$ and $\text{FC}_\downarrow \equiv |\langle \text{g}|\text{e}\rangle|^2$ divided by the atomic scattering rate Γ_a for a two-color photoassociation transition from the $T = 5\,\mu\text{K}$ scattering state to the $a^3\Sigma$ vibrational level ν by way of 0_g^- level ν'. The outlined squares highlight the four transitions we experimentally observe in Fig. 5.9.

states of the $a^3\Sigma$ manifold is more challenging due to the low Franck-Condon factors of such transitions (because these bound states live at much smaller internuclear separations than do the excited 0_g^- states). We found a promising path by targeting not the deeply bound $a^3\Sigma$ states but the very weakly bound ones, which have internuclear distances comparable to those of the excited states and thus reasonable Franck-Condon factors. These states and the transitions to them proved accessible and in fact rather convenient, as the low binding energy of these states implies that we can generate the light with one laser and an electro-optical modulator in the GHz range, or two lasers coupled with an offset lock again using GHz electronics. The implementation of the latter approach enabled us to observe these bound molecular states in our cavity.

When exciting atoms into excited molecular states, one must consider both the shower of many accessible decay pathways that bring molecules into states that are not trapped or otherwise not useful, and the relative rates of the photoassociation transition versus the scattering rates off the single-atom excitation transitions (here the D_2 line). We calculated which vibrational 0_g^- level offers the most favorable ratio $\Gamma_{\mathrm{PA}}/\Gamma_{\mathrm{scattering}}$, and which bound $a^3\Sigma$ levels would be most accessible from each of those excited levels. To do this we calculated the Franck–Condon factors and the photoassociation rates for the various transitions between these manifolds, following the methods in Refs. [166, 167]. From this we evaluated the two-photon scattering probability in combination with the single-photon scattering loss rate to determine which transitions posed the most advantageous targets. We chose to explore the photoexcitation transition to the excited vibrational state $\nu' = 1$ because of the relatively large transition strength and its large detuning from the excited atomic state. For the deexcitation transition we probed the ground vibrational states with $\nu \in \{36, 37, 38, 39\}$ (which are the four most weakly bound vibrational levels of the $a^3\Sigma$ manifold) because of the strengths of the transitions to the $\nu' = 1$ excited state; as well as the accessibility to our laser offset lock system, capable of producing a two-photon frequency difference up to 20 GHz. Since we pump the atoms into the stretched state $|F = 2, m_F = +2\rangle$ as opposed to some optical pumping schemes that pump into the $m_F = 0$ clock states, in our system the atom pairs are in the triplet state. This simplifies the situation considerably because we need only consider the triplet states without singlet mixing.

5.4 Molecular spectroscopy experiments

5.4.1 One-photon molecular spectroscopy experiments

To probe the molecular excited states, we performed spectroscopy using one photoassociation laser field incident from the side of the cavity. Measurement of the atom number before and after a photoassociation time probes the scattering probability in Eq. 5.8 through fitting to Eq. 5.13.

Our initial measurements probed molecular states close to the atomic D_2 line, leading to significant heating, which led us to instead study the more deeply bound excited states.

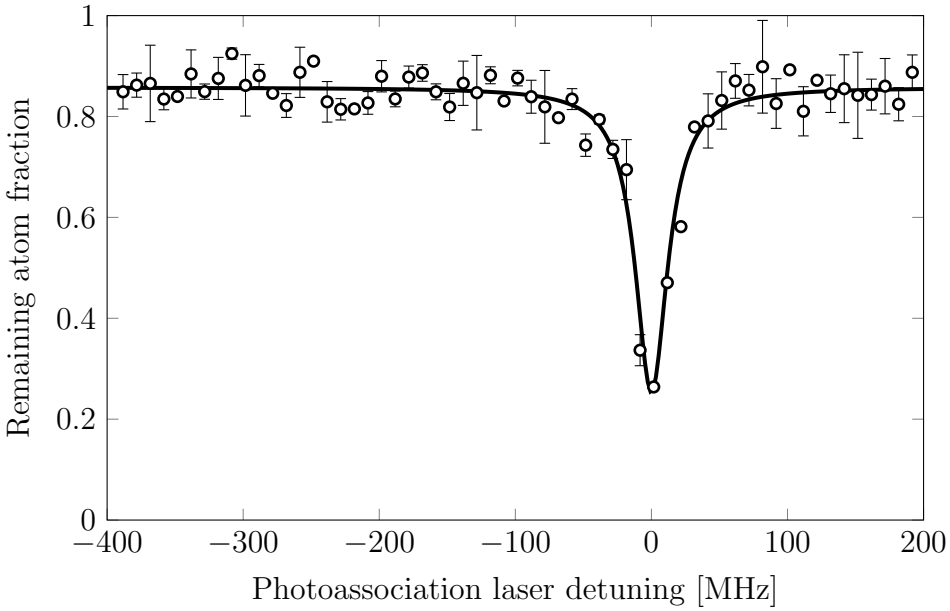


Figure 5.5: Single-color photoassociation spectroscopy of $\nu' = 1$. The atom loss feature corresponds to the formation of molecules in the 0_g^- $\nu' = 1$ state. The solid line is a fit of Eqs. 5.8 and 5.13 to the experimental data points. The center of the feature was measured to be 383 422 609(100) MHz.

Later experiments focused on the $\nu' = 1$ state that sits about 0.8 THz below the atomic line; we calculated that the photoassociation rate to this state would greatly exceed the atomic scattering rate at such large detuning. Data collected around the frequency of the $\nu' = 1$ state of the 0_g^- manifold are shown in Fig. 5.5. Working with atoms in the $F = 2$ ground state, we measure the transition frequency to 0_g^- $\nu' = 1$ to be 383 422 609(100) MHz; the uncertainty in this number is systematic and related to an imperfectly corrected drift in the absolute calibration of our laser frequency measurement device.

5.4.2 Two-photon molecular spectroscopy experiments

With atoms loaded in the cavity ODT, we perform spectroscopy on the molecular transitions using two classical laser fields incident from the side of the cavity. Measurement of the atom number before and after a photoassociation time probes the scattering probability in Eq. 5.10 through fitting to Eq. 5.13. Our two-photon measurements were conducted using the 0_g^- $\nu' = 1$ as the intermediate state, with the frequency of either the photoassociation light or the molecular-transition light held constant and the other scanned to detect molecular states at binding energies given by the two-photon frequency difference $\Delta_1 - \Delta_2$ The two-photon detuning $\delta = [E_\nu - (\Delta_1 - \Delta_2)]/\hbar$ is the difference between this quantity and a given state's binding energy E_ν. Note that the Doppler effect can be large compared to the linewidth of

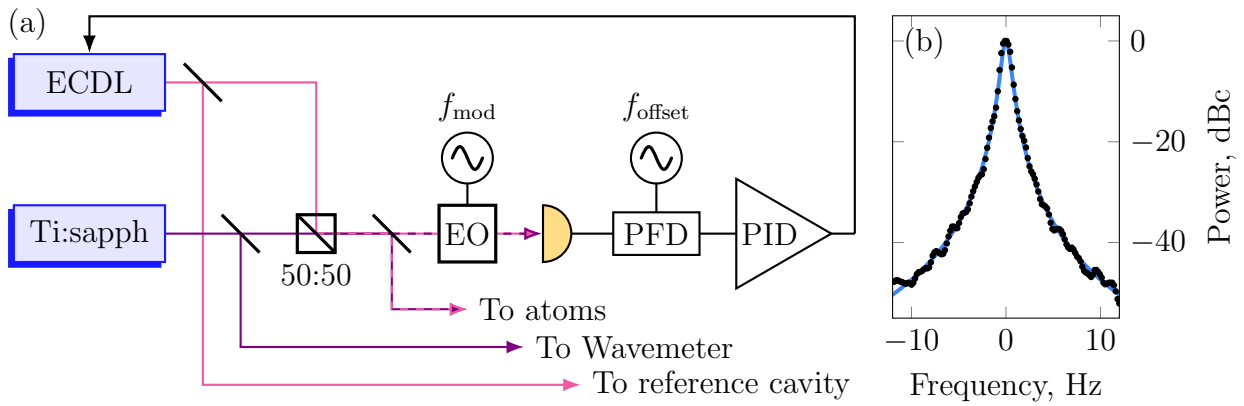


Figure 5.6: (a) Laser stabilization and beat-note lock schematic for two-color photoassociation, designed and constructed by Josh Isaacs. We stabilize the ECDL to the reference cavity while monitoring the frequency of the Ti:sapph laser with the Wavemeter. A 50:50 cube combines light from the both ECDL and from the Ti:sapph and we send most of the combined light to the atoms by fiber. We sample a portion of the combined light, modulate it with an electro-optic modulator (EO) driven by a function generator at f_{mod}, and measure it on a photodiode. Interference between the $+1$ order of the lower-frequency laser and the -1 order of the higher-frequency laser is compared to a function generator at f_{offset} using a phase-frequency detector (PFD) and used for stabilization of the ECDL via a proportional–integral–derivative controller (PID). The relative frequency is stabilized to be $f_{\mathrm{offset}} + 2f_{\mathrm{mod}}$. (b) Two-laser beat-note spectrum, mixed down to zero frequency. A Lorentzian fit (solid line) indicates sub-Hz relative linewidth.

the two-photon transition; by co-propagating the two laser drives the Doppler effects nearly cancel, but this adds a complication in the case of non-co-propagating lasers (such as the case discussed in Sec. 5.2.6).

Scanning the two laser frequencies produces different spectroscopic line-shapes near resonance in each case:

- scanning the frequency of the molecular-transition light while holding the photoassociation light frequency constant near resonance results in loss due to excited state decay except when the two-photon detuning δ becomes small, in which case coherent effects in the effective three-level system reduce the absorption on the photoassociation transition and produce a transparency feature, as in Fig. 5.9;

- scanning the frequency of the photoassociation light frequency while holding the other constant results in a broad absorption feature around the single-photon resonance but split into two, with a transparency feature at two-photon resonance, as in Fig. 5.7.

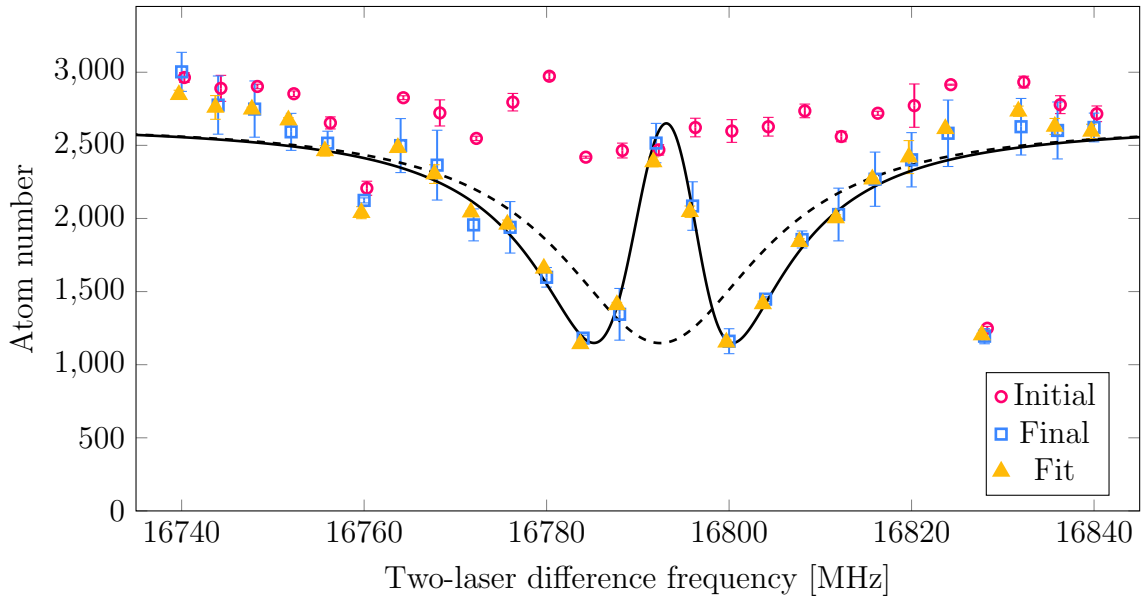


Figure 5.7: Two-color photoassociation spectroscopy of 0_g^- $\nu' = 1$, $a^3\Sigma$ $\nu = 36$. This atom loss spectrum was obtained by scanning the frequency of the photoassociation laser while the frequency of the laser driving the bound-to-bound molecular transition was held constant. Frequency-dependent atom losses are shown in the difference between the initial (red circles) and final (blue squares) atom numbers. The yellow triangles represent a single common fit of Eq. 5.13 with two-photon expression for $|S|^2$ from Eq. 5.10 to the final atom number data, incorporating the initial atom numbers as fixed parameters. The solid line is the same fit evaluated using the mean initial atom number. The dashed line is the same function evaluated without no ground molecular state present. The solid line captures the overall shape well, but the individual runs of the experiment and associated fluctuations are well-captured by the (yellow triangle) point-by-point common fit.

The relative widths of the absorption and transparency features depend on the laser intensities, transition strengths and thus Franck-Condon factors, transition linewidths, atom density, and atom cloud temperature; this is described in the scattering probability. In our experiments, the transparency feature serves as a signature of two-photon resonance with a molecular ground state, and through these measurements we have observed several ($\nu = 36, 37, 38, 39$) vibrational states of the $a^3\Sigma$ molecular potential and found that their binding energies agreed with numerical calculations.

5.5 Toward cavity and collective enhancement

Our goals for these experiments included the observation of cavity-mediated photoassociation, and to subsequently probe the collective enhancement of the photoassociation process

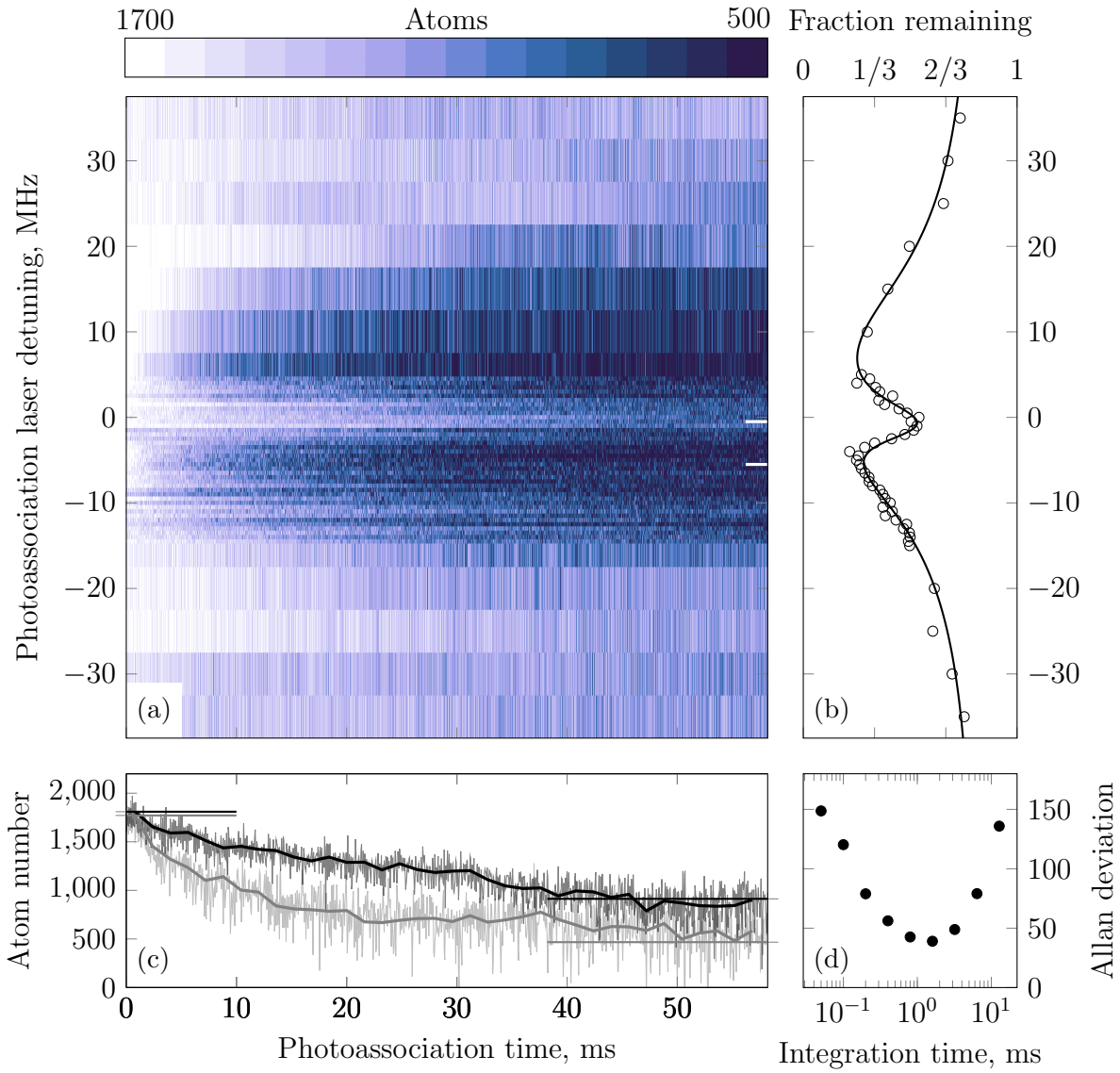


Figure 5.8: (a) Two-color atom loss spectrogram of 0_g^- $\nu' = 1$, $a^3\Sigma$ $\nu = 36$ obtained by scanning the frequency of the laser driving the photoassociation transition while the frequency of the laser driving the bound-to-bound was held constant, nearly resonant with the $\nu = 36$ to $\nu' = 1$ transition. (b) The fraction of initial atoms remaining at the end of the 55 ms photoassociation time. (c) Individual real-time atom number traces from the cavity transmission records show different loss dynamics for different laser detunings. These traces correspond to the detunings indicated by the small white lines on the right side of (a), with one chosen to be in the transparency feature and one near the maximal loss rate. (d) Allan deviation of the real-time atom number traces allowed real-time determination of the atom number to a precision of a few tens of atoms at an optimal integration time of 1–2 ms.

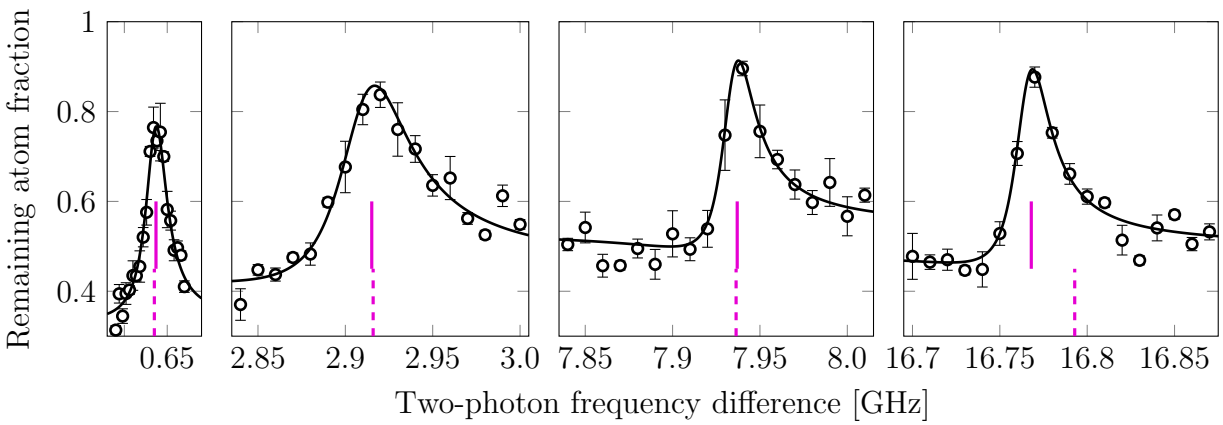


Figure 5.9: Two-color ^{87}Rb photoassociation spectroscopy of 0_g^- $\nu' = 1$, $a^3\Sigma$ $\nu \in \{36, 37, 38, 39\}$. These atom loss spectra were obtained by scanning the frequency of the laser driving the bound-to-bound transition while the frequency of the photoassociation laser was held constant, nearly resonant with the $\nu' = 1$ excited state; the photoassociation time was 58.65 ms. The spectra are all plotted with the same scaling. The solid lines are fits of Eq. 5.13 to the data with two-photon expression for $|S|^2$ from Eq. 5.10. Transparency features are observed at frequency differences of 643.5(4) MHz, 2915.1(23) MHz, 7937.0(9) MHz, and 16 768.0(11) MHz, which we interpret as the molecular state binding energies. The spectra appear asymmetric because the photoassociation light was slightly detuned from the excited state. We calculated the $a^3\Sigma$ vibrational state energies using the Fourier grid Hamiltonian method [168] with potential parameters from the literature [169] to be 642.5 MHz, 2.916 GHz, 7.936 GHz, and 16.793 GHz. Solid vertical lines mark our observed binding energies; dashed lines mark our calculated binding energies.

[170]. With our cavity tuned to the corresponding frequency, the high cooperativity $C = 16$ of our atom–cavity system could facilitate Purcell enhancement of a particular bound-to-bound transition. Excited molecules should then predominantly exchange their excitation with the cavity and into the cavity emission faster than they would decay via spontaneous emission into other radiation modes (and molecular states). We planned to explore detuning from the excited state while maintaining the two-photon (laser frequency + cavity frequency) resonance as this may have led to greater molecule creation efficiency/specificity by minimizing the population in the excited state and thus the "bad" spontaneous decays but did not have a chance to meaningfully explore this.

In addition to providing high specificity as to the ground state of the molecules created, the cavity-mediated configuration would allow relatively high efficiency heralding of successful molecule formation: each molecule that undergoes decay via emission of a photon into the cavity mode and subsequent emission of the cavity photon ends up in the chosen ground state, and detecting a photon in the cavity output indicates the creation of that molecule. To this end, in some of the experiments we swapped the heterodyne detection for a single-

photon avalanche detector (SPAD) that we coupled to a fiber, coupled in turn to the cavity output (after the dichroic beamsplitter to separate the ODT light). The fiber between the cavity output and the SPAD was thoroughly wrapped with opaque black tape to minimize stray light leaking into the detector input.

We performed a number of attempts to observe cavity-mediated photoassociation. Guided by our spectroscopic data to one of the two-photon transitions, we coupled one of the photoassociation lasers into the cavity pump path while we kept the other incident from the side of the cavity. The large free spectral range of our cavity would have prevented effective simultaneous coupling of both photoassociation lasers into the cavity mode, lacking knowledge of a two-photon molecular transition with energy difference that matched the free spectral range. This meant that, unlike our prior experiments, the propagation axes of the two lasers now had a relative 90° angle. The non-collinear nature means that there would now be a Doppler shift on the narrow two-photon transition, which the collinear case conveniently avoids almost completely due to the nearly equal wavevectors. Additionally, with the cavity nearly resonant with one of the molecular transitions it was now far from the atomic transition, so we were unable to use our normal high-sensitivity dispersive atom number measurements to monitor the photoassociation process, instead relying on (destructive) absorption imaging to count the atoms, and the light leaking from the cavity coupled onto the SPAD. Our attempts included driving both transitions by side-pumping and the cavity light, and also driving just the photoassociation transition while holding the cavity near resonance with the bound-to-bound transition but without pumping it with a coupled laser. We were also considering that if the photoassociation process was strong enough and the atom number large enough, the cloud could develop a macroscopic dipole moment that would superradiantly enhance further scattering into the cavity mode. This acceleration of scattering would increase $\sim \sqrt{N_\mathrm{a}}$ as the atom number N_a increases and may have presented a signature in the time-correlation of photons reaching the cavity: a large number of the atoms photoassociating and emitting into the cavity mode at once would produce a burst of photons from the cavity.

Ultimately, we were not able to observe signatures of cavity-mediated photoassociation within the time we had allotted to the search. I suspect that this was due to a combination of factors including the challenge of ensuring that we were simultaneously resonant with both transitions, while not having a sensitive measure of the atom number without reconfiguring the optical paths; the Doppler shift present given the non-collinear two-photon transition configuration; complications and uncertainties about the molecular selection rules for the combination of light polarizations and the field axis; and possibly insufficient available optical power for a significant fraction of the cloud to undergo photoassociation fast enough that it would be distinguishable from the background of photons reaching the SPAD from the cavity.

Bibliography

1. Parker, R. H., Yu, C., Zhong, W., Estey, B. & Müller, H. Measurement of the fine-structure constant as a test of the Standard Model. *Science* **360,** 191–195 (2018).
2. Morel, L., Yao, Z., Cladé, P. & Guellati-Khélifa, S. Determination of the fine-structure constant with an accuracy of 81 parts per trillion. *Nature* **588,** 61–65. ISSN: 1476-4687 (2020).
3. Planck, M. Über das Gesetz der Energieverteilung im Normalspectrum. *Ann. Phys* **309,** 553–563 (1901).
4. Einstein, A. Über einen die Erzeugung und Verwandlung des Lichtes betreffenden heuristischen Gesichtspunkt. *Annalen der Physik* **322,** 132–148 (1905).
5. Kimble, H. J., Dagenais, M. & Mandel, L. Photon Antibunching in Resonance Fluorescence. *Phys. Rev. Lett.* **39,** 691–695 (1977).
6. Wolf, J. *et al.* Autonomous Feedback Stabilization of a Cavity-Coupled Spin Oscillator. *Phys. Rev. Lett.* **134,** 053603 (2025).
7. Wolf, J. *Coherent and Incoherent Quantum Feedback in an Atom–Cavity System* PhD thesis (University of California, Berkeley, 2023).
8. Devoret, M. H., Martinis, J. M. & Clarke, J. Measurements of Macroscopic Quantum Tunneling out of the Zero-Voltage State of a Current-Biased Josephson Junction. *Phys. Rev. Lett.* **55,** 1908–1911 (1985).
9. Nakamura, Y., Chen, C. D. & Tsai, J. S. Spectroscopy of Energy-Level Splitting between Two Macroscopic Quantum States of Charge Coherently Superposed by Josephson Coupling. *Phys. Rev. Lett.* **79,** 2328–2331 (1997).
10. Mooij, J. E. *et al.* Josephson Persistent-Current Qubit. *Science* **285,** 1036–1039 (1999).
11. Wallraff, A. *et al.* Strong coupling of a single photon to a superconducting qubit using circuit quantum electrodynamics. *Nature* **431,** 162–167. ISSN: 1476-4687 (2004).
12. Koch, J. *et al.* Charge-insensitive qubit design derived from the Cooper pair box. *Phys. Rev. A* **76,** 042319 (2007).
13. You, J. Q. & Nori, F. Atomic physics and quantum optics using superconducting circuits. *Nature* **474,** 589–597. ISSN: 1476-4687 (2011).

14. Kjaergaard, M. *et al.* Superconducting Qubits: Current State of Play. *Annual Review of Condensed Matter Physics* **11,** 369–395. ISSN: 1947-5462 (2020).

15. Kastner, M. A. Artificial Atoms. *Physics Today* **46,** 24–31. ISSN: 0031-9228 (1993).

16. Ashoori, R. C. Electrons in artificial atoms. *Nature* **379,** 413–419. ISSN: 1476-4687 (1996).

17. Banin, U., Cao, Y., Katz, D. & Millo, O. Identification of atomic-like electronic states in indium arsenide nanocrystal quantum dots. *Nature* **400,** 542–544. ISSN: 1476-4687 (1999).

18. Jelezko, F., Gaebel, T., Popa, I., Gruber, A. & Wrachtrup, J. Observation of Coherent Oscillations in a Single Electron Spin. *Phys. Rev. Lett.* **92,** 076401 (2004).

19. Epstein, R. J., Mendoza, F. M., Kato, Y. K. & Awschalom, D. D. Anisotropic interactions of a single spin and dark-spin spectroscopy in diamond. *Nature Physics* **1,** 94–98. ISSN: 1745-2481 (2005).

20. Wrachtrup, J. & Jelezko, F. Processing quantum information in diamond. *Journal of Physics: Condensed Matter* **18,** S807 (2006).

21. Hanson, R., Mendoza, F. M., Epstein, R. J. & Awschalom, D. D. Polarization and Readout of Coupled Single Spins in Diamond. *Phys. Rev. Lett.* **97,** 087601 (2006).

22. Gaebel, T. *et al.* Room-temperature coherent coupling of single spins in diamond. *Nature Physics* **2,** 408–413. ISSN: 1745-2481 (2006).

23. Dutt, M. V. G. *et al.* Quantum Register Based on Individual Electronic and Nuclear Spin Qubits in Diamond. *Science* **316,** 1312–1316 (2007).

24. Maze, J. R. *et al.* Nanoscale magnetic sensing with an individual electronic spin in diamond. *Nature* **455,** 644–647. ISSN: 1476-4687 (2008).

25. Metcalf, H. J. & van der Straten, P. in *The Optics Encyclopedia* (John Wiley & Sons, Ltd, 2007). ISBN: 9783527600441.

26. Stenger, J. *et al.* Spin domains in ground-state Bose–Einstein condensates. *Nature* **396,** 345–348. ISSN: 1476-4687 (1998).

27. Miesner, H.-J. *et al.* Observation of Metastable States in Spinor Bose-Einstein Condensates. *Phys. Rev. Lett.* **82,** 2228–2231 (1999).

28. Stamper-Kurn, D. M. *et al.* Quantum Tunneling across Spin Domains in a Bose-Einstein Condensate. *Phys. Rev. Lett.* **83,** 661–665 (1999).

29. Autler, S. H. & Townes, C. H. Stark Effect in Rapidly Varying Fields. *Phys. Rev.* **100,** 703–722 (1955).

30. Bize, S. *et al.* High-accuracy measurement of the 87Rb ground-state hyperfine splitting in an atomic fountain. *Europhysics Letters* **45,** 558 (1999).

31. Steck, D. A. Rubidium 87 D Line Data (2001).

32. Ye, J., Swartz, S., Jungner, P. & Hall, J. L. Hyperfine structure and absolute frequency of the 87Rb 5P3/2 state. *Opt. Lett.* **21,** 1280–1282 (1996).
33. Giovannetti, V., Lloyd, S. & Maccone, L. Quantum-Enhanced Measurements: Beating the Standard Quantum Limit. *Science* **306,** 1330–1336 (2004).
34. Giovannetti, V., Lloyd, S. & Maccone, L. Advances in quantum metrology. *Nature Photonics* **5,** 222–229. ISSN: 1749-4893 (2011).
35. Wineland, D. J., Bollinger, J. J., Itano, W. M. & Heinzen, D. J. Squeezed atomic states and projection noise in spectroscopy. *Phys. Rev. A* **50,** 67–88 (1994).
36. Wineland, D. J., Bollinger, J. J., Itano, W. M., Moore, F. L. & Heinzen, D. J. Spin squeezing and reduced quantum noise in spectroscopy. *Phys. Rev. A* **46,** R6797–R6800 (1992).
37. Arndt, M. & Hornberger, K. Testing the limits of quantum mechanical superpositions. *Nature Physics* **10,** 271–277. ISSN: 1745-2481 (2014).
38. Nimmrichter, S., Hornberger, K. & Hammerer, K. Optomechanical Sensing of Spontaneous Wave-Function Collapse. *Phys. Rev. Lett.* **113,** 020405 (2014).
39. Brion, E., Pedersen, L. H. & Mølmer, K. Adiabatic elimination in a lambda system. *Journal of Physics A: Mathematical and Theoretical* **40,** 1033 (2007).
40. Happer, W. & Mathur, B. S. Off-Resonant Light as a Probe of Optically Pumped Alkali Vapors. *Phys. Rev. Lett.* **18,** 577–580 (1967).
41. Murch, K. W. *Cavity quantum optomechanics with ultracold atoms* English. PhD thesis (2008), 146. ISBN: 978-0-549-83350-5.
42. Marquardt, F. & Girvin, S. M. Optomechanics. *Physics* **2** (2009).
43. Purdy, T. P. *et al.* Tunable Cavity Optomechanics with Ultracold Atoms. *Phys. Rev. Lett.* **105,** 133602 (2010).
44. Riedinger, R. *et al.* Remote quantum entanglement between two micromechanical oscillators. *Nature* **556,** 473–477. ISSN: 1476-4687 (2018).
45. Ockeloen-Korppi, C. F. *et al.* Stabilized entanglement of massive mechanical oscillators. *Nature* **556,** 478–482. ISSN: 1476-4687 (2018).
46. Pirkkalainen, J.-M., Damskägg, E., Brandt, M., Massel, F. & Sillanpää, M. A. Squeezing of Quantum Noise of Motion in a Micromechanical Resonator. *Phys. Rev. Lett.* **115,** 243601 (2015).
47. Wollman, E. E. *et al.* Quantum squeezing of motion in a mechanical resonator. *Science* **349,** 952–955 (2015).
48. Brooks, D. W. C. *et al.* Non-classical light generated by quantum-noise-driven cavity optomechanics. *Nature* **488,** 476–480. ISSN: 1476-4687 (2012).

49. Brahms, N., Botter, T., Schreppler, S., Brooks, D. W. C. & Stamper-Kurn, D. M. Optical Detection of the Quantization of Collective Atomic Motion. *Phys. Rev. Lett.* **108,** 133601 (2012).
50. Brahms, N. & Stamper-Kurn, D. M. Spin optodynamics analog of cavity optomechanics. *Phys. Rev. A* **82,** 041804 (2010).
51. Schreppler, S. *et al.* Optically measuring force near the standard quantum limit. *Science* **344,** 1486–1489 (2014).
52. Spethmann, N., Kohler, J., Schreppler, S., Buchmann, L. & Stamper-Kurn, D. M. Cavity-mediated coupling of mechanical oscillators limited by quantum back-action. *Nature Physics* **12,** 27–31. ISSN: 1745-2481 (2016).
53. Kohler, J., Gerber, J. A., Deist, E. & Stamper-Kurn, D. M. Simultaneous retrodiction of multimode optomechanical systems using matched filters. *Phys. Rev. A* **101,** 023804 (2020).
54. Kohler, J., Spethmann, N., Schreppler, S. & Stamper-Kurn, D. M. Cavity-Assisted Measurement and Coherent Control of Collective Atomic Spin Oscillators. *Phys. Rev. Lett.* **118,** 063604 (2017).
55. Kohler, J., Gerber, J. A., Dowd, E. & Stamper-Kurn, D. M. Negative-Mass Instability of the Spin and Motion of an Atomic Gas Driven by Optical Cavity Backaction. *Phys. Rev. Lett.* **120,** 013601 (2018).
56. Zeiher, J., Wolf, J., Isaacs, J. A., Kohler, J. & Stamper-Kurn, D. M. Tracking Evaporative Cooling of a Mesoscopic Atomic Quantum Gas in Real Time. *Phys. Rev. X* **11,** 041017 (2021).
57. Jaynes, E. & Cummings, F. Comparison of quantum and semiclassical radiation theories with application to the beam maser. *Proceedings of the IEEE* **51,** 89–109 (1963).
58. Tavis, M. & Cummings, F. W. Exact Solution for an N-Molecule–Radiation-Field Hamiltonian. *Phys. Rev.* **170,** 379–384 (1968).
59. Purdy, T. *Cavity QED with Ultracold Atoms on an Atom Chip* PhD thesis (University of California, Berkeley, 2009).
60. Bergner, D. *et al.* Polarization dependent photoemission as a probe of the magnetic ground state in the van der Waals ferromagnet VI3. *Applied Physics Letters* **121,** 183104. ISSN: 0003-6951 (2022).
61. Maksimovic, N. *et al.* Evidence for a delocalization quantum phase transition without symmetry breaking in $CeCoIn_5$. *Science* **375,** 76–81 (2022).
62. Aspect, A., Arimondo, E., Kaiser, R., Vansteenkiste, N. & Cohen-Tannoudji, C. Laser Cooling below the One-Photon Recoil Energy by Velocity-Selective Coherent Population Trapping. *Phys. Rev. Lett.* **61,** 826–829 (1988).
63. Dalibard, J. & Cohen-Tannoudji, C. Laser cooling below the Doppler limit by polarization gradients: simple theoretical models. *J. Opt. Soc. Am. B* **6,** 2023–2045 (1989).

64. Kastler, A. Optical Methods of Atomic Orientation and of Magnetic Resonance∗. *J. Opt. Soc. Am.* **47,** 460–465 (1957).

65. Happer, W. Optical Pumping. *Rev. Mod. Phys.* **44,** 169–249 (1972).

66. Born, M. *et al.* in *Principles of Optics: Electromagnetic Theory of Propagation, Interference and Diffraction of Light* 1–74 (Cambridge University Press, 1999).

67. Byrnes, S. J. *Multilayer optical calculations* 2020.

68. Luce, A., Mahdavi, A., Marquardt, F. & Wankerl, H. TMM-Fast, a transfer matrix computation package for multilayer thin-film optimization: tutorial. *Journal of the Optical Society of America A* **39,** 1007. ISSN: 1520-8532 (2022).

69. Marcos, L. V. R.-d., Larruquert, J. I., Méndez, J. A. & Aznárez, J. A. Self-consistent optical constants of SiO_2 and Ta_2O_5 films. *Opt. Mater. Express* **6,** 3622–3637 (2016).

70. Gao, L., Lemarchand, F. & Lequime, M. Exploitation of multiple incidences spectrometric measurements for thin film reverse engineering. *Opt. Express* **20,** 15734–15751 (2012).

71. Gao, L., Lemarchand, F. & Lequime, M. Refractive index determination of SiO_2 layer in the UV/Vis/NIR range: spectrophotometric reverse engineering on single and bilayer designs. *J. Eur. Opt. Soc.-Rapid Publ.* **8,** 13010 (2013).

72. Polyanskiy, M. *Refractiveindex.info database of optical constants* 2024.

73. Kohler, J. *Optodynamical Measurement and Coupling of Atomic Motion and Spin* PhD thesis (University of California, Berkeley, 2018).

74. Debatin, M. *Creation of Ultracold RbCs Ground-State Molecules* PhD thesis (Institute of Experimental Physics, University of Innsbruck, 2013).

75. Wieman, C. & Hänsch, T. W. Doppler-Free Laser Polarization Spectroscopy. *Phys. Rev. Lett.* **36,** 1170–1173 (1976).

76. Bjorklund, G. C. Frequency-modulation spectroscopy: a new method for measuring weak absorptions and dispersions. *Opt. Lett.* **5,** 15–17 (1980).

77. Corwin, K. L., Lu, Z.-T., Hand, C. F., Epstein, R. J. & Wieman, C. E. Frequency-stabilized diode laser with the Zeeman shift in an atomic vapor. *Appl. Opt.* **37,** 3295–3298 (1998).

78. Petelski, T., Fattori, M., Lamporesi, G., Stuhler, J. & Tino, G. Doppler-free spectroscopy using magnetically induced dichroism of atomic vapor: a new scheme for laser frequency locking. *The European Physical Journal D - Atomic, Molecular, Optical and Plasma Physics* **22,** 279–283 (2003).

79. Smith, P. W. & Hänsch, R. Cross-Relaxation Effects in the Saturation of the 6328-Å Neon-Laser Line. *Phys. Rev. Lett.* **26,** 740–743 (1971).

80. MacAdam, K. B., Steinbach, A. & Wieman, C. A narrow-band tunable diode laser system with grating feedback, and a saturated absorption spectrometer for Cs and Rb. *American Journal of Physics* **60,** 1098–1111. ISSN: 0002-9505 (1992).

81. Raj, R. K., Bloch, D., Snyder, J. J., Camy, G. & Ducloy, M. High-Frequency Optically Heterodyned Saturation Spectroscopy Via Resonant Degenerate Four-Wave Mixing. *Phys. Rev. Lett.* **44,** 1251–1254 (1980).

82. Zhang, H. *et al.* Collective State Measurement of Mesoscopic Ensembles with Single-Atom Resolution. *Phys. Rev. Lett.* **109,** 133603 (2012).

83. Livingston, W. *Continuous Feedback on Quantum Superconducting Circuits* PhD thesis (University of California, Berkeley, 2021).

84. Bender, P. L. & Owens, J. C. Correction of optical distance measurements for the fluctuating atmospheric index of refraction. *Journal of Geophysical Research (1896-1977)* **70,** 2461–2462 (1965).

85. Wu, G., Takahashi, M., Arai, K., Inaba, H. & Minoshima, K. Extremely high-accuracy correction of air refractive index using two-colour optical frequency combs. *Scientific Reports* **3,** 1894. ISSN: 2045-2322 (2013).

86. Matsumoto, H. & Honda, T. High-accuracy length-measuring interferometer using the two-colour method of compensating for the refractive index of air. *Measurement Science and Technology* **3,** 1084 (1992).

87. Tiamsuphat, J. *analog-PI* https://github.com/JQIamo/analog-pi. 2016.

88. Galison, P. *How Experiments End* (The University of Chicago Press, 1987).

89. IEEE Guide for the Application of Component Surge-Protective Devices for Use in Low-Voltage [Equal to or Less than 1000 V (ac) Or 1200 V (dc)] Circuits. *IEEE Std C62.42-2005 (Revision of IEEE C62.42-1992),* 1–105 (2006).

90. Clerk, A. A., Devoret, M. H., Girvin, S. M., Marquardt, F. & Schoelkopf, R. J. Introduction to quantum noise, measurement, and amplification. *Rev. Mod. Phys.* **82,** 1155–1208 (2010).

91. Grynberg, G., Aspect, A. & Fabre, C. *Introduction to Quantum Optics: From the Semi-classical Approach to Quantized Light* (Cambridge University Press, 2010).

92. Cohen-Tannoudji, C., Dupont-Roc, J. & Grynberg, G. *Photons and Atoms* ISBN: 9783527618422 (John Wiley & Sons, Ltd, 1997).

93. Schleier-Smith, M. H., Leroux, I. D. & Vuleti ć, V. States of an Ensemble of Two-Level Atoms with Reduced Quantum Uncertainty. *Phys. Rev. Lett.* **104,** 073604 (2010).

94. Kippenberg, T. J. & Vahala, K. J. Cavity Optomechanics: Back-Action at the Mesoscale. *Science* **321,** 1172–1176 (2008).

95. Marquardt, F., Chen, J. P., Clerk, A. A. & Girvin, S. M. Quantum Theory of Cavity-Assisted Sideband Cooling of Mechanical Motion. *Phys. Rev. Lett.* **99,** 093902 (2007).

96. Wilson-Rae, I., Nooshi, N., Zwerger, W. & Kippenberg, T. J. Theory of Ground State Cooling of a Mechanical Oscillator Using Dynamical Backaction. *Phys. Rev. Lett.* **99,** 093901 (2007).

97. Genes, C., Vitali, D., Tombesi, P., Gigan, S. & Aspelmeyer, M. Ground-state cooling of a micromechanical oscillator: Comparing cold damping and cavity-assisted cooling schemes. *Phys. Rev. A* **77,** 033804 (2008).

98. Wilson-Rae, I., Nooshi, N., Dobrindt, J., Kippenberg, T. J. & Zwerger, W. Cavity-assisted backaction cooling of mechanical resonators. *New Journal of Physics* **10,** 095007 (2008).

99. Delić, U. *et al.* Cooling of a levitated nanoparticle to the motional quantum ground state. *Science* **367,** 892–895 (2020).

100. Teufel, J. D. *et al.* Sideband cooling of micromechanical motion to the quantum ground state. *Nature* **475,** 359–363. ISSN: 1476-4687 (2011).

101. Chan, J. *et al.* Laser cooling of a nanomechanical oscillator into its quantum ground state. *Nature* **478,** 89–92. ISSN: 1476-4687 (2011).

102. Hammerer, K., Mølmer, K., Polzik, E. S. & Cirac, J. I. Light-matter quantum interface. *Phys. Rev. A* **70,** 044304 (2004).

103. Madsen, L. B. & Mølmer, K. Spin squeezing and precision probing with light and samples of atoms in the Gaussian description. *Phys. Rev. A* **70,** 052324 (2004).

104. Ozeri, R. *et al.* Hyperfine Coherence in the Presence of Spontaneous Photon Scattering. *Phys. Rev. Lett.* **95,** 030403 (2005).

105. Vuletić, V., Chan, H. W. & Black, A. T. Three-dimensional cavity Doppler cooling and cavity sideband cooling by coherent scattering. *Phys. Rev. A* **64,** 033405 (2001).

106. Kimble, H. J. Strong interactions of single atoms and photons in cavity QED. *Physica Scripta* **1998,** 127 (1998).

107. Huang, G. M., Tarn, T. J. & Clark, J. W. On the controllability of quantum-mechanical systems. *Journal of Mathematical Physics* **24,** 2608–2618. ISSN: 0022-2488 (1983).

108. Lloyd, S. Coherent quantum feedback. *Phys. Rev. A* **62,** 022108 (2000).

109. Mabuchi, H. & Khaneja, N. Principles and applications of control in quantum systems. *International Journal of Robust and Nonlinear Control* **15,** 647–667 (2005).

110. Zhang, J., Liu, Y.-x., Wu, R.-B., Jacobs, K. & Nori, F. Quantum feedback: Theory, experiments, and applications. *Physics Reports* **679,** 1–60. ISSN: 0370-1573 (2017).

111. Shor, P. W. Scheme for reducing decoherence in quantum computer memory. *Phys. Rev. A* **52,** R2493–R2496 (1995).

112. Steane, A. M. Error Correcting Codes in Quantum Theory. *Phys. Rev. Lett.* **77,** 793–797 (1996).

113. Geerlings, K. *et al.* Demonstrating a Driven Reset Protocol for a Superconducting Qubit. *Phys. Rev. Lett.* **110,** 120501 (2013).

114. Keßler, H., Klinder, J., Wolke, M. & Hemmerich, A. Steering Matter Wave Superradiance with an Ultranarrow-Band Optical Cavity. *Phys. Rev. Lett.* **113,** 070404 (2014).

115. Dür, W., Skotiniotis, M., Fröwis, F. & Kraus, B. Improved Quantum Metrology Using Quantum Error Correction. *Phys. Rev. Lett.* **112,** 080801 (2014).

116. Zhou, S. & Jiang, L. Optimal approximate quantum error correction for quantum metrology. *Phys. Rev. Res.* **2,** 013235 (2020).

117. Pan, J.-W., Simon, C., Brukner, Č. & Zeilinger, A. Entanglement purification for quantum communication. *Nature* **410,** 1067–1070. ISSN: 1476-4687 (2001).

118. Armen, M. A., Au, J. K., Stockton, J. K., Doherty, A. C. & Mabuchi, H. Adaptive Homodyne Measurement of Optical Phase. *Phys. Rev. Lett.* **89,** 133602 (2002).

119. Sayrin, C. *et al.* Real-time quantum feedback prepares and stabilizes photon number states. *Nature* **477,** 73–77. ISSN: 1476-4687 (2011).

120. Vijay, R. *et al.* Stabilizing Rabi oscillations in a superconducting qubit using quantum feedback. *Nature* **490,** 77–80. ISSN: 1476-4687 (2012).

121. Ristè, D., Bultink, C. C., Lehnert, K. W. & DiCarlo, L. Feedback Control of a Solid-State Qubit Using High-Fidelity Projective Measurement. *Phys. Rev. Lett.* **109,** 240502 (2012).

122. Campagne-Ibarcq, P. *et al.* Persistent Control of a Superconducting Qubit by Stroboscopic Measurement Feedback. *Phys. Rev. X* **3,** 021008 (2013).

123. Doherty, A. C., Habib, S., Jacobs, K., Mabuchi, H. & Tan, S. M. Quantum feedback control and classical control theory. *Phys. Rev. A* **62,** 012105 (2000).

124. Hofmann, H. F., Mahler, G. & Hess, O. Quantum control of atomic systems by homodyne detection and feedback. *Phys. Rev. A* **57,** 4877–4888 (1998).

125. Gertler, J. M. *et al.* Protecting a bosonic qubit with autonomous quantum error correction. *Nature* **590,** 243–248. ISSN: 1476-4687 (2021).

126. Puri, S. *et al.* Bias-preserving gates with stabilized cat qubits. *Science Advances* **6** (2020).

127. Ma, W.-L. *et al.* Quantum control of bosonic modes with superconducting circuits. *Science Bulletin* **66,** 1789–1805. ISSN: 2095-9273 (2021).

128. Murch, K. W. *et al.* Cavity-Assisted Quantum Bath Engineering. *Phys. Rev. Lett.* **109,** 183602 (2012).

129. Ristè, D. *et al.* Deterministic entanglement of superconducting qubits by parity measurement and feedback. *Nature* **502,** 350–354. ISSN: 1476-4687 (2013).

130. Shankar, S. *et al.* Autonomously stabilized entanglement between two superconducting quantum bits. *Nature* **504,** 419–422. ISSN: 1476-4687 (2013).

131. Lin, Y. *et al.* Dissipative production of a maximally entangled steady state of two quantum bits. *Nature* **504,** 415–418. ISSN: 1476-4687 (2013).

132. Leghtas, Z. *et al.* Stabilizing a Bell state of two superconducting qubits by dissipation engineering. *Phys. Rev. A* **88,** 023849 (2013).

133. Andersen, C. K., Kerckhoff, J., Lehnert, K. W., Chapman, B. J. & Mølmer, K. Closing a quantum feedback loop inside a cryostat: Autonomous state preparation and long-time memory of a superconducting qubit. *Phys. Rev. A* **93,** 012346 (2016).

134. Mabuchi, H. Coherent-feedback quantum control with a dynamic compensator. *Phys. Rev. A* **78,** 032323 (2008).

135. Schleier-Smith, M. H., Leroux, I. D. & Vuleti ć, V. Squeezing the collective spin of a dilute atomic ensemble by cavity feedback. *Phys. Rev. A* **81,** 021804 (2010).

136. Kitagawa, M. & Ueda, M. Squeezed spin states. *Phys. Rev. A* **47,** 5138–5143 (1993).

137. Caves, C. M. Quantum-mechanical noise in an interferometer. *Phys. Rev. D* **23,** 1693–1708 (1981).

138. Takeuchi, M. *et al.* Spin Squeezing via One-Axis Twisting with Coherent Light. *Phys. Rev. Lett.* **94,** 023003 (2005).

139. Takahashi, Y. *et al.* Quantum nondemolition measurement of spin via the paramagnetic Faraday rotation. *Phys. Rev. A* **60,** 4974–4979 (1999).

140. Saffman, M., Oblak, D., Appel, J. & Polzik, E. S. Spin squeezing of atomic ensembles by multicolor quantum nondemolition measurements. *Phys. Rev. A* **79,** 023831 (2009).

141. Gross, C. Spin squeezing, entanglement and quantum metrology with Bose–Einstein condensates. *Journal of Physics B: Atomic, Molecular and Optical Physics* **45,** 103001 (2012).

142. Block, M. *et al.* Scalable spin squeezing from finite-temperature easy-plane magnetism. *Nature Physics* **20,** 1575–1581. ISSN: 1745-2481 (2024).

143. Sørensen, A., Duan, L.-M., Cirac, J. I. & Zoller, P. Many-particle entanglement with Bose–Einstein condensates. *Nature* **409,** 63–66. ISSN: 1476-4687 (2001).

144. Kronwald, A., Marquardt, F. & Clerk, A. A. Arbitrarily large steady-state bosonic squeezing via dissipation. *Phys. Rev. A* **88,** 063833 (2013).

145. Thomsen, L. K., Mancini, S. & Wiseman, H. M. Spin squeezing via quantum feedback. *Phys. Rev. A* **65,** 061801 (2002).

146. Thomsen, L. K., Mancini, S. & Wiseman, H. M. Continuous quantum nondemolition feedback and unconditional atomic spin squeezing. *Journal of Physics B: Atomic, Molecular and Optical Physics* **35,** 4937 (2002).

147. Corney, J. F. & Milburn, G. J. Homodyne measurements on a Bose-Einstein condensate. *Phys. Rev. A* **58,** 2399–2406 (1998).

148. Wiseman, H. M. Quantum theory of continuous feedback. *Phys. Rev. A* **49,** 2133–2150 (1994).

149. Jones, K. M., Tiesinga, E., Lett, P. D. & Julienne, P. S. Ultracold photoassociation spectroscopy: Long-range molecules and atomic scattering. *Rev. Mod. Phys.* **78,** 483–535 (2006).

150. Ni, K.-K. *et al.* A High Phase-Space-Density Gas of Polar Molecules. *Science* **322,** 231–235 (2008).

151. DeMille, D., Hutzler, N. R., Rey, A. M. & Zelevinsky, T. Quantum sensing and metrology for fundamental physics with molecules. *Nature Physics* **20,** 741–749. ISSN: 1745-2481 (2024).

152. Bigagli, N. *et al.* Observation of Bose–Einstein condensation of dipolar molecules. *Nature* **631,** 289–293. ISSN: 1476-4687 (2024).

153. Cornish, S. L., Tarbutt, M. R. & Hazzard, K. R. A. Quantum computation and quantum simulation with ultracold molecules. *Nature Physics* **20,** 730–740. ISSN: 1745-2481 (2024).

154. Langen, T., Valtolina, G., Wang, D. & Ye, J. Quantum state manipulation and cooling of ultracold molecules. *Nature Physics* **20,** 702–712. ISSN: 1745-2481 (2024).

155. Miller, J. D., Cline, R. A. & Heinzen, D. J. Photoassociation spectrum of ultracold Rb atoms. *Phys. Rev. Lett.* **71,** 2204–2207 (1993).

156. Martinez de Escobar, Y. N. *et al.* Two-photon photoassociative spectroscopy of ultracold ^{88}Sr. *Phys. Rev. A* **78,** 062708 (2008).

157. Pichler, M. *et al.* Photoassociation of ultracold K atoms: Observation of high lying levels of the 1g$\sim 1^1\Pi$g molecular state of K_2. *The Journal of Chemical Physics* **118,** 7837–7845. ISSN: 0021-9606 (2003).

158. Gordon, J. P. & Ashkin, A. Motion of atoms in a radiation trap. *Phys. Rev. A* **21,** 1606–1617 (1980).

159. Gardiner, C. W., Ye, J., Nagerl, H. C. & Kimble, H. J. Evaluation of heating effects on atoms trapped in an optical trap. *Phys. Rev. A* **61,** 045801 (2000).

160. Bohn, J. L. & Julienne, P. S. Semianalytic treatment of two-color photoassociation spectroscopy and control of cold atoms. *Physical Review A* **54** (1996).

161. Band, Y. B. & Julienne, P. S. Ultracold-molecule production by laser-cooled atom photoassociation. *Phys. Rev. A* **51,** R4317–R4320 (1995).

162. Thorsheim, H. R., Weiner, J. & Julienne, P. S. Laser-induced photoassociation of ultracold sodium atoms. *Phys. Rev. Lett.* **58,** 2420–2423 (1987).

163. Bohn, J. L. & Julienne, P. S. Semianalytic theory of laser-assisted resonant cold collisions. *Phys. Rev. A* **60,** 414–425 (1999).

164. Martinez de Escobar, Y. N. *et al.* Two-photon photoassociative spectroscopy of ultracold ^{88}Sr. *Physical Review A* **78** (2008).

165. Napolitano, R., Weiner, J., Williams, C. J. & Julienne, P. S. Line Shapes of High Resolution Photoassociation Spectra of Optically Cooled Atoms. *Physical Review Letters* **73** (1994).

166. Bruzewicz, C. D., Gustavsson, M., Shimasaki, T. & DeMille, D. Continuous formation of vibronic ground state RbCs molecules via photoassociation. *New Journal of Physics* **16,** 023018 (2014).

167. Pillet, P. *et al.* Photoassociation in a gas of cold alkali atoms: I. Perturbative quantum approach. *Journal of Physics B: Atomic, Molecular and Optical Physics* **30,** 2801 (1997).

168. Marston, C. C. & Balint-Kurti, G. G. The Fourier grid Hamiltonian method for bound state eigenvalues and eigenfunctions. *The Journal of Chemical Physics* **91,** 3571–3576. ISSN: 0021-9606 (1989).

169. Guan, Y. *et al.* Updated potential energy function of the Rb_2 $a^3\Sigma_u^+ a^3\Sigma_u^+$ state in the attractive and repulsive regions determined from its joint analysis with the $2^3\Pi_g$ state. *The Journal of Chemical Physics* **139,** 144303. ISSN: 0021-9606 (2013).

170. Kampschulte, T. & Hecker Denschlag, J. Cavity-controlled formation of ultracold molecules. *New J. Phys.* **20** (2018).